Study of germanium carbide and zirconium nitride as an absorber material for hot carrier solar cells

Author:
Gupta, Neeti

Publication Date:
2019

DOI:
https://doi.org/10.26190/unsworks/21118

Study of Germanium carbide and Zirconium nitride as an absorber material for Hot Carrier Solar Cells

A thesis in fulfilment of the requirements for the degree of

Doctor of Philosophy

by

Neeti Gupta

The School of Photovoltaic and Renewable Energy Engineering

The University of New South Wales

Sydney, Australia

August 2016

PLEASE TYPE

THE UNIVERSITY OF NEW SOUTH WALES
Thesis/Dissertation Sheet

Surname or Family name: Gupta

First name: Neeti

Other name/s:

Abbreviation for degree as given in the University calendar:

School: Photovoltaic and Renewable Energy

Faculty: Engineering

Title: **Study of Germanium Carbide and Zirconium Nitride as an absorber material for Hot Carrier Solar Cells**

Abstract 350 words maximum: (PLEASE TYPE)

Hot Carrier Solar Cell (HC-SC) is one of the advanced photovoltaic technologies. The two main building blocks of a HC-SC are: the absorber, where electrons- holes pairs are photo generated by absorbing the incoming photons, and the energy selective contacts, which allow extraction of these carriers to the external circuit in a narrow range of energies. HC-SCs offer the possibility of operating at very high efficiencies (Limiting efficiency above 65% for un-concentrated light) with structure of reduced complexity. An ideal HC-SC operates at very high efficiency by absorbing wide range of photon energies and extracting the photo-generated carriers at elevated temperatures before they thermalize to the band-edge of the absorber material. The finding of suitable absorber material and its fabrication along with characterisation are the initial steps to implement the HC-SC with a better efficiency. Germanium Carbide (GeC) and Zirconium nitride (ZrN) have a large mass difference between their consecutive elements and exhibit a large phonon band gap sufficient to block the dominant carrier cooling mechanism by Klemens decay route. In this thesis, GeC and ZrN have been studied to investigate their suitability as absorbers for HC-SCs. These material have been fabricated using sputtering and characterised using an array of techniques such as X-ray photoelectron spectroscopy, transmission microscopy, X-ray diffraction, Raman spectroscopy, Atomic Force Microscopy and optical absorption spectroscopy to study structural, compositional and optical properties. Transient absorption spectroscopy was used to study the carrier dynamics. Nano-crystalline GeC has been fabricated which may be suitable for photovoltaic application. Germanium carbide with the record of 15.5 % GeC has been demonstrated. Growth of ZrN have been demonstrated in the range of process parameters. Epitaxial growth of ZrN on MgO substrate has been achieved with DC sputtering at 500°C. Carrier dynamics in ZRN film have been investigated with Ultrafast transient absorption measurements which have indicated a long relaxation time of order of hundreds of picoseconds. The finding in the thesis provide initial insight into the properties of GeC and ZrN and show the possibilities of these materials as an absorber for the HC-SC.

Declaration relating to disposition of project thesis/dissertation

Signature | Witness Signature | Date

FOR OFFICE USE ONLY

Date of completion of requirements for Award:

ORIGINALITY STATEMENT

'I hereby declare that this submission is my own work and to the best of my knowledge it contains no materials previously published or written by another person, or substantial proportions of material which have been accepted for the award of any other degree or diploma at UNSW or any other educational institution, except where due acknowledgement is made in the thesis. Any contribution made to the research by others, with whom I have worked at UNSW or elsewhere, is explicitly acknowledged in the thesis. I also declare that the intellectual content of this thesis is the product of my own work, except to the extent that assistance from others in the project's design and conception or in style, presentation and linguistic expression is acknowledged.'

Signed

Date

COPYRIGHT STATEMENT

Signed

Date

AUTHENTICITY STATEMENT

‘I certify that the Library deposit digital copy is a direct equivalent of the final officially approved version of my thesis. No emendation of content has occurred and if there are any minor variations in formatting, they are the result of the conversion to digital format.’

Signed

Date

THESIS ABSTRACT

Hot Carrier Solar Cell (HC-SC) is one of the advanced photovoltaic technologies. The two main building blocks of a HC-SC are: the absorber, where electrons- holes pairs are photo generated by absorbing the incoming photons, and the energy selective contacts, which allow extraction of these carriers to the external circuit in a narrow range of energies. HC-SCs offer the possibility of operating at very high efficiencies (Limiting efficiency above 65% for un-concentrated light) with structure of reduced complexity. An ideal HC-SC operates at very high efficiency by absorbing wide range of photon energies and extracting the photo-generated carriers at elevated temperatures before they thermalize to the band-edge of the absorber material. The finding of suitable absorber material and its fabrication along with characterisation are the initial steps to implement the HC-SC with a better efficiency. Germanium Carbide (GeC) and Zirconium nitride (ZrN) have a large mass difference between their consecutive elements and exhibit a large phonon band gap sufficient to block the dominant carrier cooling mechanism by Klemens decay route. In this thesis, GeC and ZrN have been studied to investigate their suitability as absorbers for HC-SCs. These material have been fabricated using sputtering and characterised using an array of techniques such as X-ray photoelectron spectroscopy, transmission microscopy, X-ray diffraction, Raman spectroscopy, Atomic Force Microscopy and optical absorption spectroscopy to study structural, compositional and optical properties. Transient absorption spectroscopy was used to study the carrier dynamics. Nano-crystalline GeC has been fabricated which may be suitable for photovoltaic application. Germanium carbide with the record of 15.5 % GeC has been demonstrated. Growth of ZrN have been demonstrated in the range of process parameters. Epitaxial growth of ZrN on MgO substrate has been achieved with DC sputtering at 500°C. Carrier dynamics in ZRN film have been investigated with ultrafast transient absorption measurements which have indicated a long relaxation time of order of hundreds of picoseconds. The finding in the thesis provide initial insight into the properties of GeC and ZrN and show the possibilities of these materials as an absorber for the HC-SC.

Acknowledgements

This work has been supported by many people. It is now my great pleasure to express my gratitude to them.

I would like to express my deepest gratitude to my supervisors, Dr. Santosh Shrestha for allowing me to work on this challenging and exciting project. I am grateful for his trust and guidance that he gave me throughout the duration of this project. This allowed me to investigate aspects of the project that interested me the most, keeping my curiosity always at high levels. I very much appreciate his helpful discussions, suggestions, encouragements and efforts relating to my research work.

I would like to thank my co-supervisor Professor Gavin Conibeer for his precious advices, useful suggestions and discussions. I am also grateful to him for his scientific and punctual guidance during the crucial moments of my research. It has been great honour to one of his student.

A special thank goes to Hongze Xia. I appreciated his great help for the computation of numerical results, presented in the third and fifth chapter of this thesis.

I thank Dr. Pasquale Aliberti and Dr. Binesh Putthen Vettill for the series of very helpful discussions on the characterization results. Special Thanks to Dr Shujuan Huang for the discussion on XRD and TEM results. Great thanks to Dr. Bill Gong for the XPS measurements. I am also thankful to the entire LDOT team of the SPREE for being so efficient in keeping the laboratories in such an amazing working order.

I extend my thanks to all my friends, especially Dr. Yuanxuan Liao, Dr. Suntrana Smyth, Dr. Ibraheem Ali Mansorri, Dr. Ning Song, Dr. Yajie (Jessica) Yang, Dr. Xialoei, Xi Dai, Simon Chung, Dr. Craig Johnson, Dr. Supriya Pillai, for their great company throughout the year.

I am also grateful to all my students of “introduction to electronic devices” for making my teaching activity at UNSW such a rewarding experience.

I am thankful to the University of New South Wales for awarding me an APA (Australian post graduate award), such a prestigious scholarship, which allowed me to enjoy this

remarkable and unforgettable time. Finally, I thank everyone at the School of Photovoltaics and Renewable Energy during my study.

Heartfelt thanks to my Husband, my in-laws, my kids, my parents, sisters and brother for their love and wonderful support.

“As far as the laws of mathematics refer to reality, they are not certain, and as far as they are certain, they do not refer to reality.”

Albert Einstein

Contents.

List of Figures

List of Tables

Chapter 1

Introduction

This chapter presents the impetus for this thesis. It also introduces the various photovoltaic loss mechanisms which restrict the efficiency of the p-n junction solar cells. It then provides an overview of different solar cell approaches to increase the efficiency of solar cells. It also reviews advanced photovoltaic concept, especially the hot carrier solar cell. The background and significance of this thesis are also presented.

1.1. Motivation

During the last two hundred years, the global economic growth has been fuelled primarily by the conventional fossil fuels such as coal, oil and natural gas. The wide use of fossil fuels contributes to the excessive CO_2 emission which is regarded as the main cause of climate change. In order to satisfy the economic growth in a sustainable manner, the energy source needs to shift from pollution intensive fossil fuels to the clean and abundant renewable energy. The photovoltaic technology is considered to be the most promising renewable energy source. The international energy association predicts that the global energy need can be satisfied if only 4 percent of earth's surface is covered by photovoltaic systems [1].

Recent studies have predicted that the total energy consumption would increase by 48 percent (1.71 percent per year), from 158 trillion kilowatt hours in 2012 to 239 trillion kilowatt hours in 2040.[1] The use of all energy sources is predicted to increase. The access to fossil fuels, in particular, liquid fuels and petroleum will become more

complicated and expensive, thus the consumption of oil is predicted to grow at a very slow rate. Renewables are the world's fastest-growing energy source over the projection period from 2012 to 2040. Renewable energy consumption increases by an average 2.6 % /year between 2012 and 2040.[1]

A large growth in energy generation from renewable sources is expected to meet the increment in energy demand in the next decades. The renewable energy production is projected to grow from 20.5 trillion kilowatt hours in 2012 to 41.2 trillion kilowatt hours in 2040. Currently (2016) hydroelectricity and wind energy represent the largest renewable sources, accounting for 75 percent of renewable energy production [1]. A large growth of wind and hydro is forecast for China and Canada, whereas other forms of renewable energies are predicted to increase in other parts of the world.

Despite the recent growth of the solar energy market, the wholesale cost/watt figure of solar modules is still very high compared to a conventional energy sources and other renewable energies such as hydro and wind. To allow an even wider spread of solar generated energy, photovoltaic energy in particular, devices with higher efficiencies and lower production costs need to be developed. The investigation of absorber material for advance photovoltaic concepts, which will allow higher efficiency at lower prices, is the objective of the current research in "Advanced photovoltaics".

1.2. Photovoltaic devices and various losses

Photovoltaic devices or solar cells convert solar energy directly into electrical energy. The first silicon solar cell, developed in 1954 by Chapin et. al. was an inevitable result of the invention of the p-n junction diode in 1949 [2]. Chapin's silicon solar cell displayed an efficiency of 6 % [2]. Since then researchers have been attempting to

increase the efficiency of solar cells to meet the growing demands for clean energy. A range of different materials, designs and concepts have been experimented in the bid to devise cheapest and efficient solar cell. The passivated emitter with rear locally diffused (PERL) cell developed at University of New South Wales (UNSW), is a good example which achieved 25 % conversion efficiency [3]. This system has almost reached the theoretical efficiency of 29 % for crystalline Si solar cell [4]. Recently, UNSW reported 40 % energy conversion efficiency from spectrum splitting [5]. Electricity generated from the solar cells is clean and renewable as the energy source, the sun, is virtually inexhaustible. It even produces greenhouse gases, such as carbon dioxide, that contribute to global warming. The greenhouse gas such as CO_2 emission from solar PV is significantly low as compared to using coals [1]. Furthermore, solar cells can be integrated into existing built environments increasing the efficacy of space management.

Photovoltaic cells can be realized using different material and configurations, a large part of a conventional solar cell is based on crystalline and polycrystalline Si [6]. Solar cell's design consists of a p-n junction semiconductor device where the incident photons with energies greater than the bandgap of the semiconductor generates electron-hole pairs. These electron-hole pairs drift away in opposite direction by the internal electric field in a depletion region and are collected on either side of it. The electron are directed to the external circuit through contact for generating power.

Typical single p-n junction solar cells have various losses as shown in Figure 1.2.1 which limit the efficiency:

- Sub bandgap losses when Eph*<Eg* (1)
- Thermalisation loss due to absorption of high energy photons (2)

- Junction losses (3)
- Contact losses (4)
- Recombination losses (5)

* Eph = photon energy, * Eg = Bandgap

Advance photovoltaic concepts aim to attain high conversion efficiency by minimizing the different loss mechanism that occur in p-n junction solar cells. When a photon is absorbed by a photovoltaic device, it excites an electron from the valence band to the conduction band, leaving behind a hole in the valence band. The electron and holes are therefore each associated with a chemical potential which enables power generation in the solar cells. When the incoming photons have much higher energy than the band gap of the absorbing material (1.1 eV in Si), electrons and holes are excited well above the conduction and valence band edges respectively. Electrons cool down by emitting phonons to the material and come down to the energy of conduction band edge. Similarly, holes cool down to the valence band edge by emitting phonons to the lattice. The phonons thus emitted contribute to the heating of the material, thus extra energy from photons is lost as a heat to the lattice rather than converting to the output power. This mechanism is shown in Figure 1.2.1 as (2). This loss process alone limits the efficiency of a cell to approximately 44 % [7]. The second main loss is the sub-bandgap loss when photon energy is less than bandgap energy which accounts for about 30% of loss. This mechanism is shown as (1) in Figure 1.2.1. Another major loss mechanism, shown as (5) in Figure 1.2.2, represents the recombination of generated electron-hole pairs, either radiatively or non-radiatively. The rate of recombination process can be reduced by using defect free material in order to minimise recombination centres, or by surface passivation or hydrogenation steps during fabrication. Junction loss and contact

losses labelled as (3) and (4) respectively in Figure 1.2.1 are much smaller in principle and can be minimised through optimisation of cell design and processing.

Losses, specially sub- bandgap and/or thermalization, cannot be overcome as these are the intrinsic properties of the semiconductor material limiting the theoretical conversion efficiency of the solar cells. It is necessary to alleviate dominant losses; thereby a few approaches such as advance photovoltaic concepts have been proposed to tackle these two main problems and to exceed the Shockley-Queisser photovoltaic efficiency limit.

Theory for utilizing the energy lost by mechanism (1) and (2) comprises the majority of the advance photovoltaic concept.

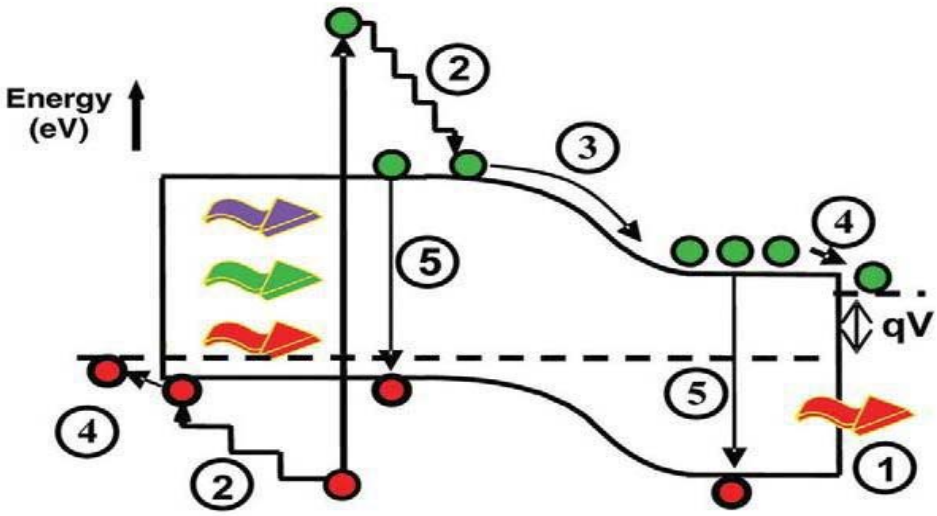

Figure 1.2.1: Loss processes in a standard p-n junction solar cell: (1) Sub-band gap losses; (2) thermalisation loss; (3) and (4) junction and contact voltage losses; (5) Recombination loss. Reproduced from [7]

1.3. A summary of three generations of photovoltaic cells

Photovoltaic cells can be broadly classified into three generations based on the concept, material and manufacturing technology used.

1.3.1. Crystalline Si wafers based solar cells

Crystalline Si wafers based solar cells have dominated the commercial photovoltaic market since Si has many advantages including abundance, nontoxicity and mature processing technologies compared to other semiconductor materials. Silicon wafer based solar cells have a characteristic feature of high quality and high efficiency (in the range of 21.2-25.6 % for industrial grade solar cells) [8]. The materials used may be mono-crystalline, multi-crystalline or ribbon silicon. A large amount of high-quality material accounts for the relatively high cost of this technology [9].

1.3.2. Thin film solar cells

For the thin film PV technology, base material is glass instead of silicon wafers and the thickness of the absorbing material is between a few hundred nanometres to tens of micrometres. Hence the amount of absorber materials required for these photovoltaic devices is significantly less. But this development has come at a cost. The efficiency of thin film solar cells is lower compared to crystalline silicon solar cells due to the presence of many defects due to the processing of material. Typically, the materials used in thin film solar technology are amorphous silicon or crystalline thin film silicon, CIGS (Copper Indium Gallium di-Selenide), Cadmium Telluride (CdTe) or organic materials. Recently, CdTe thin film solar cell is reported by Newport test centre with an efficiency of 21.0 ± 0.4 % [8]. 10.2 % conversion efficiency for single junction

amorphous silicon solar cell was reported in 2016 [8]. Over 10% conversion efficiency is achieved in 2μm poly crystalline silicon and, as a tandem of micro crystalline silicon and amorphous silicon (thin film silicon hybrid or Micromorph solar cell), 14.7 % efficiency is recorded [10].

1.3.3. Advanced photovoltaic concepts

The main sources of losses in conventional solar cells mentioned in section 1.2 are due to inability of collecting photons with energy below the bandgap, the very low conversion efficiency of photons with energy above the bandgap (thermalisation losses), the re-emission of photons by radiative recombination and losses related to carrier recombination in different parts of the device. The interaction of these loss mechanisms gives rise to an intrinsic efficiency limit for single junction solar cells. This limit is known as the Shockley Queisser limit and is around 28 percent for conventional c-Si solar cells [4], for a 6000 K blackbody incoming radiation. The Shockley-Queisser limit is very different from the thermodynamic limit for solar energy conversion, which was first calculated by Landsberg to be above 90 percent [11].

The wide gap between the Landsberg limit [11] and the single junction Shockley Queisser limit indicates that there is a large amount of room for further improvements of photovoltaic devices. Research in high efficiency photovoltaics and “advanced photovoltaics” have the aim of engineering solar cells with efficiencies higher than the Shockley Queisser limit, using design solutions which are not bound to the single junction approach. Some of these novel devices include tandem solar cells, quantum dot solar cells, intermediate band solar cells, up-conversion and hot carrier solar cells (HCSC) [13, 14]. These solar cell concepts are designed to minimize one or more of the

loss mechanisms shown in Figure 1.2.1. Hence, advance photovoltaic concept aim to achieve high efficiency devices but using thin-film technology.

Tandem and Hot carrier solar cells (HCSCs) are two major approaches in the advance photovoltaic technologies aim to tackle sub bandgap and thermalisation losses in single band gap solar cells. Another main advance solar cell concept is the intermediate band (IB) solar cell, was developed by Luque and Marti in 1997 [12], with a proposed efficiency over 40 %. IBs are being researched using the mini-bands in QDs, usually InAs QDs in InGaAs [13] and in the split-off bands of highly mismatched alloys such as Mn in GaAs [14] or II-VI compounds heavily doped with transition metals. However, IB cells are not considered further in this thesis.

1.4. Tandem solar cell

Tandem solar cell is a unique form of solar cells consisting of two or more sub cells, which are able to selectively absorb sunlight spectrum with high absorbance. They are stacked on top of each other with an ascending band gap from low to high, from which multi-layer heterojunction could be constructed. The fundamental efficiency of a single junction silicon solar cell is limited to 31 % [4], while by implementing 2 or 3 tandem stacking cells with careful selection of their band gap the limitation will increase to 42.5 % and 47.5 % respectively. For a dual tandem, the top cell's optimal band gap is 1.7-1.8 eV with a silicon cell with 1.1 eV band gap underneath. For three tandem devices, the upper and interlayer cells' band gap should be 2.0 eV and 1.5 eV [15]. Tandem cells are the only successfully implemented advance photovoltaic solar cells to date to surpass the theoretically efficiency limits for single junction solar cell. A triple junction tandem cell, InGaP/GaAs/InGaAs, with reported efficiency of 44.4 ± 2.6 % and four junction

GaInP/GaAs/GaInAsP/GaInAswith an efficiency of 43.4 ± 2.4 % have been achieved [8]. Four junction wafer bonded solar cells have been reported in 2014 with an improved efficiency of 46.5 % by Fraunhofer ISE [16].

1.5. Hot carrier solar cell

HCSC, as schematically shown in Figure 1.5.1(a) is a promising advance photovoltaic device. The first analysis of HCSC appeared in 1982 [17]. In this work, it was shown that under direct sunlight (when the solid angle, over which light is emitted and received = solid angle of the sun), HCSCs have a limiting efficiency of 85.4 % [17]. A later analysis done by M.A. Green showed a theoretical efficiency of 65.4 % can be achieved from global sunlight (when the angle of the sun = 10^{-5} θ, i.e. 1 sun) [15]. Thus, HCSC devices can in principle reach efficiency almost as high as an infinite tandem cell.

The two basic requirements necessary to implement HCSC are:

a) The absorber material, which has to slow down the thermalisation of carriers, by minimizing the carriers-phonons interactions.
b) The energy selective contacts (ESCs), which have to allow extraction of carriers only in a very narrow range of energies [18].

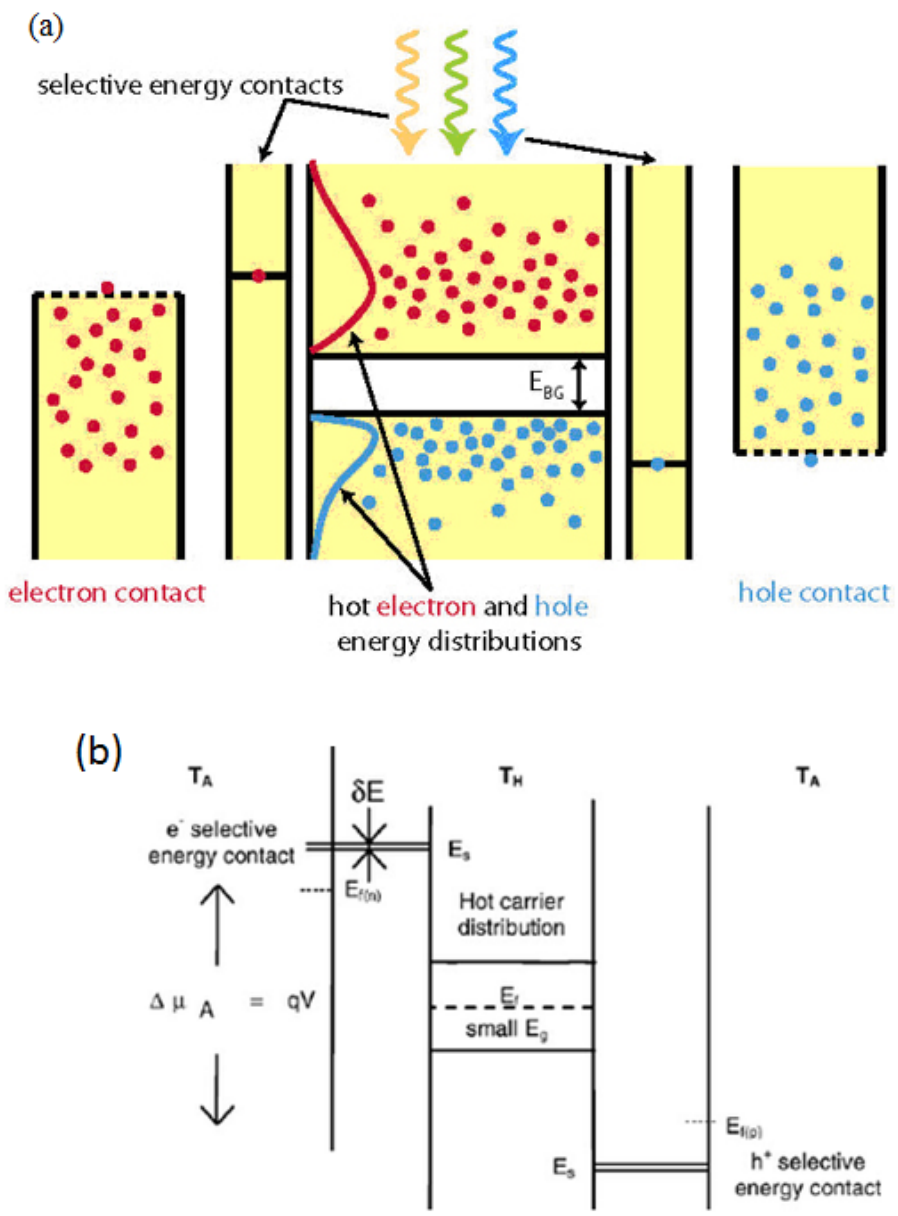

Figure 1.5.1: a) Band diagram of an ideal hot carrier solar cell. [19] b) The absorber has a hot carrier distribution at temp T_H. Carriers cool isoentropically in the mono-energetic contacts to T_A. The difference of the Fermi levels of these two contacts is manifested as a difference in chemical potential of the carriers at each contact and hence an external voltage, V [20].

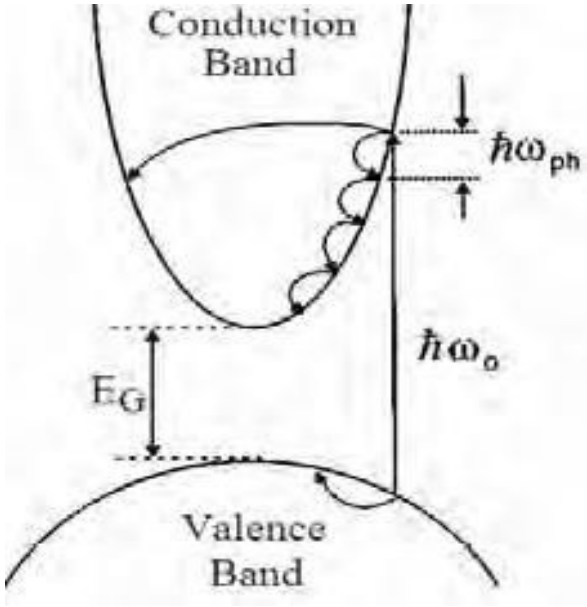

Figure 1.5.2: Schematic illustration of an electron-hole pair creation, following absorption of a photon with energy $h\omega_0$. Energy relaxation follows via optical phonons emission ($h\omega_{ph}$). Adopted from [21] .

Low wavelength photons, once absorbed, generate highly energetic electron hole (e-h) pairs; these are extracted before they are thermalised towards respective band edges, losing their excess kinetic energy. HCSCs make use of the extra energy of electrons and holes above the band edges of the absorber material by converting it into electrical power instead of letting it heat up the lattice through the emission of phonons. In HCSCs the excited electrons and holes find equilibrium energetic states among themselves rather than cooling down to the edge of the conduction band and the valence band respectively. This equilibrium is reached via carrier-carrier elastic scattering rather than carrier-lattice inelastic collisions. Thus, carriers in HCSCs are at elevated energy levels allowing it to operate at a higher voltage [22]. The interaction of carriers with phonons forces them to thermalise towards band edges as shown in Figure 1.5.2. In general, the energy is lost by successive interactions with optical phonons. Recent

theoretical works on HCSCs operating under practical conditions have given efficiencies using real material parameters is estimated to be 43-45 % at 1000 sun [23-25]. The processes in which hot carriers in semiconductors are involved after excitation are schematized in Figure 1.5.3. If the interaction of optical and acoustic phonons is much slower than the carrier to optical phonon interaction, large non-equilibrium optical phonon populations can be generated, slowing energy relaxation of the hot carriers (hot phonon re-absorption) [20, 26].

The energy dissipation of photo-generated carriers is a multi-step process. The inelastic scattering of carriers takes place in the first few 10s of femtoseconds after their generation. This process normalizes momentum and leads to a distribution of electron energies which can be described by a Boltzman distribution and a single high temperature, i.e. a thermal population, and a separate low temperature thermal population of holes [27]. Then on a longer timescale (typically several picoseconds) carrier's scatter inelastically with phonons, predominantly emitting optical phonons in a series of discrete hops in each of which energy and momentum are conserved in the combination of electron and emitted phonon. For polar semiconductors the major scattering process is with longitudinal optical phonon modes. These optical phonons emitted by the excited carriers then interact with other phonons due to the anharmonic nature of the crystal potential. Through various routes these over-populated optical phonons decay into low-energy acoustic phonons. The final step is the transport of these acoustic phonons, macroscopically marked as the heat dissipation to the environment. The carrier cooling process can be slowed by blocking any of these three processes.

The cooling of carriers by emission of optical phonons leads to the build-up of a non-equilibrium 'hot' population of optical phonons which, if it remains hot, will drive a reverse reaction to re-heat the carrier population, thus slowing further carrier cooling. Therefore the critical factor is the mechanism by which these optical phonons decay into acoustic phonons, or heat in the lattice. The principal mechanism by which this can occur is the Klemens mechanism, in which the optical phonon decays into two acoustic phonons of half its energy and of equal and opposite momenta [28]. The accumulation of emitted optical phonons is strongly peaked at zone centre both for compound semiconductor due to the Fröhlich interaction (strong quadratic dependence on momentum) and for elemental semiconductors due to the deformation potential interaction (less strong linear dependence on momentum). The strong coupling of the Fröhlich interaction also means that high energy optical phonons are also constrained to near zone centre even if parabolicty of the bands is no longer valid as is the case for high energy carriers well above the band minima. This zone centre optical phonon population determines that the dominant optical phonon decay mechanism is this pure Klemens decay.

For a binary material, a simple 1D phonon frequency calculation assuming simple harmonic oscillators is given below [20] for highest acoustic phonon and lowest optical phonon dispersion:

$$\omega_{\mathrm{acoustic}} = \sqrt{\frac{2T}{a}\frac{1}{M}},$$

$$\omega_{\mathrm{optical(min)}} = \sqrt{\frac{2T}{a}\frac{1}{m}} \quad \text{and}$$

$$\omega_{optical(max)}=\sqrt{\frac{2T}{a}\left[\frac{1}{m}+\frac{1}{M}\right]}$$

Where T/a is the force constant, M and m are heavy and light atomic masses of the compound respectively.

By substituting atomic masses for each element and normalizing the energy difference between highest acoustic and lowest optical dispersion branch, the normalized phononic band gap is obtained. Theoretically, the normalized band gap just larger than 1 should be enough for preventing Klemens mechanism, but in a realistic situation, larger than ones could also prevent any perturbation and defects effect. In addition, Ridley mechanism is another mechanism by which longitudinal optical (LO) phonons decay at zone centres into a transverse optical (TO) phonon and emit a longitude acoustic (LA) phonon. This indicates the energy dispersion between optical modes must be small.

Additionally, selective energy contacts (ESC) enable the hot carrier device to extract the carriers with specific energy to the external circuit [18, 20, 29]. The requirement of an ESC is that it should have a narrow band within a large bandgap semiconductor which permits only carriers in a narrow energy range to be transmitted, electrons in one contact and holes in the other. Figure 1.5.1(b) demonstrates the band diagram for a hot carrier cell with absorber and ESCs. As can be seen, electrons are transferred from the absorber material to the ESCs through a narrow energy. These electrons elastically interact with other hot electrons in the absorber material and normalize their energy. Holes are collected to the external contact at the positive side of the cell through a similar mechanism.

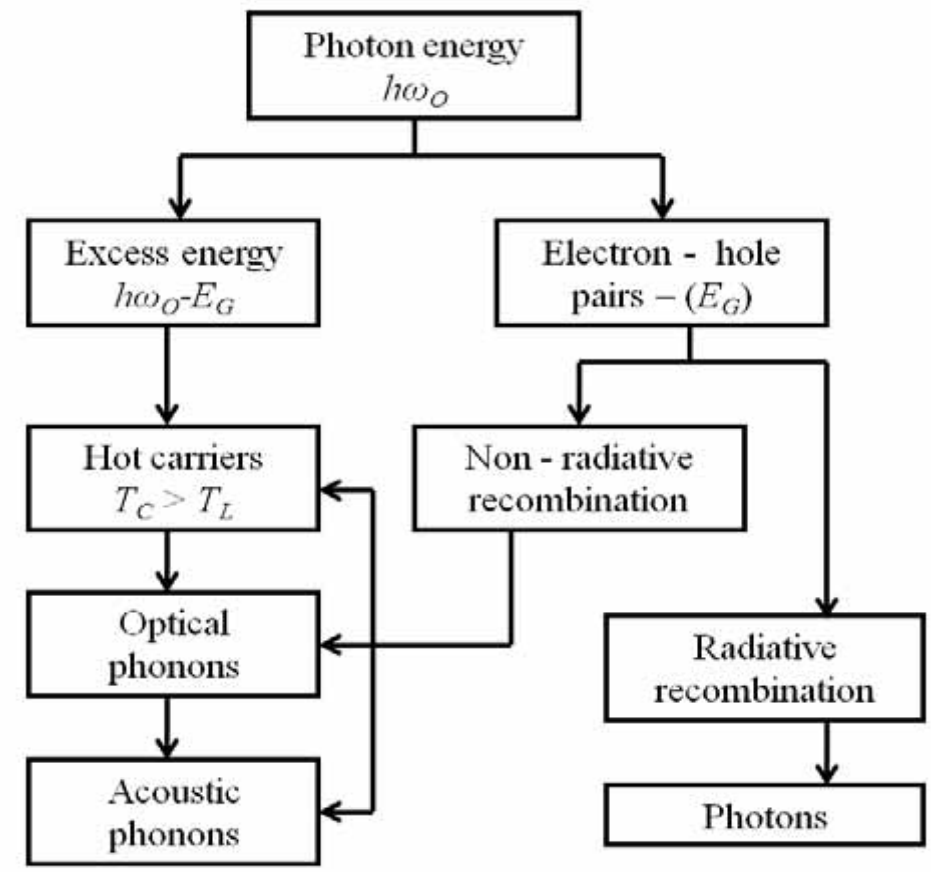

Figure 1.5.3: Energy flowchart in photo excited semiconductor [21]

A possible method of implementing ESC structures is by using the, double barrier structures consisting of quantum dots (QDs) or a quantum well (QW) [18] in an insulating dielectric oxide or nitride matrix were investigated. The QDs/QWs provide a discrete energy level between two insulating barriers which is expected to give conduction of carriers strongly peaked at these particular energy levels, but much lower at other energies – hence selecting a particular energy level. The position of the peak and the selectivity can be tuned by carefully choosing the QD size and the insulating barrier thickness of the contacts. ESC structures using SiO_2/Si QW/SiO_2, Al_2O_3/ Ge QW / Al_2O_3 and Al_2O_3/ Ge QD / Al_2O_3 have been investigated [30, 31].

1.5.1. Requisite properties for absorber material

The major properties required for a good hot carrier absorber material suggested [26, 32, 33] are listed below in approximate order of priority, although their relative significance may well modified in light of impending research:

1. Large phononic band gap (E_O (min) - E_{LA}) - to suppress Klemens' decay, requires large mass difference between elements.
2. Narrow optical phonon energy dispersion (E_{LO} - E_O (min)) – to minimise the loss by Ridley decay, requires a high symmetry.
3. Small E_g < 1eV – to allow a broad range of strong photon absorption.
4. A small LO optical phonon energy (E_{LO}) – to reduce the amount of energy lost per LO phonon emission but not so small as to increase the occupancy of LO modes unduly. (E_{LO}.exp(-E_{LO}/kT)
5. A small maximum acoustic phonon energy (E_{LA}). This maximises (E_O(min) - E_{LA}) and is important if E_{LO} is also small.
6. Good renormalisation rates in the material, i.e. good e-e and h-h scattering. This condition is met in most semiconductors quite easily, with e-e scattering rates of less than 100 fs. But it may be compromised in nanostructures.
7. To allow good carrier transport of hot carriers to the contacts, optical absorption depth should be shorter than the transport distance in the absorber.
8. Ability to make good quality, ordered, low defect material.
9. Earth abundant and readily processable materials.
10. No, or low, toxicity of elements, compounds and processes.

* E_{LO}, $E_{O(min)}$ & E_{LA} are the maximum optical, minimum optical and maximum acoustic phonon energies. In μT where μ is the mobility and T is the Temperature

For HCSCs, in addition to absorbing the photons and creating the electron hole pairs, the absorber materials need to block the Klemens mechanism to increase the chances of phonon reabsorption by cold electrons. A large phonon band-gap is the essential feature for the absorber to show a phonon bottleneck effect. A large phonon band-gap increases the lifetimes of high energy phonons by inhibiting fast decay paths. The required phononic properties can be realized through carefully engineered nanostructure super lattices. Theoretically, the lifetime of high energy phonons is found to be hundreds of picoseconds for certain symmetry directions for diamond super lattices [34]. Some bulk materials have shown slow carrier cooling and considered good candidate as an absorber for HCSCs. InN is an example of such material with a large phonon bandgap [35]. The effectiveness of InN as a hot carrier absorber material still has to be properly assessed because it is a very difficult material to grow at reasonable quality, again due to the disparity in size of its constituent element atoms [20]. In addition, InN is predominantly grown as hexagonal wurtzite material rather than the more symmetric cubic zinc-blende structure, although growth of cubic InN is possible [36]. Furthermore, the abundance of In is very low, so it is difficult to see InN as a long term material suitable for large scale implementation. Hence analogues of InN, which retain its interesting property of a large phonon band gap, need to be investigated. So, the focus has been on realizing bulk material as an absorber materials using Group IV alloys and transition metal nitride which are reasonably abundant [32, 33, 37, 38]. However, obtaining reasonable good absorber material using these materials is still a challenging task, since it requires a very high quality film.

An investigation on properties of germanium carbide and zirconium metal nitride after fabrication using sputtering method is presented in this thesis.

1.6. Aim and structure of this thesis

The main aim of this thesis is to investigate the different materials from group IV alloys and transition metals' nitride as an absorber material for HCSCs. The work includes the fabrication and characterization of materials especially germanium carbide and zirconium nitride as an absorber using an industry-friendly process called sputtering and analyses their properties for photovoltaic applications.

The thesis is divided into six chapters. At the beginning of each chapter, a comprehensive review of the literature on that specific topic and at the end, a summary of the key results is reported.

The structure of the thesis is designed as follows:

- Chapter 1 provides an overview of different solar cell approaches and various photovoltaic loss mechanism which restrict the efficiency of solar cells.
- In Chapter 2, the literature review on group IV alloys and transition metal nitride is presented. Potential bulk material as hot carrier absorber is also discussed.
- Chapter 3 is dedicated to the experimental investigation of germanium carbide as a hot carrier absorber material. Properties of germanium carbide film deposited using industry friendly process called sputtering are investigated. Nanocrystalline growth of Ge_xC_{1-x} is also presented.
- In Chapter 4 deposition and characterization of zirconium nitride films using RF and DC sputtering are presented. Polycrystalline and single crystal growth of zirconium nitride films are discussed.

- Chapter 5 is written on the ultrafast carrier dynamics study on deposited zirconium nitride. In this study, hundreds of picoseconds decay time constant in zirconium nitride film, which could be assumed as a carrier cooling time, is observed.
- Chapter 6 is dedicated to conclusions of chapter 3, 4 and 5. This chapter outlines the current state of research on HCSCs and highlights the different areas and directions where future research should be focused.
- Sample processing and characterization details are given in Appendix A, B and C respectively.
- A publication list has been presented in Appendix D.

1.7. Bibliography

1. Administration, U.S.E.I., *International Energy Outlook*. 2016: Washington DC.
2. Chapin, D.M., C.S. Fuller, and G.L. Pearson, *A New Silicon p-n Junction Photocell for Converting Solar Radiation into Electrical Power.* Journal of Applied Physics, 1954. **25**(5): p. 676-677.
3. Zhao, J., A. Wang, and M.A. Green, *24·5% Efficiency silicon PERT cells on MCZ substrates and 24·7% efficiency PERL cells on FZ substrates.* Progress in Photovoltaics: Research and Applications, 1999. **7**(6): p. 471-474.
4. Shockley, W. and H.J. Queisser, *Detailed Balance Limit of Efficiency of p-n Junction Solar Cells.* Journal of Applied Physics, 1961. **32**(3): p. 510-519.
5. Crozier, R. *UNSW researchers set world record in solar energy efficiency*. 2014.
6. Ginley, D., M.A. Green, and R. Collins, *Solar Energy Conversion Toward 1 Terawatt.* MRS Bulletin, 2008. **33**(04): p. 355-364.
7. Conibeer, G., *Third-generation photovoltaics.* Materials Today, 2007. **10**(11): p. 42-50.
8. Green, M.A., et al., *Solar cell efficiency tables (version 47).* Progress in Photovoltaics: Research and Applications, 2016. **24**(1): p. 3-11.
9. Bruton, T.M., G. Luthardt, K.D. Rasch, K. Roy, I.A. Dorrity, B. Garrard, L., J.A. Teale, U. Ugalde, K. Declerq, J. Nijs, J. Szlufcik, A. Rauber, W., and a.A.V. Wettling. *A study of the manufacture at 500MWp p.a. of crystalline silicon photovoltaic modules*. in *14th European Photovoltaic Solar Energy Conference*. 1997. Barcelona.
10. Yoshimi, M., et al. *High efficiency thin film silicon hybrid solar cell module on 1 m/sup 2/-class large area substrate*. in *Photovoltaic Energy Conversion, 2003. Proceedings of 3rd World Conference on*. 2003.
11. Landsberg, P.T.a.G.T., *Thermodynamic energy conversion efficiencies.* Journal of Applied Physics, 1980. **51**(7): p. R1-R20.
12. Luque, A. and A. Martí, *Increasing the Efficiency of Ideal Solar Cells by Photon Induced Transitions at Intermediate Levels.* Physical Review Letters, 1997. **78**(26): p. 5014-5017.
13. Luque, A., et al., *Experimental analysis of the quasi-Fermi level split in quantum dot intermediate-band solar cells.* Applied Physics Letters, 2005. **87**(8): p. 083505.
14. Yu, K.M., et al., *Effect of the location of Mn sites in ferromagnetic Ga1-xMnxAs on its Curie temperature.* Physical Review B, 2002. **65**(20): p. 201303.
15. Green, M.A., *Third Generation Photovoltaics : Advanced Solar Energy Conversion*, ed. Springer-Verlag. 2003, Berlin and Heidelberg GmbH & Co. KG.
16. ISE, F.-I.f.S.E., *New world record for solar cell efficiency at 46 % French-German cooperation confirms competitive advantage of European photovoltaic industry*. 2014.
17. Ross, R.T. and A.J. Nozik, *Efficiency of hot-carrier solar energy converters.* Journal of Applied Physics, 1982. **53**(5): p. 3813-3818.
18. Shrestha, S.K., P. Aliberti, and G.J. Conibeer, *Energy selective contacts for hot carrier solar cells.* Solar Energy Materials and Solar Cells, 2010. **94**(9): p. 1546-1550.
19. Gavin Conibeer, M.G., *Hot Carrier Solar Cell: Implementation of the Ultimate Photovoltaic Converter*. 2008, Standford University: Global Climate & Energy Project
20. Conibeer, G.J., et al., *Slowing of carrier cooling in hot carrier solar cells.* Thin Solid Films, 2008. **516**(20): p. 6948-6953.
21. Othonos, A., *Probing ultrafast carrier and phonon dynamics in semiconductors.* Journal of Applied Physics, 1998. **83**(4): p. 1789-1830.

22. Würfel, P., *Solar energy conversion with hot electrons from impact ionisation.* Solar Energy Materials and Solar Cells, 1997. **46**(1): p. 43-52.
23. Yasuhiko, T., et al., *Practical Factors Lowering Conversion Efficiency of Hot Carrier Solar Cells.* Applied Physics Express, 2010. **3**(10): p. 104301.
24. Aliberti, P., et al., *Investigation of theoretical efficiency limit of hot carriers solar cells with a bulk indium nitride absorber.* Journal of Applied Physics, 2010. **108**(9): p. 094507.
25. Takeda, Y., et al., *Hot carrier solar cells operating under practical conditions.* Journal of Applied Physics, 2009. **105**(7): p. 074905.
26. Conibeer, G., et al., *Hot carrier solar cell absorber prerequisites and candidate material systems.* Solar Energy Materials and Solar Cells, 2014(0).
27. Administration, U.S.E.I. *International Energy Outlook*. 2014.
28. Klemens, P.G., *Anharmonic Decay of Optical Phonons.* Physical Review, 1966. **148**(2): p. 845-848.
29. Conibeer, G.J., et al., *Selective energy contacts for hot carrier solar cells.* Thin Solid Films, 2008. **516**(20): p. 6968-6973.
30. Liao, Y., *Energy Selective Contacts Based on Quantum Well Structures of Al2O3 and Group IV Materials for Hot Carrier Solar Cells*, in *Photovoltaics & Renewable Energy Engineering*. 2014, University of New South Wales.
31. Shrestha, S.K., et al., *Energy selective contacts for hot carrier solar cells.* Solar Energy Materials and Solar Cells, 2010. **94**(9): p. 1546-1550.
32. Conibeer, G., et al., *Hot carrier solar cell absorber prerequisites and candidate material systems.* Solar Energy Materials and Solar Cells, 2015. **135**(0): p. 124-129.
33. Conibeer, G., et al. *Hot carrier solar cell absorbers: materials, mechanisms and nanostructures*. 2014.
34. Patterson, R., et al., *Phonon lifetimes in model quantum dot superlattice systems with applications to the hot carrier solar cell.* Solar Energy Materials and Solar Cells, 2010. **94**(11): p. 1931-1935.
35. Chen, F., et al., *Time-resolved spectroscopy of recombination and relaxation dynamics in InN.* Applied Physics Letters, 2003. **83**(24): p. 4984-4986.
36. Cimalla, V., et al., *Growth of cubic InN on r-plane sapphire.* Applied Physics Letters, 2003. **83**(17): p. 3468-3470.
37. Shrestha, S., et al. *Evaluation of hafnium nitride and zirconium nitride as Hot Carrier absorber*. in *Photovoltaic Specialist Conference (PVSC), 2014 IEEE 40th*. 2014.
38. Chung, S., et al., *Evidence for a large phononic band gap leading to slow hot carrier thermalisation.* IOP Conference Series: Materials Science and Engineering, 2014. **68**(1): p. 012002.

Chapter 2

Group IV alloys and transition metal nitrides as hot carrier absorber material

This chapter presents the literature review on Group IV alloys and transition metal nitrides. It also presents information about bulk hot carrier absorber material and familiarizes the theoretical calculation of normalised phononic bandgap and energy optical dispersion mode of various group IV alloys and refractory metal nitride.

2.1. Literature review on group IV alloy

2.1.1. Germanium-carbide alloy

Germanium is a group IV element and is a reasonably abundant element on the earth .It has been known for some time that c-Ge is a reasonably good absorber of light because of a very small separation (~0.15 eV) between the lowest L valley and the central Γ valley in the conduction band [1]. As a result, it behaves almost like a direct gap semiconductor. Unfortunately, its bandgap (~0.66 eV) is too low for efficient photovoltaic energy conversion [2]. In contrast, c-Si, which has a bandgap (1.12 eV) closer to the optimum gap for PV conversion (~1.5 eV), is a very poor absorber of light because of a large (many eV) separation between the lowest X valleys and the central Γ valley. Therefore, neither Si nor Ge can be used for efficient PV conversion in a thin film form. However, when one examines the band structures of Ge and of diamond,

with a bandgap of ~5.4 eV, it becomes apparent that a small addition of C to Ge would result in a material with a bandgap in the optimum solar range, and one would only need to add little amount of carbon to germanium to achieve such a bandgap. Upon examining the lattice constants of Ge and diamond, it also becomes apparent that the addition of a few percentage of C to Ge would reduce the lattice constant of the material to a value close to that of c-Si, thereby making $Ge_{1-x}C_x$ compatible with deposition on crystalline Si. Germanium carbide is called a man-made alloy. Due to extreme low solubility between Ge and C, it is difficult to form stable long range ordered structural GeC compounds [3, 4]. However, $Ge_{1-x}C_x$ films with 11.6 % GeC content at 250 V bias has been reported using medium frequency magnetron sputtering. It has promising application in many fields such as temperature sensor, protection layer for infrared optics and optoelectronics and as an antireflection coating [4].

GeC films have been proved to be very promising candidate in photovoltaics applications such as temperature sensors, resistant protective coating in Infrared (IR) optics. They have numerous fascinating properties like low stress and light absorption, high Young's Modulus, thermo-stability and good adhesion on many IR substrates such as Ge and ZnS. In addition, their tailoring composition can allow the tunability of a refractive index within the range of 1.5-4 and an optical band gap over wide ranges which help them in making suitable candidate for the application of multilayer antireflection and protection coating for IR windows [5-7]. Moreover, the large atomic mass difference between cations and anions may show a large "phononic band gap", which could meet the hot carrier absorber requirement [8]. Many researchers have reported the fabrication and characterization of this material by using a variety of

methods, such as sputtering [4, 9-13], molecular beam epitaxy (MBE) [14-18] and electron cyclotron resonance plasma and chemical vapour deposition (CVD) [19, 20]. These methods and valuable results obtained will be presented as follows.

Liu et al. [9] and other workers [4, 11, 13] reported the preparation of Ge_xC_{1-x} films through reactive RF sputtering method. In Liu's experiment (1997), high purity Ge (111) target was sputtered in an argon and methane mixture gas environment and films were deposited on single crystalline Si and quartz substrates. Initially, RF power and substrate temperature were 150 W and 200 ºC respectively. Pre-pumping the deposition chamber down to 5×10^{-5} Torr was necessary to drive out any contamination gases. Argon and methane gas mixture with gas flow ratio $CH_4/Ar+CH_4$ = 0.05 was fed and accurately modulated by a flow controller. During deposition, the chamber pressure was maintained around 7×10^{-3} Torr. Film surface observation by SEM and XRD analysis indicated smooth and amorphous samples were produced. AES test was conducted, and due to the impurity of the feed-in gas, oxygen peak was found.

Many research attempts further proceeded to investigate the effect of key sputter parameters [4, 11, 13] on properties of Ge_xC_{1-x} films. These parameters included flow ratio of mixed gas and RF power. The repeated experiments were carried out with different gas flow ratio, and carbon concentration information was obtained by AES. The carbon composition in a series of samples increased as the gas flow ratio increased from 25 % to nearly 100 % for 4 % to 20 % of gas flow ratio. Under this deposition condition, GeC alloy appeared at approximate 17 % gas flow ratio. By keeping gas flow ratio 20 % and 200 ºC substrate temperature, but varying the RF power from 80 W to 250 W during sputtering [12], the compositional ratio is variable so that their optical and

mechanical properties change accordingly. XPS results demonstrated that germanium content increased with the applied RF power giving 35 % and 63 % germanium with 80 W and 250 W RF power, respectively. Besides that, Hu et al [13] also found that increased RF power encouraged the formation of sp^3 hybridized carbon atoms to integrate to GeC network. The more sp^3 hybridization in the network, the more diamond like structure it would be, however by contrast, the sp^2 hybridization produces large fraction of graphite clusters, which would drastically reduce the optical and mechanical properties of GeC alloy.

XRD examinations indicated that all samples obtained were amorphous. Raman results showed broad peak between 1000-1800 cm^{-1}, which is believed to be the graphitic (G band) and disorder graphitic band (D band) peaking at 1570 cm^{-1} and 1340 cm^{-1} respectively. The intensity increases as the gas flow ratio increases indicating increased C-C bonds fraction, while smaller peak at 290 cm^{-1} corresponding to Ge-Ge bonding decreases. The refractive index has reverse dependence of gas flow ratio and the optical band gaps for these amorphous films was observed to range from 0.6-1.1 eV.

Another promising method of depositing crystalline GeC alloys is ECR plasma CVD [20]. GeC obtained from this method contains minor carbon up to 8 % and results in a wider band gap up to 1.15 eV with same high level absorption coefficient as crystalline Ge. This property is quite attractive for photovoltaic application. Niu et al. [20] used germane and methane with H ion plasma released by feed-in hydrogen gas, which can assist crystallization and passivation of GeC alloy films. The gas flow ratio of hydrogen/(germane+methane) was 20~50:1. Growth temperature and pressure were 300 ^{o}C-350 ^{o}C and 10 mTorr respectively.

2.2. Transition metal nitride

High strength and low coefficient of friction of Transition metal nitrides enables the use of this material in industries ranging from food processing to decorative coatings. They have recently been examined for photovoltaic applications. The IV-B transition metal nitrides, specifically, have been investigated for a number of years for a wide variety of applications. Produced as a thin film, they demonstrated high hardness, chemical stability, corrosion resistance, high melting point, low resistivity and low coefficient of friction. Recently, these IV-B transition metal nitrides have been also investigated as diffusion barriers in metallization schemes [21, 22], super lattice and Josephson function [23].

Zirconium nitride (ZrN) is an IVB-V compound known for extremely high hardness and appealingly pleasing gold colouration that validates properties desirable for a variety of industrial and consumer applications. ZrN exhibits superior optical properties, high hardness, wear and oxidation resistance, which makes it better than the other transition metal nitride [24]. The brilliant golden colour and resistant to wear make it enormously desirable as decorative coating in high end watches and the jewellery industry. It has achieved Federal Drug Administration (FDA) approval for use in surgical application and food preparation due to its wear resistant properties [25]. The tool and dye industry use ZrN coating for tool wear resilient. Table 2.2.1 summarizes the major technical aspects of ZrN.

Table 2.2.1 Main technical properties of ZrN.

Properties	ZrN
Hardness (Kg/mm)	4510 Kg/mm^2 [26]
Melting Point	2952K at 760 mmHg [26]
Density	7.09 g/cm^3 at 24 ^{o}C [26]
Resistivity	12.0 μΩ-cm at RT [26]
Lattice parameter	4.58 Å [26]
Superconducting Temp	10 .4K [26]
Solubility	Soluble in concentrated HF acids [26]

ZrN satisfies the Hägg rule and crystallizes in a B1-NaCl crystal structure. The Hägg rule states that the structure of transition metal hydrides, carbides, nitrides and borides is determined by calculating the ratio of the atomic radii of the interstitial element to the transition metal and then comparing with 0.59. If the ratio is less than 0.59, simple structure will be formed else complex structure. As mentioned above, the principal application of refractory metal nitrides is as a wear resistant coating, but in this research they are being considered as a potential candidate as an absorber material for advance photovoltaic such as a hot carrier solar cell.

Zirconium nitride has been fabricated by a variety of deposition techniques such as reactive magnetron sputtering: DC/RF; plasma enhanced chemical vapour deposition (PECVD), ion plating, dual ion beam sputtering, ion assisted deposition, molecular beam epitaxy, atomic layer deposition (ALD) and pulse laser deposition [24, 27-41].

One of the disadvantages of ZrN is that it reacts quickly with oxygen even at temperatures below 600 ^{o}C [39, 42]. The deposition ZrN has been done in a controlled

environment to avoid oxidation [30]. To prevent oxidation certain elements have been added, such as aluminium, carbon, nickel, copper titanium and yttrium or degassing at high temperature was used [30].

Among transition metal nitride, zirconium nitride (ZrN) films are the most attractive candidates because they have the highest heat of formation and the lowest resistivity. However; it has been generally believed that, to obtain epitaxial ZrN films on Si substrate, a fairly high substrate temperature of approximately 600-900 ºC is needed which is too high for practical use in the microelectronics industry. In addition, Barnett et al. [41] reported that cracks were observed in ZrN films prepared at a high substrate temperature because the lattice misfit between ZrN and Si is 16 % and the thermal expansion coefficient (7.24×10^{-6} / °C)(7.24×10-6 / °C) of ZrN is much higher than that of Si (2.33×10^{-6} / °C). It was also found that the film's resistivity was strongly dependent on the N_2 flow ratio and that the film crystallinities were dependent on DC power (P_{DC}) and T_s. The optimum sputtering conditions obtained for ZrN deposition were as follows: an N_2 flow ratio of 3 % and a P_{DC} of 15 W. Furthermore, epitaxial growth of high-quality stoichiometric (001) ZrN films with a resistivity of 17 μΩcm, comparable to that of bulk ZrN (13.6 μΩcm), was achieved on (001) Si under the sputtering conditions described in reference [43]. Epitaxial growth of ZrN on MgO substrate has also been reported using RF magnetron sputtering [30].

2.3. Promising bulk Hot carrier absorber materials

Figure 2.3.1 shows a comparison of the normalised phononic band gaps which is the ratio of energy difference between optical and acoustic phonons to maximum acoustic phonon energy for different compounds (filled squares). It also shows energy dispersion of optical modes which is the ratio of energy difference between maximum and minimum optical phonons to energy of acoustic phonon, (unfilled squares). For details refer to Section 1.5 of Chapter 1.

Energy dispersion of optical modes and phononic bandgap of various binary compounds is graphically represented in Figure 2.3.1. These data are calculated from 1-D force constant model treating the atoms as simple harmonic oscillators as described in reference [44]. In the materials in which the ratio of normalised phononic band gap is larger than unity, Klemens' decay mechanism is forbidden as there are no states available for decay to happen. Ridley mechanism is also blocked for those materials which also have narrower dispersion of optical phonon modes.

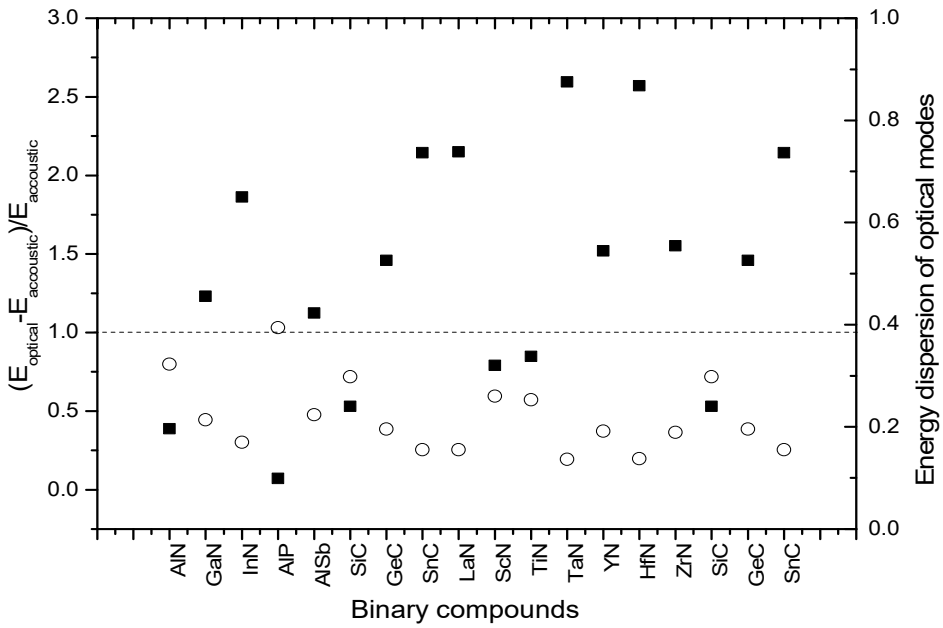

Figure 2.3.1: *Ratios of phononic bandgap energy values for various binary compounds. The filled squares represent energy gap between acoustic and optical modes normalised to acoustic frequency and the unfilled squares represent energy dispersion of optical modes. From [44].*

It is evident from Figure 2.3.1 that among the group III-V compounds, InN, GaN and AlSb have a large phononic band gap and narrow phonon dispersions suitable to block Klemens and Ridley decays. Of these materials InN has the largest phononic band gap, lowest narrowest phonon dispersion and importantly the lowest band gap of 0.7 eV. Hence InN is an ideal hot carrier absorber material. However, abundance of In is very low (~1.7 x10^6 times lower than Si). Importantly, growth of good quality InN, which is typically achieved with expensive MBE technique, is very challenging. Therefore, although InN is a model material, it is not suitable for a large scale implementation of photovoltaics.

Group IV carbides such as GeC and SnC can also have very large phonon bandgaps suitable to block the Klemens' mechanism. Their abundance is an order of magnitude larger than that of In. Theoretical studies suggest that SnC has a direct band gap of 0.75 eV but GeC has indirect bandgap over 1.4 eV [45, 46] but can be modulated with the stoichiometry of the films [12, 47], making both of these materials good choices for HC absorber. The main challenge is the growth of these materials as the solubility of C in Ge (and possibly also in Sn) is extremely low which prohibits growth of good quality GeC crystals [17]. Several methods such as Molecular Beam Epitaxy, Chemical Vapour deposition and RF sputtering have been tried to grow Ge_xC_{1-x} films with higher C content but the carbon incorporation of only up to about 11 % has been achieved [4, 12, 17, 48]. Besides, both GeC and SnC tend to form weak compounds and have low thermal stability. For hot carrier absorbers besides slow cooling rate property, lower band gap and high absorbance are desired. Low band gap corresponds to longer cut off wavelength so that the absorber material can absorb a wide range of solar spectrum, and high absorbance will enable use of thin layer of materials. As discussed below, GeSn and GeC can both exhibit lower than 1 eV band gap. However, associated with larger phononic band gap property, only GeC seems feasible among the group IV alloys.

Figure 2.3.1 shows that transition nitrides HfN, ZrN, YN and LaN can have large phononic gaps. While YN does not show suitable phononic band gap [49], wide phononic gaps in HfN and ZrN are supported by theoretical studies and also verified experimentally by inelastic neutron scattering measurement [50-52]. Both HfN and ZrN are metallic but the band gap of Hf_2N_5 is around 0.5 eV (and for Hf_3N_4 it is 0.9 eV) and that of Zr_3N_4 is between 0.6 and 0.9 eV [53] which are desirable for Hot Carrier solar cells. Abundance of Hf and Zr is also about 20 and 800 times larger than that of In. Thus

both are very attractive materials as hot carrier absorber material. This thesis will focus on ZrN.

Nitrides of hafnium and zirconium have large predicted [49] and measured phononic band gaps, as shown in Figure 2.3.1. The phononic gap for TaN is reasonable but not as large as its acoustic phonon energy, although it is a useful thermoelectric material. Hf and Ta are about the same abundance as Ge and As, with Zr 100× more abundant and all are widely used metals. ZrN not only shows a large phonon band gap (large enough to block Klemens decay completely) [52] but also a narrow optical phonon dispersion – important to block secondary Ridley decay. These nitrides can also readily be fabricated and have many existing applications, although the lack of stability of ZrN in moist air would need to be managed in a real application, probably by encapsulation. Interestingly both HfN and ZrN have zero electronic band gap, leading to the surprising conclusion that these n-type semi-metals may be good absorbers for a hot carrier cell.

2.3.1. Hot carrier generation in metal

It is important to understand how hot carriers could be generated in metals. The absorption of light occurs in metals through two main pathways, interband absorption and intraband absorption. In order for the metal to act as a zero band gap absorber the absorption should be through the intraband pathway, directly into the itinerant electron distribution. Such absorption occurs in noble metals up to relatively high threshold energy, before interband absorption is relevant. For example in Silver, all absorption below 3.8 eV occurs through intraband processes [54]. Light absorption through

intraband processes results in a heated distribution of electrons in the metal, with the temperature of this distribution depending on the total energy of the incident light [55], determined by both the photon flux and the photon energy. This heated distribution can then be exploited if it exists long enough for the electrons to reach the contact region before losing energy to the lattice. Significant work has been carried out to determine the hot carrier relaxation time in metals, using femtosecond time resolved spectroscopy to obtain the electron energy distribution at a given time the application of an ultrafast excitation pulse. It is shown by Fann [55, 56] that a laser pulse at 1.84 eV on a thin Au film initially creates a broad distribution of hot electrons from the Fermi edge up to 1.84 eV above the Fermi edge on a timescale of less than 130 fs. This distribution then evolves through electron-hole (e-p) and electron-electron (e-e) interactions into a hot thermalized distribution on a timescale of 1.3 ps. While the resulting distribution can be defined by a temperature after this time, it still remains hot in comparison with the lattice. The extraction of hot electrons from metallic regions that are less than 100 nm thick can occur on timescales of less than 100 fs [57], showing the compatibility of this particular cell structure with the hot carrier concept.

Femtosecond electron thermalization in Gold metal was investigated using transient thermomodulation transmissivity and reflectivity[58]. Studies were performed using a tunable multiple-wavelength femtosecond pump-probe technique in optically thin gold films in the low perturbation limit. Thermalization of the order of ∼1–2 ps are observed in Gold metal at energy close to the Fermi surface.

R. W. Schoenlein et. al [59] used high-intensity femtosecond laser pulses to induce non-equilibrium electron heating in gold metal. The thermal relaxation of the electronic distribution was studied through pump and continuum probe measurements of transient reflectivity.

Measurements were performed for different heating-pulse fluences and probe-photon energies. The observed reflectivity line shape demonstrated the generation of nonequilibrium electron temperatures which cool to the lattice on a 2–3 ps time scale.

.

2.4. Bibliography

1. Mahmood, A., et al., *Band structure and bulk modulus calculations of germanium carbide.* Journal of Materials Research, 2011. **20**(05): p. 1101-1106.
2. *Renewable Energy Policy Network for the 21st Century,Renewables 2011 Global status report.* 2011: p. 116.
3. Sahnoun, M., et al., *First-principles calculations of optical properties of GeC, SnC and GeSn under hydrostatic pressure.* Physica B: Condensed Matter, 2005. **355**(1–4): p. 392-400.
4. ZHAN Chang-Yong, W.L.-W., HUANG Ning-Kang, *Effect of Bias on Content of GeC in Ge 1-x Cx Films.* Chin. Phys. Lett., 2007. **24**(3): p. 803-806.
5. Baumann, R.E.S.C.W.P.K.H. *Amorphous hydrogenated carbon germanium films for hard multilayer IR optical coatings*. in *SPIE Proceedings*. 1990.
6. Wu, X., et al., *The deposition and optical properties of Ge1−xCx thin film and infrared multilayer antireflection coatings.* Thin Solid Films, 2008. **516**(10): p. 3189-3195.
7. Lettington, A.H., C.J.H. Wort, and B.C. Monachan. *Developments And IR Applications Of GeC Thin Films*. 1989.
8. Conibeer, G., et al. *Hot carrier solar cell absorbers: materials, mechanisms and nanostructures*. 2014.
9. Liu , Z.T., et al., *Structure and Properties of germanium Carbide Films Prepared by Rf Reactive Sputtering in Ar/CH4.* J Appl Phys, 1997. **36**: p. 3625-3628.
10. R. J. Soukup, N.J.I., J. S. Schrader and V. L. Dalal *Polycrystalline GeC Thin Films Deposited Using a Unique Hollow Cathode Sputtering Technique.* . in *MRS Proceedings, 862, A20.2*. 2005.
11. Chaoquan, H., et al., *Effects of the chemical bonding on the optical and mechanical properties for germanium carbide films used as antireflection and protection coating of ZnS windows.* Journal of Physics: Condensed Matter, 2006. **18**(17): p. 4231.
12. Hu, C.Q., et al., *Effects of radio frequency power on the chemical bonding, optical and mechanical properties for radio frequency reactive sputtered germanium carbide films.* Journal of Physics D: Applied Physics, 2006. **39**(23): p. 5074.
13. Hu, C.Q., et al., *Increasing sp 3 hybridized carbon atoms in germanium carbide films by increasing the argon ion energy and germanium content.* Journal of Physics D: Applied Physics, 2010. **43**(13): p. 135103.
14. Kolodzey, J., et al., *Growth of germanium-carbon alloys on silicon substrates by molecular beam epitaxy.* Applied Physics Letters, 1995. **67**(13): p. 1865-1867.
15. Krishnamurthy, M., J.S. Drucker, and A. Challa, *Epitaxial growth and characterization of Ge1-xCx alloys on Si(100).* Journal of Applied Physics, 1995. **78**(12): p. 7070-7073.
16. Krishnamurthy, M., B.K. Yang, and W.H. Weber, *Microstructural development and optical properties of epitaxial Ge1−xCx alloys on Si(100).* Applied Physics Letters, 1996. **69**(17): p. 2572-2574.
17. Okinaka, M., et al., *Effect of lower growth temperature on C incorporation in GeC epilayers on Si(001) grown by MBE.* Physica E: Low-dimensional Systems and Nanostructures, 2003. **16**(3–4): p. 473-475.

18. Okinaka, M., et al., *MBE growth mode and C incorporation of GeC epilayers on Si(001) substrates using an arc plasma gun as a novel C source.* Journal of Crystal Growth, 2003. **249**(1–2): p. 78-86.
19. Dalal, V.L., et al. *Microcrystalline Germanium Carbide: A New, Almost Direct Gap, Thin Film Material for Photovoltaic Energy Conversion.* in *MRS Proceedings*. 2001.
20. Niu, X., J. Booher, and V.L. Dalal. *Growth and properties of nanocrystalline germanium and germanium-carbide films and devices*. in *Photovoltaic Specialists Conference, 2005. Conference Record of the Thirty-first IEEE*. 2005.
21. Leu, L.C., et al., *Comparative study of ZrN and Zr–Ge–N thin films as diffusion barriers for Cu metallization on Si.* Journal of Vacuum Science & Technology B, 2008. **26**(5): p. 1723-1727.
22. Chen, C.S., et al., *Influence of the preferred orientation and thickness of zirconium nitride films on the diffusion property in copper.* Journal of Vacuum Science and Technology B: Microelectronics and Nanometer Structures, 2004. **22**(3): p. 1075-1083.
23. Schwarz, K., et al., *Zirconium nitride: a new material for Josephson junctions.* Physical Review B, 1985. **32**(12): p. 8312-8316.
24. Lamni, R., et al., *Optical and electronic properties of magnetron sputtered ZrNx thin films.* Thin Solid Films, 2004. **447–448**(0): p. 316-321.
25. Brugnoni, C., et al., *Evaluation of the wear resistance of ZrN coatings using thin layer activation.* Surface and Coatings Technology, 1998. **100–101**: p. 23-26.
26. Lide, D.R., *CRC Handbook of Chemistry and Physics* 90th ed. 2009, Boca Raton, Florida: CRC Press.
27. YaBin, Z., et al., *Low-Temperature Growth of Highly Crystalline Superconducting ZrN Thin Film on c -GaN Layer by Pulsed Laser Deposition.* Japanese Journal of Applied Physics, 2007. **46**(11L): p. L1000.
28. Myung Bok, L., et al., *Epitaxial Growth of Highly Crystalline and Conductive Nitride Films by Pulsed Laser Deposition.* Japanese Journal of Applied Physics, 1994. **33**(11R): p. 6308.
29. Signore, M.A., et al., *Zirconium nitride films deposited in sputtering atmosphere: Optical, structural, and electrical properties.* Journal of Vacuum Science & Technology A: Vacuum, Surfaces, and Films, 2011. **29**(6): p. 061507-061507-9.
30. Mei, A.B., et al., *Physical properties of epitaxial ZrN/MgO(001) layers grown by reactive magnetron sputtering.* Journal of Vacuum Science & Technology A, 2013. **31**(6): p. -.
31. Craciun, D., et al., *The effect of deposition atmosphere on the chemical composition of TiN and ZrN thin films grown by pulsed laser deposition.* Applied Surface Science, 2013(0).
32. Signore, M.A., et al., *Investigation of the physical properties of ion assisted ZrN thin films deposited by RF magnetron sputtering.* Journal of Physics D: Applied Physics, 2010. **43**(22): p. 225401.
33. Jeng, J.S., S.H. Wang, and J.S. Chen, *Effects of substrate bias and nitrogen flow ratio on the resistivity and crystal structure of reactively sputtered ZrNx films at elevated temperature.* Journal of Vacuum Science & Technology A, 2007. **25**(4): p. 651-658.
34. Jiménez, H., E. Restrepo, and A. Devia, *Effect of the substrate temperature in ZrN coatings grown by the pulsed arc technique studied by XRD.* Surface and Coatings Technology, 2006. **201**(3–4): p. 1594-1601.
35. Wang, S.-H., C.-C. Chang, and J.S. Chen, *Effects of substrate bias and nitrogen flow ratio on the resistivity, density, stoichiometry, and crystal structure of reactively*

sputtered ZrNx thin films. Journal of Vacuum Science & Technology A, 2004. **22**(5): p. 2145-2151.

36. Liu, C.-P. and H.-G. Yang, *Deposition temperature and thickness effects on the characteristics of dc-sputtered ZrNx films.* Materials Chemistry and Physics, 2004. **86**(2–3): p. 370-374.
37. Zhou, M., et al., *Influence of sputtering conditions on microstructure and mechanical properties of ZrN films prepared by radio-frequency-reactive sputtering.* Journal of Vacuum Science & Technology A: Vacuum, Surfaces, and Films, 2003. **21**(5): p. 1791-1795.
38. Liu, C.-P. and H.-G. Yang, *Systematic study of the evolution of texture and electrical properties of ZrNx thin films by reactive DC magnetron sputtering.* Thin Solid Films, 2003. **444**(1–2): p. 111-119.
39. Del Re, M., et al., *Study of ZrN layers deposited by reactive magnetron sputtering.* Surface and Coatings Technology, 2003. **174–175**(0): p. 240-245.
40. Del Re, M., et al., *XPS study of ZrN layers deposited by reactive magnetron sputtering.* Etude par XPS de couches de ZrN déosés par pulverisation réactive magnétron, 2002. **2 4**(304): p. 347-355+240+430.
41. Barnett, S.A., et al., *Epitaxial growth of ZrN on Si(100).* Applied Physics Letters, 1988. **53**(5): p. 400-402.
42. Pilloud, D., et al., *Effect of germanium addition on the properties of reactively sputtered ZrN films.* Thin Solid Films, 2005. **492**(1–2): p. 180-186.
43. Yanagisawa, H., et al., *Epitaxial growth of (001)ZrN thin films on (001)Si by low temperature process.* Japanese Journal of Applied Physics, Part 1: Regular Papers and Short Notes and Review Papers, 2005. **44**(1 A): p. 343-349.
44. Conibeer, G.J., et al., *Slowing of carrier cooling in hot carrier solar cells.* Thin Solid Films, 2008. **516**(20): p. 6948-6953.
45. Sankey, O.F., et al., *Energetics and electronic structure of the hypothetical cubic zincblende form of GeC.* Modelling and Simulation in Materials Science and Engineering, 1993. **1**(5): p. 741.
46. Pandey, R., et al., *A theoretical study of stability, electronic, and optical properties of GeC and SnC.* Journal of Applied Physics, 2000. **88**(11): p. 6462-6466.
47. Feng, Y., et al., *Non-ideal energy selective contacts and their effect on the performance of a hot carrier solar cell with an indium nitride absorber.* Applied Physics Letters, 2012. **100**(5): p. 053502.
48. Nesting, D.C., J. Kouvetakis, and D.J. Smith, *Morphological control and structural characteristics of crystalline Ge–C systems: Carbide nanorods, quantum dots, and epitaxial heterostructures.* Applied Physics Letters, 1999. **74**(7): p. 958-960.
49. Saha, B., T.D. Sands, and U.V. Waghmare, *Electronic structure, vibrational spectrum, and thermal properties of yttrium nitride: A first-principles study.* Journal of Applied Physics, 2011. **109**(7): p. 073720.
50. Saha, B., Acharya, Jagaran,Sands, Timothy D.,Waghmare, Umesh V., *Electronic structure, phonons, and thermal properties of ScN, ZrN, and HfN: A first-principles study.* Journal of Applied Physics, 2010. **107**(3).
51. Christensen, A.N., Dietrich, O. W.,Kress, W.,Teuchert, W. D., *Phonon anomalies in transition-metal nitrides: ZrN.* Physical Review B, 1979. **19**(11): p. 5699-5703.
52. Christensen, A.N., et al., *Phonon anomalies in transition-metal nitrides: HfN.* Physical Review B, 1983. **28**(2): p. 977-981.
53. Bazhanov, D.I., et al., *Structure and electronic properties of zirconium and hafnium nitrides and oxynitrides.* Journal of Applied Physics, 2005. **97**(4): p. 044108.

54. Marini, A., R. Del Sole, and G. Onida, *First-principles calculation of the plasmon resonance and of the reflectance spectrum of silver in the GW approximation.* Physical Review B, 2002. **66**(11): p. 115101.
55. Groeneveld, R.H.M., R. Sprik, and A. Lagendijk, *Femtosecond spectroscopy of electron-electron and electron-phonon energy relaxation in Ag and Au.* Physical Review B, 1995. **51**(17): p. 11433-11445.
56. Fann, W.S., et al., *Electron thermalization in gold.* Physical Review B, 1992. **46**(20): p. 13592-13595.
57. Suárez, C., W.E. Bron, and T. Juhasz, *Dynamics and Transport of Electronic Carriers in Thin Gold Films.* Physical Review Letters, 1995. **75**(24): p. 4536-4539.
58. Sun, C.K., et al., *Femtosecond investigation of electron thermalization in gold.* Physical Review B, 1993. **48**(16): p. 12365-12368.
59. Schoenlein, R.W., et al., *Femtosecond studies of nonequilibrium electronic processes in metals.* Physical Review Letters, 1987. **58**(16): p. 1680-1683.

Chapter 3

Fabrication and characterization of deposited germanium carbide

This chapter presents the experimental work performed on germanium carbide film deposited using RF sputtering. The growth of novel nanocrystalline germanium carbide using radio frequency (RF) sputtering has been discussed and analysed for the photovoltaic application. The growth of germanium carbide film and Ge-C content are investigated with both reactive and co-sputtering method. It also focuses on how process parameter such as substrate temperatures and RF power affect the basic properties of the deposited germanium carbide films.

Introduction

Germanium-based crystalline semiconductors have been studied in detail for their immense potential in optoelectronic applications such as optical detectors [1-9]. Germanium carbide (GeC) thin films with narrow band gap (Eg<1.5 eV) is gaining considerable attention because of their remarkable structural, optical and electrical properties which make them promising candidates for applications in photovoltaics [10, 11]. Tunable bandgap (E_g) over a wide energy range is one of the particularly attractive features of this material [12-16]. Moreover, the absorption coefficient of GeC film is much higher than that of Si and Ge [17-20]. This could make it a suitable candidate for the bottom layer of tandem solar cell [9]. Band gap tuning required for the tandem cell applications can be achieved by exploiting the quantum confinement properties of the size-controlled nanocrystalline Ge_xC_{1-x} [21-23]. Other group IV alloys such as a-SiGe and a-SiC have also been widely studied for solar cell application [24, 25] . Ge-C has been widely researched for application in infrared windows [3, 5, 26-28].

Ge_xC_{1-x} is an indirect band gap semiconducting material, which crystallises in both cubic (zinc blende) and hexagonal (wurtzite) phases [29]. Although Ge_xC_{1-x} is nontoxic and contains reasonably abundant elements, it is more complex to fabricate GeC compared to SiC due to large lattice constant mismatch (37% between diamond (a_c = 3.5668 Å) and Ge (a_{Ge} = 5.668 Å)), thermodynamic instability and low solubility of carbon in Ge ($1x10^8$ cm^{-3} at the melting point of Ge) [30-32] at all temperatures and pressures. C and Ge can hardly form stable compound under thermal equilibrium conditions due to the large difference in atomic radius. Therefore, a very low crystallinity is usually achieved for the films. The low carbon content of 4-15 % in Ge_xC_{1-x} films have been considered feasible for crystallisation [33-35]. Epitaxial $Ge_{1-x}C_x$ with less than 1% carbon on Si (001) using molecular beam epitaxy has been reported by Osten et al. [1, 2]. However, Zhan et al. [6, 34] demonstrated deposition of $Ge_{1-x}C_x$ films by medium frequency magnetron reactive sputtering technique with maximum 11.6 % Ge-C content at a bias voltage of 250 V with T_s of 150 ºC. Researcher Xing-Sen Che [36-39] and Yang Ping Li [23, 40-48] have concluded that co-sputtering fabrication process is more favourable to form Ge-C bonds than reactive sputtering and studied structural and optical properties of the amorphous $Ge_{1-x}C_x$ film. Growth of GeC has been investigated using various fabrication methods such as molecular beam epitaxy (MBE) [1, 2, 49-51], reactive sputtering [3, 6, 14, 36, 38, 52-55], chemical vapour deposition (CVD) [7, 8, 10], reactive pulse laser deposition [56], and activated reactive evaporation (ARE) [9, 57].

Recently, group IV alloy materials have received research interest in advance photovoltaic concept such as the hot carrier absorber. In Chapter 2 of this thesis, comparison of the normalised phononic band gaps to the acoustic phonon energy for

different group IV compounds has been presented. GeC exhibit a very large phononic band gap which can be attributed to large mass difference between germanium atom and carbon atom. Based on the calculation of phonon dispersion relationship which indicates its potential capability of blocking optical phonons to decay as acoustic phonons known as Klemens mechanism, from which optical phonons can reheat up carriers and therefore slow the cooling rate of hot carriers [58, 59]. Therefore, it could be a prospective hot carrier absorber material. Importantly these elements are reasonably abundant to allow large-scale and cost-effective manufacturing. The optical bandgap of GeC is also in the range of 0.6 - 1.1 eV [18, 55] which is suitable for photovoltaic application as it can absorb a large fraction of the solar spectrum.

The growth of nano-crystalline Ge_xC_{1-x} (nc-Ge_xC_{1-x}) has been demonstrated (in Section 3.1) using RF magnetron co-sputtering for the first time in UNSW. The advantage of sputtering over other fabrication methods includes simplicity, the potential for high throughput and better uniformity over a large area.

In Section 3.3, properties of amorphous GeC (a-Ge_xC_{1-x}) films deposited by RF reactive sputtering are reported. Variations of Ge-C content and E_g with different substrate temperature (T_s) are investigated. The effects of the T_s on the percentage of GeC deposited are analysed in detail. The GeC percentage by volume was found to first increase and then decrease with increasing substrate temperature. Importantly, a-Ge_xC_{1-x} films with GeC content up to 21% has been fabricated with 50 W RF power at 250 ºC.

The dependence of RF powers on the composition, structure and optical properties of the a-Ge_xC_{1-x} films are reported in Section 3.4. These results are discussed from the standpoint of the structural and compositional change in the films with deposition conditions, owing to the change in the plasma reaction process including the sputtering of carbon and germanium atoms.

Experiment details

The Ge_xC_{1-x} films were grown by sputtering of single crystal Ge target using RF sputtering system (13.56 MHz). The target consisted of a 4" Ge wafer (100 mm in diameter) with 99.999 % purity. Before the film deposition, the growth chamber was pumped down to below 5 x 10^{-4} Pa using a turbo-molecular pump. Films were grown simultaneously on Si (100) and quartz substrate to facilitate various characterisation methods for structural, compositional and optical properties. Substrates were cleaned in Piranha solution and silicon substrates were dipped in hydrofluoric (HF) solution (10:1) to remove the oxide layer before they were loaded into the growth chamber. The target was pre-sputtered using Ar gas for, at least, 15 minutes prior to the film deposition to remove any surface oxides or impurities from its surface.

All the Ge_xC_{1-x} films have been deposited using the process mentioned above unless otherwise stated. X-ray diffraction (XRD), Raman spectroscopy, X-ray photoelectron spectroscopy (XPS), Dektak Profilometer, Ultra Violet visible (UV-Vis) spectrometer, Atomic force microscopy (AFM), and High resolution transmission electron microscopy (HRTEM) have been used to study the structural, compositional and optical properties of deposited Ge_xC_{1-x} films. Details of characterisation tools are given in Appendix C.

In Section 3.1, deposition of the Ge_xC_{1-x} films using co-sputtering of Ge and graphite target is presented. The coverage area of Ge on graphite target was approximately 40 %. The substrate temperatures ranging from 350 ºC to 550 ºC and RF power of 50 W were used. Ar gas pressure during the Ge_xC_{1-} film deposition was 0.1 Pa.

In Section 3.2 and 3.3, a-Ge_xC_{1-x} films were synthesised in the mixed discharge gases of Ar (99.99 % pure) and CH_4 (99.99 % pure). During the film deposition, the methane partial pressure was kept constant at 0.02 Pa with a 0.1 Pa as total gas (Ar + CH_4)

pressure. The gas flow rate of Ar and CH_4 was accurately controlled by mass flow controllers. In Section 3.2, substrate temperature was varying from room temperature (RT) to 350 ºC keeping RF power constant at 40 W and 50 W whereas, in Section 3.3 all a-Ge_xC_{1-x} films were deposited at various radio frequency (RF) powers varying from 40 W to 80 W keeping substrate temperature constant at 250 ºC.

3.1 Synthesis of nano-crystalline germanium carbide film using radio frequency magnetron sputtering

In this Section, growth of nano-crystalline GeC by co-sputtering of combined Ge and graphite target has been investigated. Deposition details of the GeC films have been already discussed in Introduction of Chapter 3.

In order to characterise the deposition uniformity and surface roughness of the as-deposited Ge_xC_{1-x} films, AFM measurements were carried out using Bruker Dimension ICON. Figure 3.1.1 shows an AFM image of the film deposited at 350 ºC with 50 W RF power on a Si (100) substrate. The film is ~ 100 nm thick. The film has a root mean square (RMS) roughness of about 4 nm, indicating uniform deposition with low surface roughness.

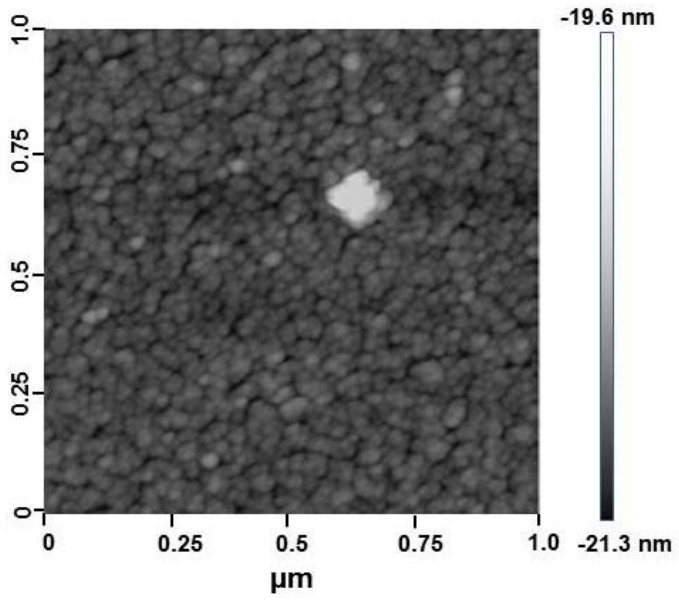

Figure 3.1.1: AFM image of a Ge_xC_{1-x} film deposited at 350 °C with 50 W RF power on a Si (100) substrate. The surface roughness is about 4 nm. Thickness of the film is ~ 100 nm.

The resitivity of the deposited GeC film was found to be ~2.3 mΩ cm using four point probe method.

Figure 3.1.2 shows HRTEM of the Ge_xC_{1-x} film. The HRTEM image shows nano-crystals in the film. From the TEM image, d-spacing of the nano-crystals has been calculated which is around 3.4 nm that gives lattice constant of 5.53 ± 0.4 Å. This is consistent with the value published by M. Todd and J. Kouvetakis for the lattice constant of GeC = 5.54 Å [60]. Amorphous SiO_2 layer of about 2.2 nm is speculated between Si substrate and Ge_xC_{1-x} film. It might be because of oxidation of substrate in the deposition chamber.

The structural properties of the crystal were analysed using a numerical model. In this model, a unit cell was assumed to be of 4 atoms, i.e., 1 C and 3 Ge, arranged in a zinc blende like crystal structure. With the help of Quantum Espresso [61], Self-consistent-field (SCF) calculations were performed on the postulated system within the framework of Density Functional Theorem (DFT). Two norm-conserving Perdew-Burke-Ernzerhof (PBE) pseudo-potentials were used in the simulation. The plane wave cut-off was set at 70 Ry and the **k**-mesh adopted in this calculation was 6x6x3. Through the equation of State, the lattice constant was estimated at 5.34 +/- 0.5 Å which matched well with our TEM measurement.

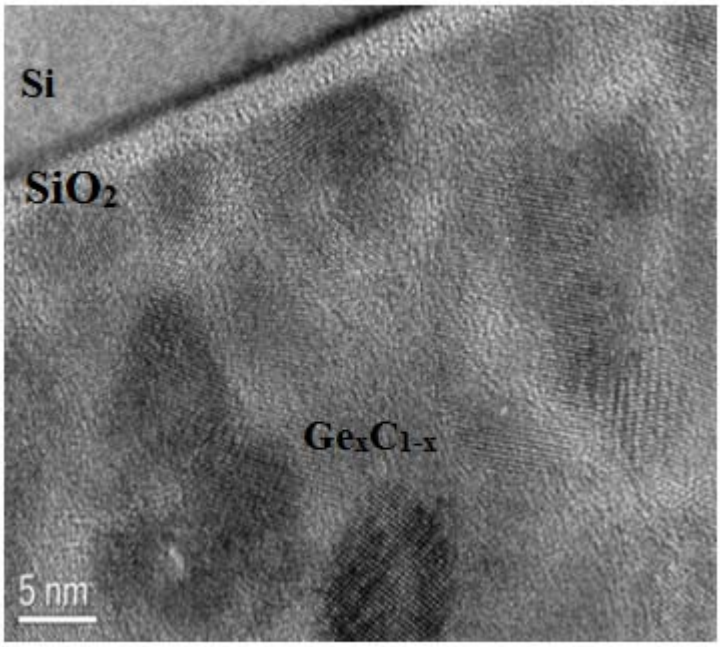

Figure 3.1.2: HRTEM image showing poly-crystalline growth of Ge_xC_{1-x} on Si. The film was deposited at 350 °C.

Effect of the substrate temperature on the composition of GeC films was investigated by XPS. Figure 3.1.3 (a) shows Ge3d and C1s XPS spectra of Ge_xC_{1-x} films grown on Si (100) at three different substrate temperatures (T_s). To avoid surface effects, the measurements were taken after Ar^+ etching for 60 s. The peak at 283.8 eV for the 350 ºC sample indicates the carbide formation whereas the peaks around 284.5 eV for the other two samples are elemental carbon peaks [4-6, 34, 52, 62]. In Figure 3.1.3 (b) Ge3d and C1s depth profiles of the sample grown at 350 ºC are shown. Atomic compositions of Ge3d, C1s and O1s at different nominal depth (ND), calculated as the product of etching rate (0.42 nm /s) and etch time (s), are shown in the inset. C and Ge are almost uniformly distributed in the bulk of the film. On the surface significant oxygen is observed which is likely to be due to the oxidation of Ge when the samples were exposed to air. Higher C content of 57.22 % on the surface can be attributed to surface contamination. From the main Figure 3.1.3 (b) it is evident that the C1s peak shifts to lower energy as we move from the surface to the depth of the film, indicating the carbide formation in the bulk of the film. Oxidation of Ge on the surface of the film deposited at 350 ºC is evidenced by the presence of GeO_y bond at 33.15 eV. As per previous literature [6, 63] GeO_y can exhibit peaks at 31.7 eV, 32.45 eV and 33.15 eV. The result clearly shows a peak at 33.15 eV indicating the formation of GeO_y bonds on the surface of the film. GeO_y bond and C1s hydrocarbon also found on the surface in the other two samples deposited at higher T_s i.e. 450 ºC and 530 ºC (not shown here).

In Figure 3.1.3, a higher C content of 57.22 % was found on the deposited GeC surface using XPS analysis due to surface contamination. Although this contamination is only monolayer thick in most of cases, a higher fraction of C is seen deeper in the film. This

is because the average analysis depth of XPS is ~10 nm. As it can be seen C content decreases with the depth and stabilises around 20 %.

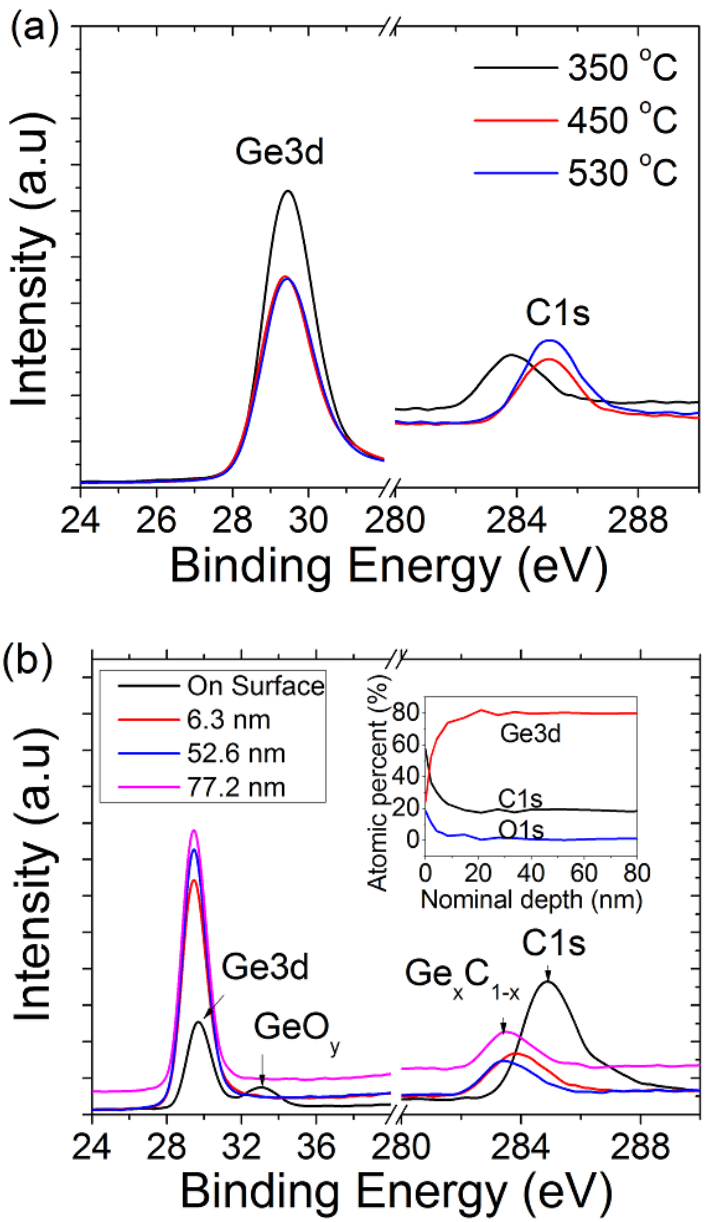

Figure 3.1.3 (a): Ge3d and C1s XPS spectra of a Ge_xC_{1-x} film grown on Si (100) at different T_s with RF = 50W.(b) Ge3d and C1s XPS spectra of the film grown at 350 °C. Inset shows atomic composition of C1s, Ge3d and O1s with nominal depth.

In order to estimate the composition of Ge-C in the film, the broad peak around 283 eV, as shown in Figure. 3.1.2 (b) has been fitted with three Gaussian components using a Levenberg-Marquardt (L-M) peak analyser algorithm keeping the peak centre and FWHM as free parameters. Figure 3.1.4 shows fits to the signal from three depths. There is a high quality of the fit with r-square (coefficient of determination) value close to 0.99. The broad peaks in Figure 3.1.4 (a) can be best fitted with two peaks at 284.8 eV and 286.2 eV. They can be attributed to elemental carbon and C-H_n (where n = 1, 2, 3) bonds [5, 6, 52, 53, 62, 64, 65]. With depth the peak shifts to lower binding energy and can be fitted with two peaks at 283.8 eV and 284.9 eV. Similarly, the peak in Figure 3.1.4 (c) can be fitted with peak at 283.6 eV. The 283.8 eV and 283.6 eV peaks in Figure 3.1.4 (b) and 3.1.4 (c), respectively, can be attributed to Ge-C bonds [6, 52-54, 62]. The other peaks at about 284.5 eV are attributed to C-C bonds in graphitic or tetrahedral form. The component at higher binding energy (BE) of 288.6 eV, attributed to C=O bond [23, 40-48, 65], is not observed. At the depth of 77.2 nm, Ge-C bond is observed with slightly lower BE of 283.6 eV. It is also to be noted that no C-C bond is observed at this depth. It can also be observed that C1s carbide peak shift to lower BE with depth at 350 ^{o}C. This might be due to charge transfer caused by electronegativity difference between carbon and germanium (Pauling electronegativities: ~2.01 for Ge and ~2.55 for carbon)[9, 66].

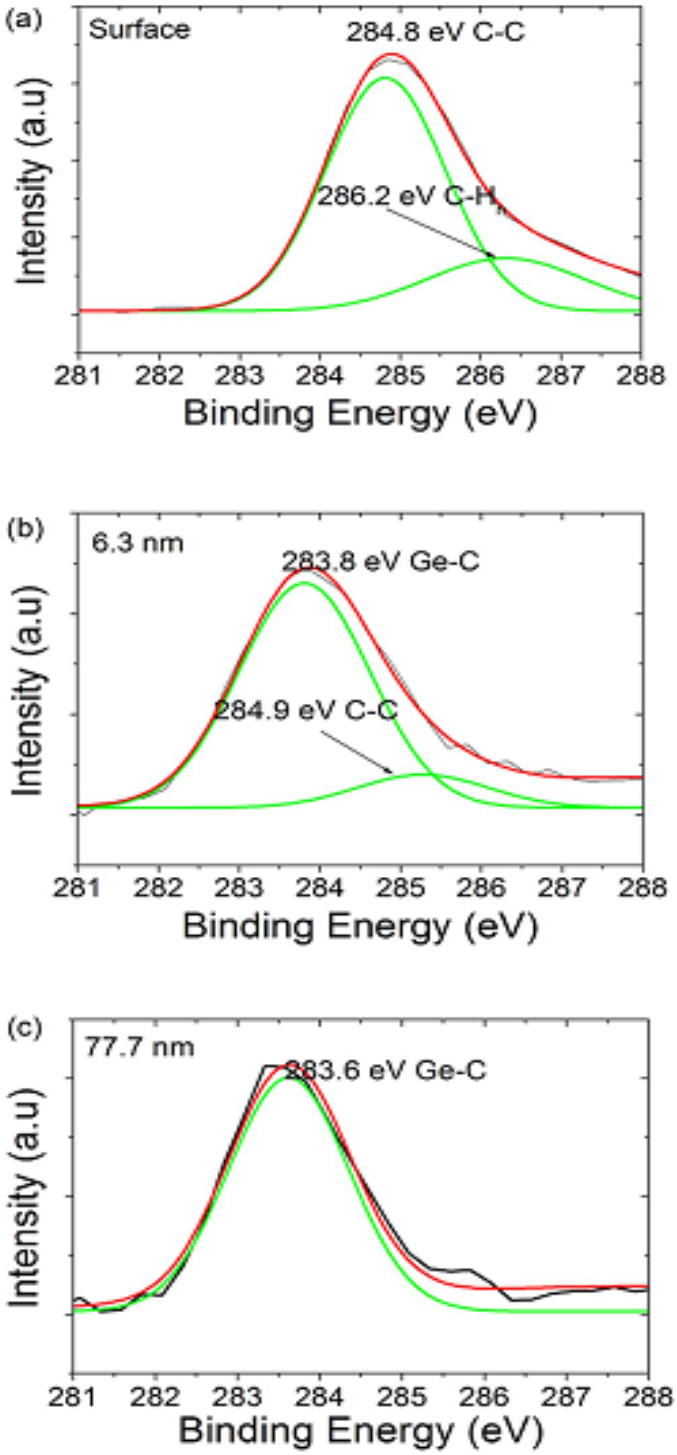

Figure 3.1.4: Fitting (red line) to the C1s spectra (black line) of the Ge_xC_{1-x} films deposited at 350 ^oC using three Gaussians (green lines) which ascribe to Ge-C and C-C bonds(a) on surface, (b) at 6.3 nm, and (c) at 77.7 nm nominal depth.

Table 3.1.1 shows the composition of the Ge_xC_{1-x} film deposited at 350 ºC calculated from XPS at different depths. Composition of other films is not shown as they do not show the formation of GeC. A Ge_xC_{1-x} percentage at a particular depth is calculated by fitting the peak around 283 eV, as discussed earlier, and using the following formula:

Ge_xC_{1-x} (%) = (GeC area integrated %) X (total C1s %)

As in the Table 3.1.1 Ge-C composition of up to 15.5 % has been observed for the sample deposited at 350 ºC. It is higher than the maximum of 11.6 % of Ge-C reported in GeC film by Zhan t al. [34] (using a medium frequency magnetron sputtering using 250 V bias at T_s = 150 ºC).

Table 3.1.1: Composition of Ge_xC_{1-x} film deposited at 350 º C measured by peak fitting of XPS spectrum on the surface and at different depths after Ar^+ etching.

Etch time(s)	Depth(nm)	Ge3d (%)	C1s (%)	O1s (%)	GeC (%) (BE eV)
0	surface	24.2	57.2	18.4	-
15	6.3	68.6	25.8	4.7	15.5(283.8 eV)
185	77.7	79.9	18.1	1.1	12.98(283.6 eV)

Figure 3.1.5 (a) shows the Raman spectra of Ge_xC_{1-x} films deposited at 350 ºC and 530 ºC. For comparison, spectrum of Ge wafer is also shown. In the frequency range between 200 and 800 cm^{-1}, the Raman spectrum of the bare Ge wafer has one first order peak (299.8 cm^{-1}) and five second order peaks (351, 475, 545, 570 and 591 cm^{-1}) [67, 68]. The sharp peak at 299.2 cm^{-1} for the films deposited at 350 ºC and 530 ºC shown

in Figure 3.1.5 (a) can be attributed to first order optical phonon contribution of the Ge–Ge stretching mode [69, 70] . This peak is shifted for the film to lower frequency compared to the bulk Ge at 299.8 cm^{-1}. This may be due to the incorporation of carbon atoms been attributed to the Ge-C [12, 33, 71]. The Ge-C peak near 530 cm^{-1} is clearly seen in peak fitting analysis by Gaussian components using a Levenberg-Marquardt (L-M) peak analyser algorithm in Figure 3.1.5 (c) [72]. For comparison, peak fitting to Ge wafer spectrum is shown in Figure 3.1.5 (b) which does not show the Ge-C peak, as expected. Ge-C bonding could not be observed in the films deposited at higher T_s which can be explained by the formation of graphitic type agglomerates of carbon at higher deposition temperature and dominating Si peak at ~520 cm^{-1} [72] . Broad peak between 1000 and 1800 cm^{-1} are observed in both films. It is a mixture of graphitic (G band) and disorder graphitic band (D band). The G band peak at about 1578 cm^{-1} is attributed to the E_{2g} optical modes of the Brillouin zone centre of the crystalline graphite, whereas the D band peak around 1345 cm^{-1} is attributed to the disorder-allowed phonon modes [4, 5]. It can be seen from Figure 3.1.5 (a) that the D and G bands of the graphite become more apparent with increasing T_s due to an increase in the carbon content.

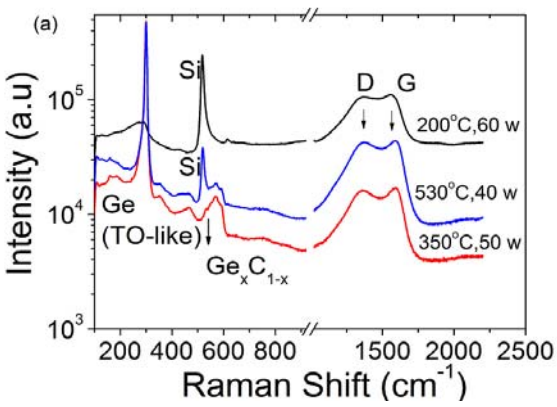

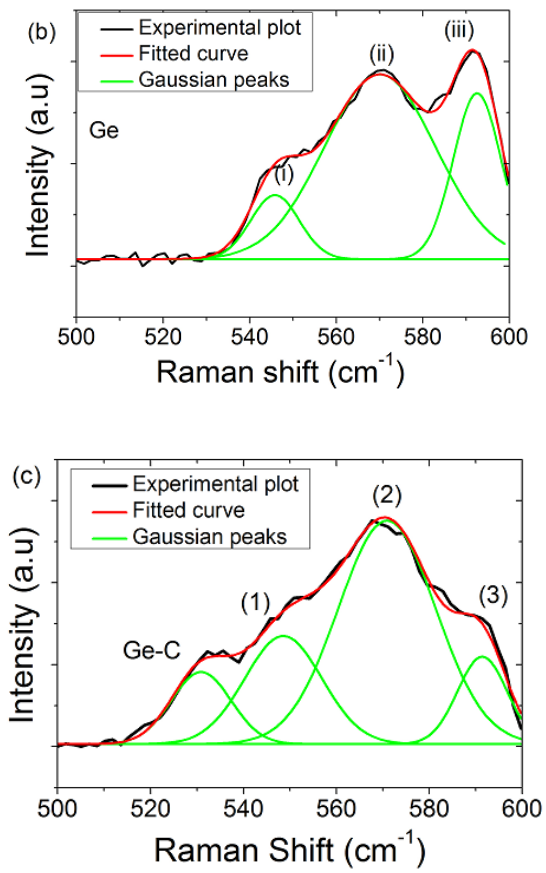

Figure 3.1.5: (a) Raman spectra of the Ge wafer and Ge_xC_{1-x}/Si (100) films deposited at different T_s with 50 W RF power. (b) peak fitting of Raman spectrum of Ge wafer using second order peaks at i) 545 cm^{-1}, ii) 570 cm^{-1}, and iii) 591 cm^{-1}. (c) Peak fitting of Ge_xC_{1-x} film grown at 350 ^oC using Ge-C peak at 530 cm^{-1} and Ge second order peaks at (1) 555 cm^{-1}, (2) 570 cm^{-1}, and (3) 591 cm^{-1}.

The optical properties of the fabricated Ge_xC_{1-x} nanocrystalline film on quartz substrate were investigated by measuring the transmittance and reflectance at RT using UV-Vis–NIR spectrophotometer with URA. The absorption coefficient was calculated from

$$\alpha = \frac{1}{t} * \ln\left(\frac{1-R}{T}\right)$$

Where, R and T are respectively the measured total reflectance and transmittance, and t is the film thickness measured with a Dektak profilometer. Optical band gap was measured from the well-known Tauc plot for indirect bandgap semiconductor [29, 36, 38, 39] according to the equation $(\alpha h\nu)^{1/2} = A(h\nu - E_g)$ where A is a constant, hν is the

photon energy and E_g is the band gap [12]. Figure 3.1.6 shows the plot of $(\alpha h\nu)^{0.5}$ as a function of photon energy ($h\nu$). By extrapolating the straight line of the $(\alpha h\nu)^{0.5}$ vs. photon energy curve to the intercept of horizontal photon energy axis, the band gap is estimated to be ~0.90eV. The estimated band gaps excess that of c-Ge of 0.67 eV at 300 K [73]. This may be recognised as alloying effect of Ge with carbon. The large value of E_g compared to Ge implies that carbon forms a bond with germanium [14, 15]. Significant low energy tail appeared at ~0 .65 eV [73] which could be due to the unalloyed Ge atoms found in the film using XPS and Raman analysis. The best linear fit to the tauc plot is shown in Figure 3.1.6. Absorption below Ge band gap ~0.5 eV energies is not fully understood.

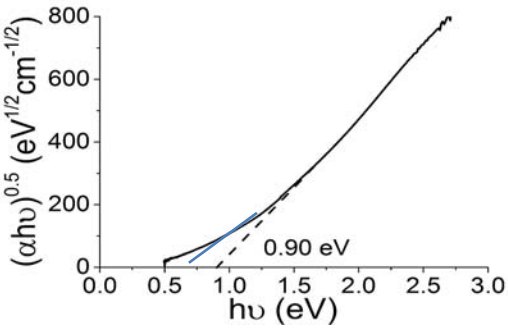

Figure 3.1.6: $(\alpha h\nu)^{0.5}$ as a function of hν for the Ge_xC_{1-x} film on quartz substrate obtained at 350 °C.

Summary

In this work, Ge_xC_{1-x} nanocrystalline films were grown on Si (100) substrates by RF magnetron co-sputtering. The sputtered Ge_xC_{1-x} film has a smooth surface with a root mean square roughness of about 4 nm. XPS results show the presence of Ge-C bonding for the samples grown at 350 ºC with 50 W indicating the carbide formation. E_g ~ 0.9 eV has been estimated for this sample from Tauc equation. TEM image shows the formation of nanocrystals with lattice constant of 5.53 Å which is consistent with GeC. The Raman signature of the local Ge–C mode is identified near 530 cm^{-1} in Ge_xC_{1-x} film grown at 350 ºC. At this growth condition, maximum of 15.5 % of Ge-C is found in the film by fitting XPS specta.

3.2 Effect of process parameters on compositional, structural and optical properties of amorphous germanium carbide films deposited by RF reactive sputtering

3.2.1 Effect of substrate temperature

In this Section, Ge_xC_{1-x} films were deposited using reactive sputtering in the mixed discharge gases of Ar (99.99 % pure) and CH_4 (99.99 % pure). During the film deposition, the methane partial pressure was kept constant at 0.02 Pa with a 0.1 Pa as total gas (Ar+CH_4) pressure. The composition of the Ge_xC_{1-x} films deposited under different conditions was characterized by XPS. Figure 3.2.1.1 shows the full-range XPS scan for Ge_xC_{1-x} film deposited at 250 ^oC with 0.02 Pa CH_4 using 50 W RF power on surface and after etching for 60 s, wherein there are three main peaks corresponding to Ge3d, C1s and O1s at 29.9 eV, 283.8 eV, and 530.6 eV, respectively. It can be seen that the O1s peak reduced after the sample was etched for 60 seconds (etch rate = 0.42 nm/s). This suggests that the oxygen impurity is mainly introduced when the sample is exposed to air rather than during the film deposition process. Similar spectra were obtained for other films deposited at the different combination of RF powers and T_s. Ge3d and C1s spectra after the etching are shown as an inset in Figure 3.2.1.1. The peak position of C1s is at 283.8 eV, which is lower than elemental C1s peak position of 284.8 eV [6, 34], is the evidence to support a carbide formation. At the same time peak position of the elemental Ge3d (29.2 eV) [34] shifts to higher binding energy to 29.9 eV which further substantiates that Ge is bonded to C [4-6, 34].

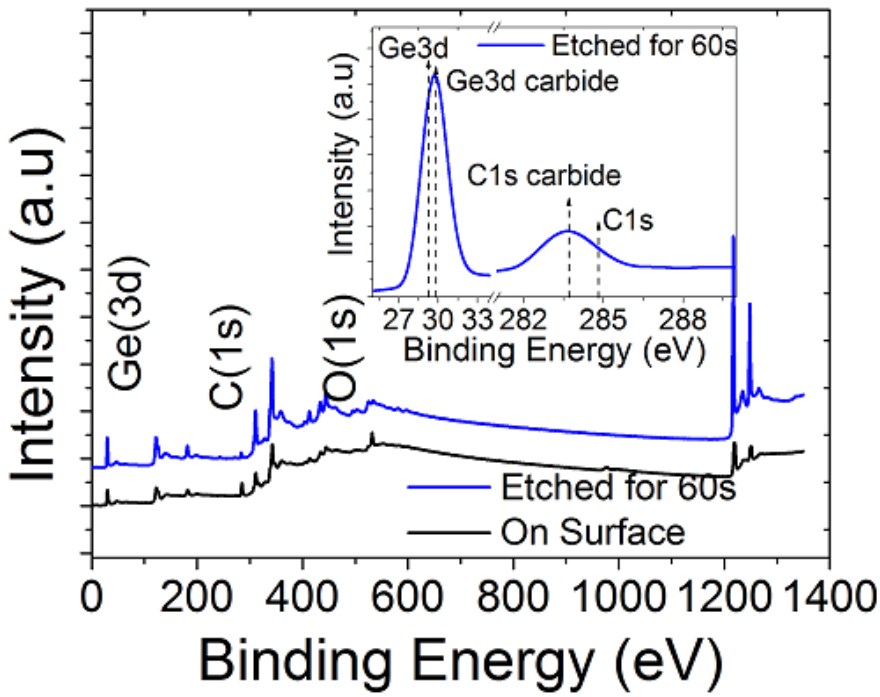

Figure 3.2.1.1: XPS spectra of a-Ge_xC_{1-x} film deposited at 250 °C using 50 W before (black) and after (blue) etching by Ar ion for 60 s. Inset shows the Ge3d and C1s spectra after etching.

Figure 3.2.1.2 shows the variation of C1s and Ge3d atomic concentration with increasing T_s for film deposited using two different RF powers. Solid lines represent the C1s and dashed line indicates the Ge3d atomic concentration whereas black and red colours indicate the films deposited at 40 W and 50 W, respectively. During the sputtering process, C species formed from the discharge of CH_4 and Ge atoms from the sputtering of Ge target which are deposited on the substrate. The gradually decreasing C content (calculated after 60 seconds Ar^+ etching) from 82 % to 20 % and 62 % to 21 % with increasing T_s from RT to 350 °C at constant RF power of 40 W and 50 W respectively shown in Figure 3.2.1.2 could be due to enhanced desorption of the methane gas from the surface of the growing film at higher T_s [4-6, 34, 37, 38, 74, 75]. As can be observed from Figure 3.2.1.2, Ge3d atomic percentage increases as the T_s is increased. On the other hand, C concentration of 26.25 % and 25.71 % observed at 40

W and 50 W respectively for the films deposited at 250 ºC. This suggests that high RF power introduces higher Ge (hence lower C content) content in the film, which is consistent with the previously published results [3, 16-19, 55, 76]. For the depositions above 250 ºC, C % is same for 40 W and 50 W.

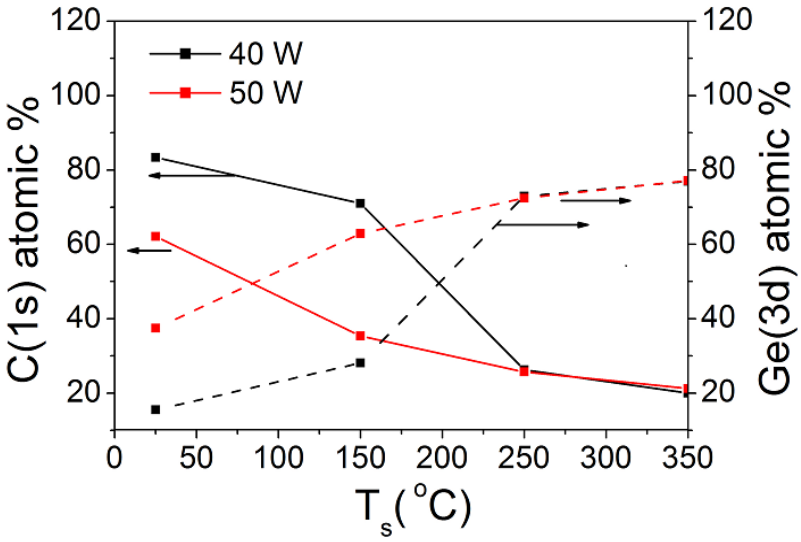

Figure 3.2.1.2: Ge3d (dashed line) and C1s (solid line) atomic concentration with T_s at two different RF powers, 40 W (black) and 50 W (red).

XPS peak fitting analysis of C1s peaks at different temperatures and RF powers was conducted, as described in Section 3.1, to characterise the composition and chemical bonding state in the films. Figure 3.2.1.3 shows fits to the C1s signals for the samples grown at various T_s and RF powers. Figure 3.2.1.3 shows the results of XPS data analysis, wherein (a) is the peak fitted C1s narrow scan on the bulk of a-Ge_xC_{1-x} film (after etching for 60 seconds), (b) is the variation of binding energy of C-C and Ge-C bonds, and (c) is the atomic % of C-C and Ge-C bonds as a function of T_s with two different RF powers. The C1s spectra were fitted by using three Gaussian components using a Levenberg-Marquardt (L-M) peak analyser algorithm keeping peak centre and FWHM as free parameters. It is evident that the quality of the fit is very good with an r-square (coefficient of determination) value close to 0.99. First, the C1s core level shifted

to low energy when T_s changes from RT to 350 ºC for both 40 W and 50 W as shown in Figure 3.2.1.3 (a), indicating that the chemical environment surrounding C atoms was significantly influenced by T_s. The peaks at 284.3 +/- 0.5 eV are assigned to C-C sites while the peaks at lower energy, 283.5 +/- 0.3 eV [77, 78] are considered to be Ge-C. The peak at 285.2 ± 0.2 eV is assigned to C-H bond [52] Interestingly, no C-C bond is found at T_s = 250 ºC,50 W .

The variation of binding energy of the Ge-C and C-C bonds deposited at different T_s , as obtained from fittings in (a), is shown in Figure. 3.2.1.3 (b). There is a gradual shifting of the peaks towards lower BE with increasing T_s. This could be because of the formation of carbide in the films. It could be observed from Figure 3.2.1.3 (b) that no Ge-C bond is formed at RT because at this temperature Ge and C exist in elemental form. The atomic percentages of the C-Ge and C-C components, are shown in Figure 3.2.1.3 (c), it could be observed that the fraction of Ge-C bonds increases with increasing T_s and tends to decrease for T_s > 250 ºC, accompanied by a decrease in the fraction of C-C bonds.

(a)

RF Power = 50 W

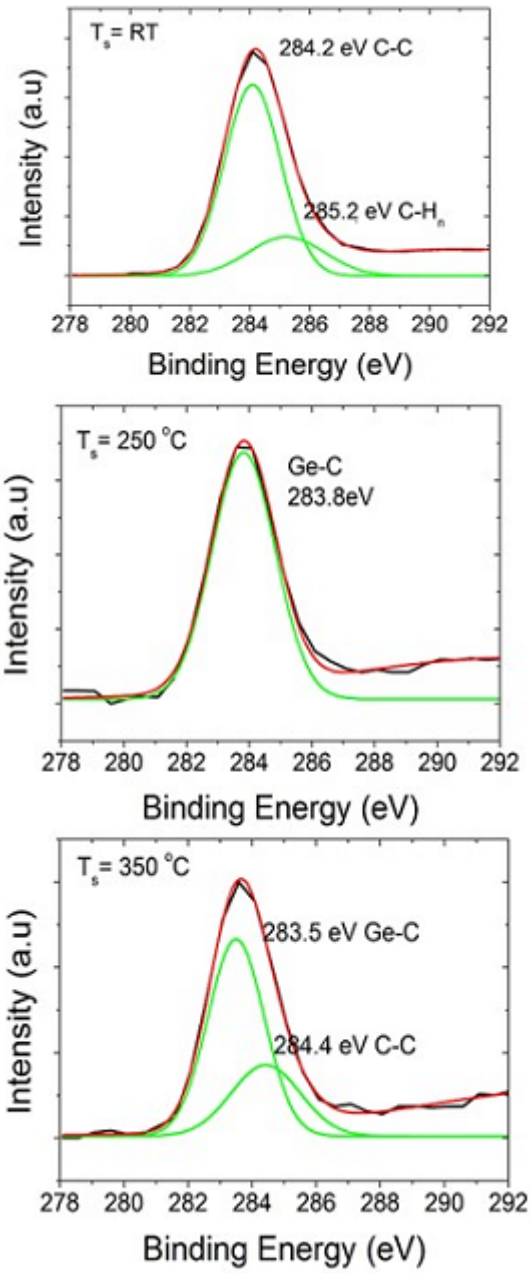

(b)

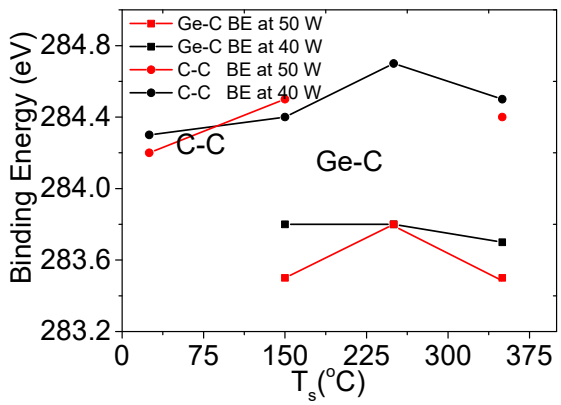

(c)

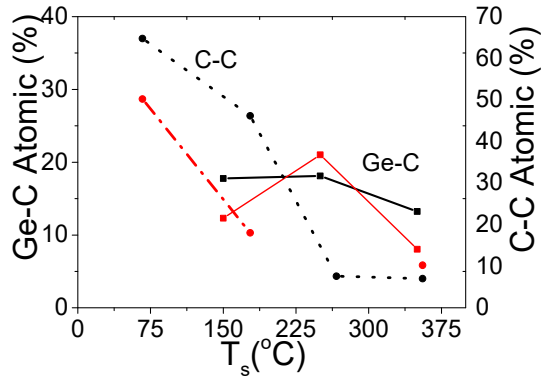

Figure 3.2.1.3: XPS peaks analysis of the Ge_xC_{1-x} films deposited at different T_s with two different RF powers 40 W (black) and 50 W (red). (a) XPS C1s spectra for Ge_xC_{1-x} films after etching for 60 s with T_s .The black line is the result from XPS, red line is the fitted spectrum, and all green spectras are de-convoluted peaks assigned to Ge-C, C-C and C-H bonds. (b) Variation of binding energy of, C-C (solid dot) and Ge-C (solid square) bonds, (c) Atomic % of C-C (solid dots and dotted lines) and Ge-C (solid squares and solid lines) bonds at 40W (black) and 50W (red).

Film thickness (t_s), deposition rate (d_R) of the films deposited at various T_s and RF powers. C and GeC content in the bulk of the film (after Ar^+ etching for 60 s) are tabulated in Table 3.2.1.1. For the films deposited with 50 W RF power, the content of Ge-C increases from 12.31 % to 21.01 % when T_s is increased from 150 ºC to 250 ºC and then it decrease to 8.05 % at 350 ºC. Similar trend is observed for the films deposited with 40 W RF power but with different Ge-C compositions. Maximum amount of Ge-C bonds seems to be formed around 250 ºC with maximum value 21% for the film deposited with 50 W RF power.

Composition of Ge_xC_{1-x} films deposited using CH_4 0.02 Pa pressure at various temperatures estimated from the peak fitting of XPS C1s spectra.is also tabulated in Table 3.2.1.1. The deposition rate (d_R) was derived from the measured film thickness (t_s) and the deposition duration (60 minutes). The deposition rate decreases from 2.7 to 2.4 nm/min and 2.8 to 2.3 nm/min with the increasing T_s at 40 W and 50 W respectively using reactive sputtering. A decrease in film thickness is observed when T_s is raised from RT to 350 °C. These effects may be attributed to an enhancement of the film compactness at elevated T_s as a consequence of increased adatom mobility, which stimulates the coalescence of nucleation islands and lowers the concentration of frozen-in defects (vacancies and voids) [79].

Table 3.2.1.1: Film thickness (t_s), deposition rate (d_R) of the films deposited at various Ts and RF powers. C and GeC content in the bulk of the film (after Ar^+ etching for 60 s) are also shown.

RF(W) / Ts(°C)	40 W				50 W			
	t_s (nm)	d_R (nm/s)	Total C1s (%)	GeC (%)	t_s (nm)	d_R (nm/s)	Total C1s (%)	GeC (%)
RT			83.4	-			62.2	-
150	166	2.7	71.1	10.5	168	2.8	35.4	12.3
250	156	2.6	26.3	18.1	150	2.5	25.7	21.0
350	144	2.4	22.1	14.1	138	2.3	21.3	8.1

The structure of the films was measured by X-ray diffraction. All samples were found to be amorphous over the entire range of T_s deposited at two different RF Powers. XRD spectra of Ge_xC_{1-x} films are shown in Figure 3.2.1.4. The diffraction pattern at RT and 150 °C are identical with a small broad peak at 55° attributed to Ge (311) [80] which indicates that the thin film that was examined was mostly amorphous with a very small amount of microcrystalline Ge. The peak at 55 ° seems to be shifted to lower diffraction angle with increasing T_s. This could be due to the introduction of carbon in the Ge matrix. Similar results were obtained for the other films grown at different T_s with 40 W

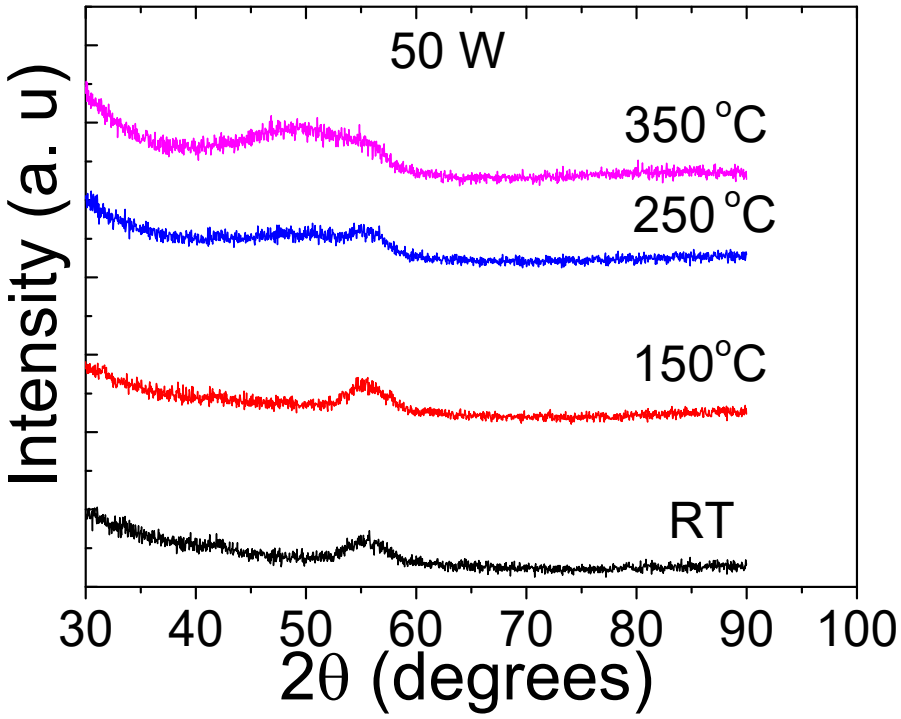

Figure 3.2.1.4: XRD spectra of the a-Ge_xC_{1-x} films at different T_s with RF power 50 W.

Figure 3.2.1.5 (a) shows the Raman spectra for the Ge_xC_{1-x} films measured in the range 200–2200 cm^{-1}. A broad peak between 1200 and 1800 cm^{-1} is observed, which have been de-convoluted into four Gaussian components after linear background subtraction using a Levenberg–Marquardt algorithm. De-convolution with two D and G Raman lines did not give accurate fit and four Gaussians were necessary to account for the observed Raman features. The four-Gaussian de-convolution results for the film deposited at three different T_s, and at 50 W RF power are shown in Figure 3.2.1.5 (b). From Figure 3.2.1.5 (a) and Figure 3.2.1.5 (b), the main peaks situated at about 1350 and 1580 cm^{-1} are identified as the D and G peak, respectively. The D band at ~1350 cm^{-1} is attributed to disorder-allowed phonon modes, which become Raman active as a result of destroying long-range order in amorphous graphitic materials while the G peak at ~ 1580 cm^{-1} is associated with the symmetric E_{2g} vibrational mode in graphite-like

materials [81]. Two additional peaks w_1 and w_2 appeared at about 1180 and 1497 cm^{-1} respectively which have been cited in literature [82-84]. The w_1 peak at the 1180 cm^{-1} peak is assigned to non-crystalline diamond which has not been observed at RT at both RF powers [83]. The appearance of Ge–Ge ~ 298 cm^{-1} and C–C (1200 ~ 1800 cm^{-1}) peaks shows that germanium, carbon and GeC clusters may be present in the a-Ge_xC_{1-x} film. The peak w_2 around 1497 cm^{-1} has been widely observed in films such as C-Si and C-Ge and are attributed to C-Ge bond [82-84]. The fitting result together with XRD spectra is indicative of the fact that amorphous GeC clusters exist in the films. In addition, the Raman peak around 298 cm^{-1} originating from Ge–Ge transverse optical (TO) mode vibration is also observed clearly [85, 86]. Intensity of this band slightly increases as T_s increases from RT to 350 ºC which can be attributed to the increase of the Ge content which has also been seen in XPS analysis as shown in Figure 3.2.1.3.

The position $w_{1(FWHM)}$, $w_{2(FWHM)}$, $w_{d(FWHM)}$, and $w_{gFWHM)}$ are four Gaussian peaks with subscripts as full width at half maximum (FWHM) after de-convolution of D and G peaks are obtained from this fitting procedure are listed in Table 3.2.1.2 and plotted in Figure 3.2.1.5 (c). Figure 3.2.1.5 (c) shows the variation of peak positions of D and G band with T_s. It can be observed that the D peak position initially decreases sharply from RT to 150 ºC and then gradually till 350 ºC. It could be due the variation in the carbon content in the film deposited. So, in combination with Figure. 3.2.1.2 (a), it can be concluded that most C atoms incorporated into the films preferred to be bonded to Ge atoms instead of forming C-C bond when the C content of the films is decreased.

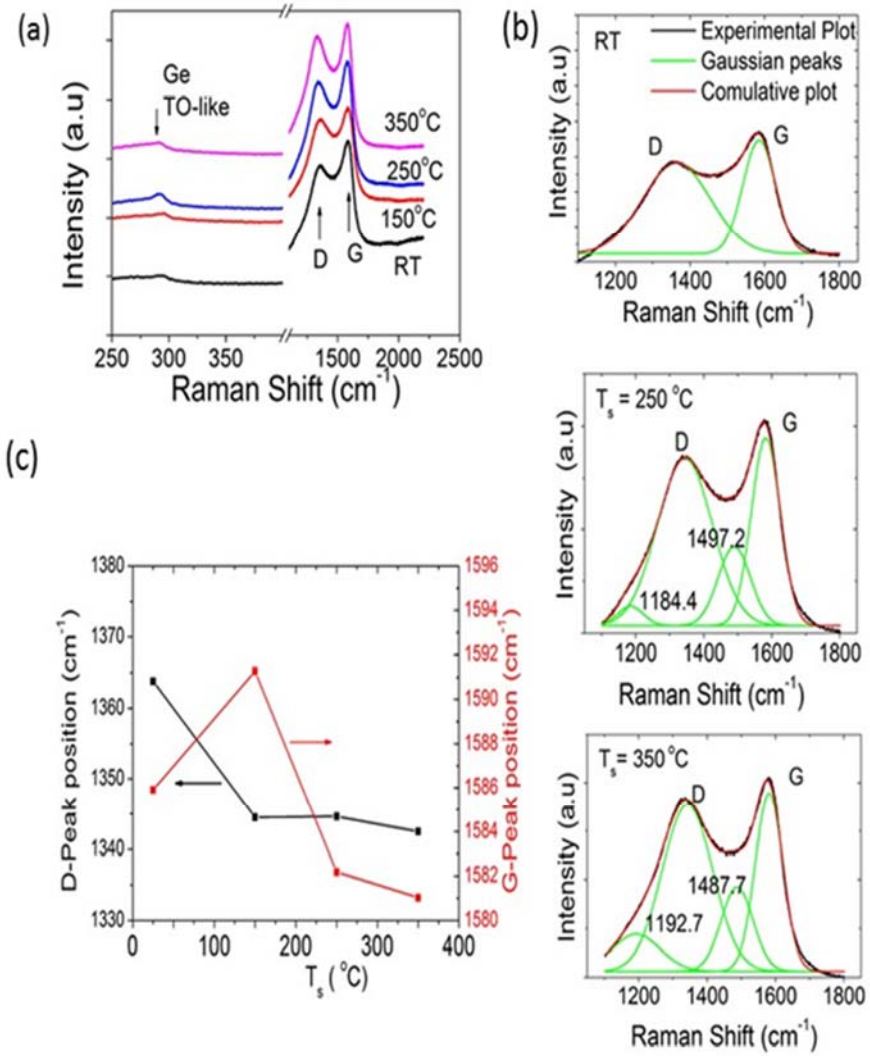

Figure 3.2.1.5: (a) Raman spectra obtained from a-Ge_xC_{1-X} films grown with different T_s using 50 W RF power. (b) Raman spectra from (a) in the range of 1100 -1800 cm^{-1}. The red curves are the experimental data and The green curves are the fitted spectra. (c) The position of the D and G peaks.

Table 3.2.1.2: Parameters of the Gaussian curves used to fit the four bands including D and G peaks of Raman spectra obtained from as deposited a-Ge_xC_{1-x} films.

P(W)	T_s (°C)	$w_{1(FWHM)(cm^{-1})}$	$w_{d(FWHM)(cm^{-1})}$	$w_{2(FWHM)(cm^{-1})}$	$w_{g(FWHM)(cm^{-1})}$
50W	RT	-	$1363.8_{(213.8)}$	-	$1585.9_{(103.4)}$
	150	$1188.6_{(99.5)}$	$1344.5_{(181.6)}$	$1509.7_{(166.3)}$	$1591.5_{(106.5)}$
	250	$1184.4_{(89.8)}$	$1344.6_{(188.8)}$	$1497.2_{(112.9)}$	$1582.2_{(100.3)}$
	350	$1182.3_{(164.6)}$	$1342.5_{(173.2)}$	$1487.7_{(109.8)}$	$1581.0_{(95.1)}$

The evolution of the optical E_g as a function of T_s, RF power and Ge-C atomic concentration can be followed in Figure 3.2.1.6 (a) and (b). The E_g have been obtained using the Tauc method for indirect bandgap semiconductor for the Ge_xC_{1-x} film [29] according to the equation $(\alpha h\nu)^{1/2} = A\ (h\nu - Eg)$, where A is constant and hν is photon energy [87]. Figures 3.2.1.7 (a) and (b) show the plot of $(\alpha h\nu)^{0.5}$ as a function of photon energy ($h\nu$). By extrapolating the straight line of the $(\alpha h\nu)^{0.5}$ vs. photon energy curve to the intercept of horizontal photon energy axis, the E_g is estimated to be in the range of 1.0 - 2.7 eV depending on the growth conditions such as T_s and RF power as shown in Figure 3.2.1.7 (a) and (b). As T_s increases from RT to 350 °C at constant RF power of 40 W and 50 W, the E_g decreases from 2.77 to 1.12 eV and 1.90 to 1.0 eV respectively. The calculated E_g exceeds that of crystalline Ge of ~0.67 eV at 300 K. Variation of E_g with Ge-C content for the Ge_xC_{1-x} films at different RF power are plotted in Figure 3.2.1.6 (b). The narrowing of the optical bandgap can be attributed to the decrease in the C concentration with rise in T_s and decrease in RF power as shown in Figure 3.2.1.6 (a) inset [14, 57]. In Figure 3.2.1.6 (a) E_g seem to correlate with T_s which could be related to amount of carbon present in the film. At higher T_s, the decrease in E_g may be related to lower carbon content in the film as shown in Table 3.2.1.1. Figure 3.2.1.6 (b)

illustrates that E_g has weak dependence on Ge-C of the film. It might be due to the small percentage of Ge-C compared to C.

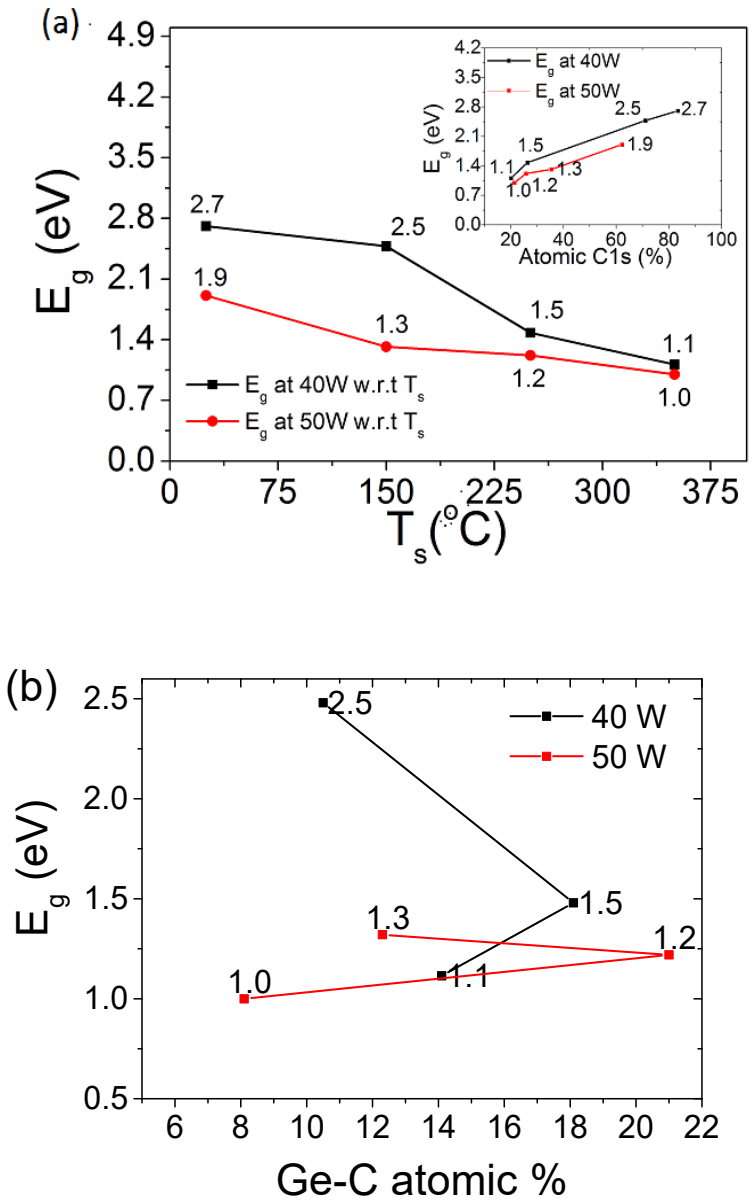

Figure 3.2.1.6: Variation of the optical band gap of the a-Ge_xC_{1-x} films deposited with two different RF powers as a function of T_s. Inset shows the change in optical band gap value w.r.t. atomic carbon concentration. (b) Change in optical band gap value w.r.t. Ge-C concentration at two different RF powers.

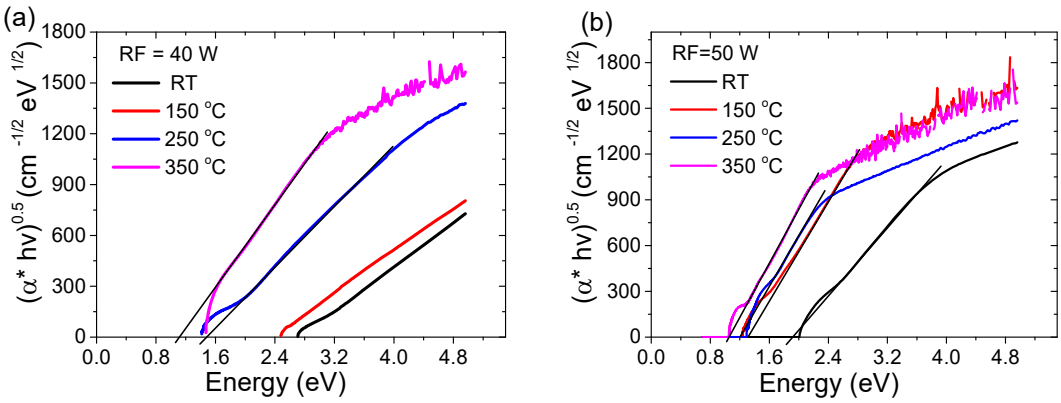

Figure 3.2.1.7 (a): Tauc plot of Ge_xC_{1-x} samples deposited at 40 W (b) 50 W.

3.2.2 Effect of RF power

In this Section, Ge_xC_{1-x} films were deposited using T_s = 250 ºC, CH_4 = 0.02 Pa using different RF Powers. The structure of the Ge_xC_{1-x} films was measured by XRD. No evidence of crystalline phases was observed except the broad peaks at 2θ ≈ 28 º and 54 º as shown in Figure 3.2.2.1.1. These peaks are attributed to Ge (111) and Ge (311) [80, 88]. At low RF powers, these peaks are not clearly visible but become marked with increasing RF power. It could be due to an increase of Ge content in the film with increasing RF powers from 40 W to 80 W as shown in Table 3.2.2.1.

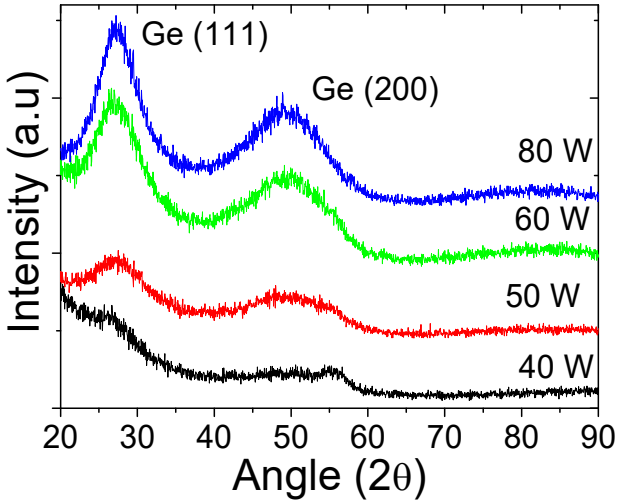

Figure 3.2.2.1: XRD spectra of a-Ge_xC_{1-x} films deposited at different RF powers with T_s = 250 °C.

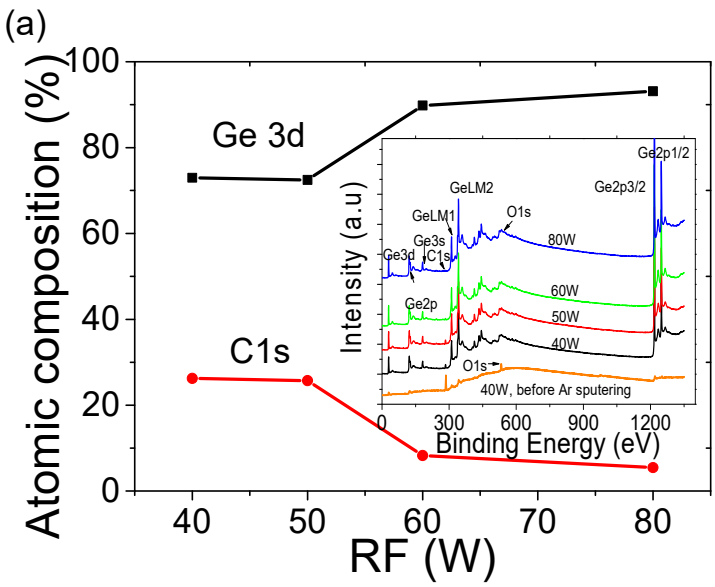

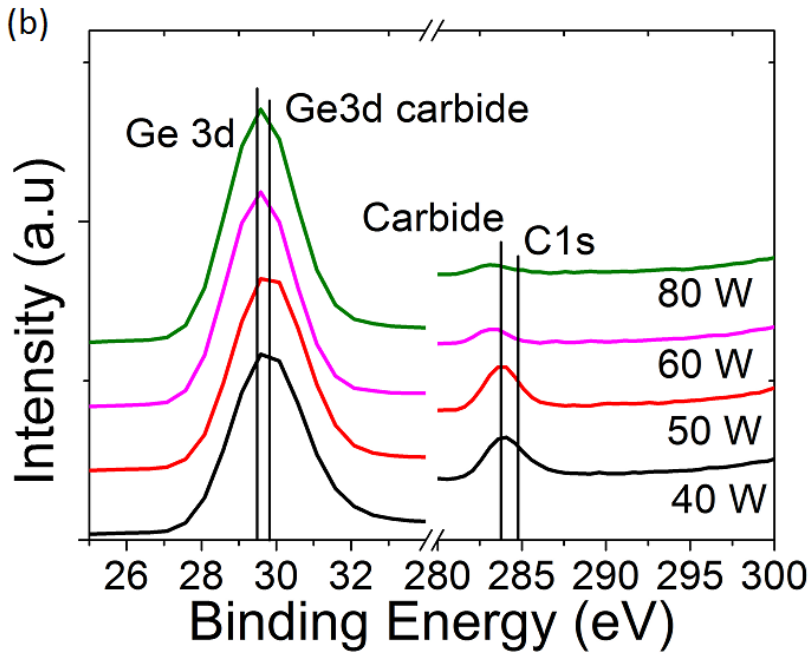

Figure 3.2.2.2: (a) main shows the C1s and Ge3d atomic composition after 60 seconds Ar^+ sputtering with different RF power, inset shows the XPS survey scan of the Ge_xC_{1-x} films deposited at different RF powers with total partial pressure of 0.12 Pa and T_s = 250 °C after Ar+ etching except survey scan of 40 W before Ar+ etching (orange). (b) Core spectra of Ge3d and C1s for the film deposited at different RF powers shows the shift in the binding energy.

XPS analysis was performed to study the atomic composition and chemical bonding in deposited GeC films in order to confirm the variation in structure and determine the changes in the optical properties of the film. XPS survey scan of the a-Ge_xC_{1-x} samples deposited at different RF powers are shown in Figure 3.2.2.2 (a) as an inset. The result for the film deposited at 40 W before etching (orange) is given as a reference. It could be observed that there are C, Ge and O atoms incorporated into the films but the intensity of the XPS peaks for O1s peak decreased to a negligible level after 60 seconds Ar^+ etching for all the films analysed at different RF powers as shown in Figure 3.2.2.2 (a) inset. So the oxygen impurity was mainly derived from surface adsorption of oxygen in the atmosphere. Hydrogen atoms cannot be distinguished by XPS due to its small

atomic number but this did not change the content of carbon and germanium in the films.

Figure 3.2.2.2 (a) main shows the atomic percentage of carbon and germanium in a-Ge_xC_{1-x} films as a function of RF powers. The carbon content tends to decrease gradually with increasing RF power from 40 W to 80 W. This is probably because the sputtering yield of germanium by argon ions increases with increasing RF power, which is due to the increase in the kinetic energy of the argon ions with increase in the RF power [12, 55, 76]. The d_R increases from 2.6 nm/s to 3.15 nm/s for RF power 40 W to 80 W respectively.

The narrow scanning XPS for Ge 3d and C1s is shown in Figure 3.2.2.2 (b). The Ge 3d peak shifted from 29.3 eV to 29.9 eV as RF decreases as shown in Figure 3.2.2.2 (b), the black line is a reference line. It has been found that the formation of Ge-C bond in the a-Ge_xC_{1-x} films can cause a upshift of Ge3d binding energy [77]. The Ge 3d curves at low RF powers, 40 W and 50 W show the peak at 29.9 eV that is associated with Ge-C bonds [77, 89] as shown in Figure 3.2.2.2 (b).

Similarly, it is clearly visible in Figure 3.2.2.2 (b) that the C1s curves were downshifted from 284.8 eV to 283.8 eV as it enters into Ge matrix [6, 34, 52, 62]. To further analyse only C1s peaks de-convoluted using a two Gaussian components with a Levenberg-Marquardt (L-M) peak analyser algorithm keeping peak centre and FWHM as free parameters. The quality of the fit is very good with an r-square (coefficient of determination) value close to 0.99. Peak position of fitted Ge-C and C-C in Ge_xC_{1-x} films deposited at different RF are shown in Figure 3.2.2.3. A significant change can be observed in Figure 3.2.2.3 as RF changed from 40 to 80 W. First, the C1s core level shifted to low energy when RF changes from 40 to 80 W, indicating that the chemical environment surrounding C atoms was significantly influenced by RF. Therefore, C1s

curve fitted into two peaks at 283.8 eV, and 284.9 eV which can be ascribed to C-Ge, and C-C bonds respectively as shown in Figure 3.2.2.3 for the film deposited at 40 W and 80 W [16,22,23]. Film deposited at 50 W shows Ge-C formation with BE at 283.8 eV.

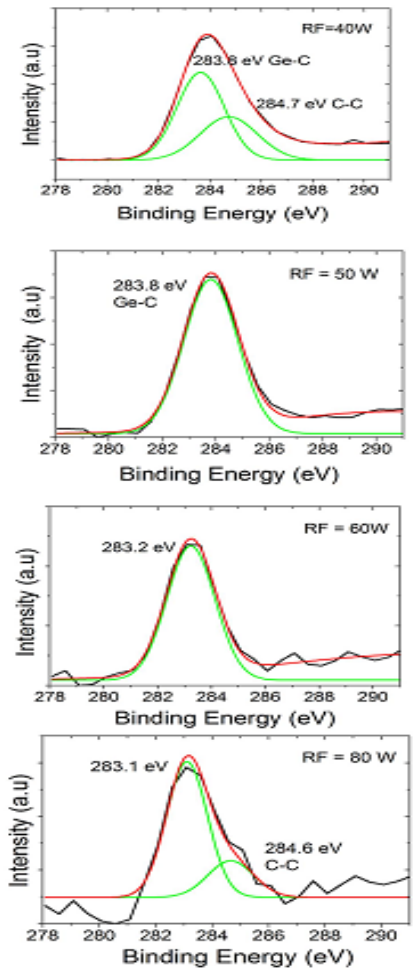

Figure 3.2.2.3: XPS peak analysis of the Ge_xC_{1-x} films deposited at different RF powers. The black line is the experimental plot, red line is the fitted spectrum, and all green spectras are de-convoluted peaks assigned to Ge-C and C-C bonds.

Film thickness (t_s), deposition rate (d_R) of the films deposited at various RF powers, Ge3d, C1s and GeC content in the bulk of the film (after Ar^+ etching for 60 s) are tabulated in Table 3.2.2.1.

Table 3.2.2.1: Thickness, d_R and C1s and GeC composition for Ge_xC_{1-x} films deposited at different RF powers.

RF(W)\T_s(ºC)	250 ºC				
	Thickness (nm)	d_R (nm/s)	Total Ge3d	Total C1s (%)	Calculated GeC (%) from C1s
40	156	2.6	72.96	26.3	18.1
50	150	2.5	72.47	25.7	21.0
60	167	2.78	89.80	8.3	5.48
80	189	3.15	93.13	5.5	3.27

The deposition rate (d_R) was derived from the measured film thickness (t_s) and the deposition duration (60 minutes). The deposition rate of Ge_xC_{1-x} films increases from 2.6 nm/min to 3.2 nm/min with increasing RF power from 40 W to 80 W respectively. Atomic compositions of GeC at different RF powers calculated as the product of area integrated under the corresponding peak and total C1s atomic concentration.

(a)

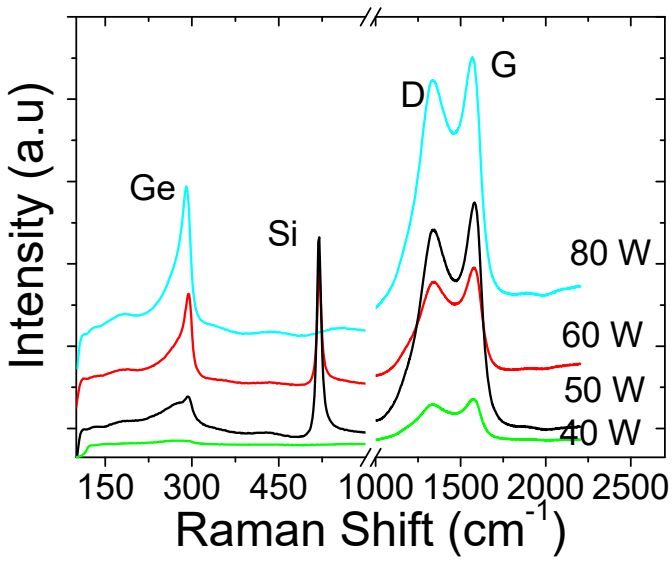

(b)

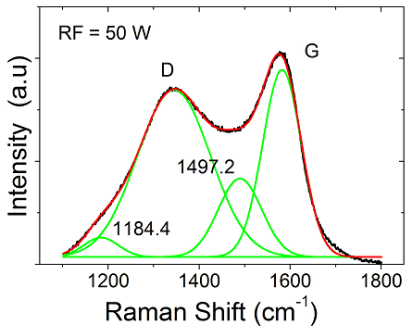

(c)

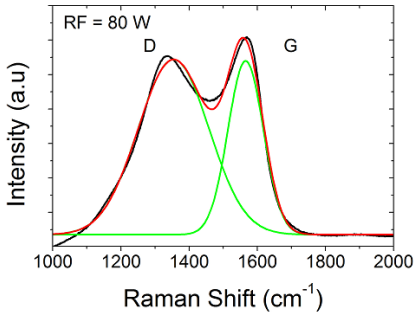

Figure 3.2.2.4: a) Raman spectra of a-Ge_xC_{1-x} films at different RF powers, b)peak fitting of Raman specta of Ge_xC_{1-x} film grown at 50 W, 250 °C, (c) .peak fitting of Raman specta of Ge_xC_{1-x} film grown at 80 W, 250 °C.

In Figure 3.2.2.4 (a) the Raman spectra of the GeC films deposited on Si (100) substrates are displayed. The shapes and positions of the Ge-related Raman modes and of the G-peak of carbon evidenced of two-phase material, i.e. GeC and a-C. The G-peak position at 1585 cm^{-1} is a signature of sp^2 bonded a-C [90]. From the spectra of the

samples deposited at 250 °C, effects on the films with increasing RF are to be noticed: i) a slight shift of the Ge–Ge longitudinal optical mode (LO) towards higher frequencies till 50 W before it starts decreasing; ii) an amorphisation of the film, judging from the increased intensities of the Ge–Ge transverse optical mode (TO) and of the D-peak with increasing carbon content, while the G-peak position does not change [90]. This is in agreement with previously published data [26] showing that increasing of GeC amount shifts the Ge–Ge LO towards higher wavenumbers. Rest of the explanation is already discussed in Section 3.2. From Figure 3.2.2.4 (c) the main peaks situated at about 1350 and 1585 cm^{-1} are identified as the D and G peak respectively. It is evidenced from XPS and Raman spectra of the film grown at 250 °C, 50 W favour the formation of maximum number of Ge-C bonds.

Summary

Ge_xC_{1-x} films have been prepared by RF reactive sputtering of a pure Ge target at various T_s using two different RF powers in a discharge of CH_4 and Ar. From XPS analysis a maximum of 21% of Ge-C content was estimated for the sample deposited at 250 ºC using 50 W. It was found that the compositional, structural, and optical properties of Ge_xC_{1-x} films can be remarkably influenced by both T_s and RF power. With increasing T_s from RT to 350 ºC, the fraction of Ge-C content first increases and then decreases above 250 ºC. This effect is significant at 50 W RF power as compared to 40 W RF power. The carbon content in the film decreases monotonically with increasing T_s from RT to 350 ºC for the process conditions used for a given T_s, C content is lower for 50 W RF power than that for 40 W RF power. Furthermore; it is found that the E_g decreases from 2.7 eV to 1.0 eV with increasing T_s from RT to 350 ºC, which can be attributed to the decrease in the C content of the Ge_xC_{1-x} films.

a-Ge_xC_{1-x} thin films were deposited by the reactive RF magnetron sputtering technique at different RF powers. The thickness of the films increases with increasing RF power. Ge-C incorporation in the films has been estimated from XPS data. Increasing RF power decreases Ge-C content in the film. This is due to reducing the carbon content in the film with increasing RF power. The maximum Ge-C content of 21% has been estimated for the films deposited at 250 ^{o}C with 50 W RF Power.

3.3 Bibliography

1. Osten, H.J., E. Bugiel, and P. Zaumseil, *Antimony-mediated growth of epitaxial Ge1−yCy layers on Si(001).* Journal of Crystal Growth, 1994. **142**(3–4): p. 322-326.
2. Osten, H.J. and J. Klatt, *In situ monitoring of strain relaxation during antimony-mediated growth of Ge and Ge1−y Cy layers on Si(001) using reflection high energy electron diffraction.* Applied Physics Letters, 1994. **65**(5): p. 630-632.
3. Chaoquan, H., et al., *Effects of the chemical bonding on the optical and mechanical properties for germanium carbide films used as antireflection and protection coating of ZnS windows.* Journal of Physics: Condensed Matter, 2006. **18**(17): p. 4231.
4. Wu, X., et al., *Mechanical and environmental properties of Ge1−xCx thin film.* Vacuum, 2008. **82**(5): p. 448-454.
5. Wu, X., et al., *The deposition and optical properties of Ge1−xCx thin film and infrared multilayer antireflection coatings.* Thin Solid Films, 2008. **516**(10): p. 3189-3195.
6. Zhan, C.Y., L.W. Wang, and N.K. Huang, *Analysis of the Ge1−xCx films deposited by MFMST.* Applied Surface Science, 2007. **253**(18): p. 7478-7482.
7. Yashiki, Y., et al., *Influence of plasma power and substrate temperature on structure of nanocrystalline germanium carbon thin films by VHF plasma CVD.* Journal of Non-Crystalline Solids, 2008. **354**(19–25): p. 2355-2358.
8. Yashiki, Y., et al., *Preparation of Microcrystalline Germanium Carbon Thin Films by Hot-Wire Chemical Vapor Deposition Using Dimethylgermane.* Jpn J Appl Phys, 2007. **46**(5): p. 2865-2868.
9. Kumar, S. and H.J. Trodahl, *Thin films of amorphous germanium-carbon and germanium-nitrogen alloys prepared by activated reactive evaporation.* Thin Solid Films, 1990. **193–194, Part 1**(0): p. 72-76.
10. Konagai, M., *Deposition of new microcrystalline materials, μc-SiC, μc-GeC by HWCVD and solar cell applications.* Thin Solid Films, 2008. **516**(5): p. 490-495.
11. Yashiki, Y., et al., *Deposition and characterization of μc-Ge1−xCx thin films grown by hot-wire chemical vapor deposition using organo-germane.* Thin Solid Films, 2006. **501**(1–2): p. 202-205.
12. Zoita, C.N., et al., *Influence of process parameters on structure and optical properties of GeC thin films deposited by RF magnetron sputtering.* Thin Solid Films, 2011. **519**(12): p. 4101-4104.
13. Herrold, J.T. and V.L. Dalal, *Growth and properties of microcrystalline germanium–carbide alloys grown using electron cyclotron resonance plasma processing.* Journal of Non-Crystalline Solids, 2000. **270**(1–3): p. 255-259.
14. Shinar, J., et al., *An IR, optical, and electron-spin-resonance study of as-deposited and annealed a-Ge1−xCx:H prepared by rf sputtering in Ar/H2/C3H8.* Journal of Applied Physics, 1987. **62**(3): p. 808-812.
15. Kumru, M., *A comparison of the optical, IR, electron spin resonance and conductivity properties of a-Ge1−xCx:H with a-Ge:H and a-Ge thin films prepared by r.f. sputtering.* Thin Solid Films, 1991. **198**(1–2): p. 75-84.
16. Saito, N., et al., *Influence of deposition conditions on the properties of a-GeC:H and a-Ge:H films prepared by r.f. magnetron sputtering.* Thin Solid Films, 1995. **269**(1–2): p. 69-74.
17. Huguenin-Love, J.L., et al. *The Properties of Ge-C Thin Films Deposited using Dual Hollow Cathodes*. in *Photovoltaic Energy Conversion, Conference Record of the 2006 IEEE 4th World Conference on*. 2006.
18. Huguenin-Love, J.L., et al., *Optical and crystallographic analysis of thin films of GeC deposited using a unique hollow cathode sputtering technique.* Materials Science in Semiconductor Processing, 2006. **9**(4–5): p. 759-763.

19. Schrader, J.S., et al., *Thin films of GeC deposited using a unique hollow cathode sputtering technique.* Solar Energy Materials and Solar Cells, 2006. **90**(15): p. 2338-2345.
20. Soukup, R.J., et al., *Experimental studies of Ge1−xCx and Ge1−x−yCxAly thin films.* Journal of Vacuum Science & Technology A, 2008. **26**(1): p. 17-22.
21. König, D., et al., *Hot carrier solar cells: Principles, materials and design.* Physica E: Low-dimensional Systems and Nanostructures, 2010. **42**(10): p. 2862-2866.
22. Shrestha, S.K., P. Aliberti, and G.J. Conibeer, *Energy selective contacts for hot carrier solar cells.* Solar Energy Materials and Solar Cells, 2010. **94**(9): p. 1546-1550.
23. Xia, H., et al., *Numerical calculation of optical phonon decay rate in InN/GaN MQW.* IOP Conference Series: Materials Science and Engineering, 2014. **68**(1): p. 012009.
24. Serenyi, M., et al., *Fabrication of a-SiGe structure by rf sputtering for solar cell purposes.* physica status solidi (c), 2003. **0**(3): p. 857-861.
25. Künle, M., et al., *Si-rich a-SiC:H thin films: Structural and optical transformations during thermal annealing.* Thin Solid Films, 2010. **519**(1): p. 151-157.
26. Hu, C.Q., et al., *Annealing effects on the bonding structures, optical and mechanical properties for radio frequency reactive sputtered germanium carbide films.* Applied Surface Science, 2009. **255**(6): p. 3552-3557.
27. Lettington, A.H., C.J.H. Wort, and B.C. Monachan. *Developments And IR Applications Of GeC Thin Films*. 1989.
28. Baumann, R.E.S.C.W.P.K.H. *Amorphous hydrogenated carbon germanium films for hard multilayer IR optical coatings*. in *SPIE Proceedings*. 1990.
29. Mahmood, A., et al., *Band structure and bulk modulus calculations of germanium carbide.* Journal of Materials Research, 2011. **20**(05): p. 1101-1106.
30. Scace, R.I. and G.A. Slack, *Solubility of Carbon in Silicon and Germanium.* The Journal of Chemical Physics, 1959. **30**(6): p. 1551-1555.
31. Sekkal, W. and A. Zaoui, *Predictive study of thermodynamic properties of GeC.* New Journal of Physics, 2002. **4**(1): p. 9.
32. Chroneos, A., *Stability of impurity–vacancy pairs in germanium carbide.* Journal of Materials Science: Materials in Electronics, 2008. **19**(1): p. 25-28.
33. Okinaka, M., et al., *MBE growth mode and C incorporation of GeC epilayers on Si(001) substrates using an arc plasma gun as a novel C source.* Journal of Crystal Growth, 2003. **249**(1–2): p. 78-86.
34. ZHAN Chang-Yong, W.L.-W., HUANG Ning-Kang, *Effect of Bias on Content of GeC in Ge 1-x Cx Films.* Chin. Phys. Lett., 2007. **24**(3): p. 803-806.
35. Gupta, N., et al., *Synthesis of nano-crystalline germanium carbide using radio frequency magnetron sputtering.* Thin Solid Films, 2015. **592, Part A**: p. 162-166.
36. Che, X.-S., et al., *Comparative study of optical properties of germanium carbon films deposited by reactive sputtering and co-sputtering.* Journal of Non-Crystalline Solids, 2013. **363**(0): p. 46-49.
37. Craciun, D., et al., *The effect of deposition atmosphere on the chemical composition of TiN and ZrN thin films grown by pulsed laser deposition.* Applied Surface Science, 2013(0).
38. Han, J., C. Jiang, and J. Zhu, *Non-hydrogenated amorphous germanium carbide with adjustable microstructure and properties: a potential anti-reflection and protective coating for infrared windows.* Surface and Interface Analysis, 2013. **45**(3): p. 685-690.
39. Todd, M., J. Kouvetakis, and D.J. Smith, *Synthesis and characterization of heteroepitaxial diamond;structured Ge1-xCx(x=1.5-5.0%) alloys using chemical vapor deposition.* Applied Physics Letters, 1996. **68**(17): p. 2407-2409.
40. Bertoti, I., et al., *Surface chemical changes in PVD TiN layers induced by ion bombardment.* Surface and Interface Analysis, 1994. **21**(6-7): p. 467-473.
41. Chung, S., et al., *Hafnium nitride for hot carrier solar cells.* Solar Energy Materials and Solar Cells, 2014(0).

42. Chung, S., et al., *Evidence for a large phononic band gap leading to slow hot carrier thermalisation.* IOP Conference Series: Materials Science and Engineering, 2014. **68**(1): p. 012002.
43. Conibeer, G., et al., *Hot carrier solar cell absorber prerequisites and candidate material systems.* Solar Energy Materials and Solar Cells, 2014(0).
44. Conibeer, G., et al. *Hot carrier solar cell absorbers: materials, mechanisms and nanostructures*. 2014.
45. Kim, B.-S., et al., *Metastable Ge1–xCx Alloy Nanowires.* ACS Applied Materials & Interfaces, 2011. **4**(2): p. 805-810.
46. Klumdoung, P., et al., *Variation of color in Zirconium nitride thin films prepared at high Ar flow rates with reactive dc magnetron sputtering.* Procedia Engineering, 2012. **32**(0): p. 916-921.
47. Konovalov, I., V. Emelianov, and R. Linke, *Hot carrier solar cell with semi infinite energy filtering.* Solar Energy, 2015. **111**(0): p. 1-9.
48. Shrestha, S., et al. *Evaluation of hafnium nitride and zirconium nitride as Hot Carrier absorber*. in *Photovoltaic Specialist Conference (PVSC), 2014 IEEE 40th*. 2014.
49. Kolodzey, J., et al., *Optical and electronic properties of SiGeC alloys grown on Si substrates.* Journal of Crystal Growth, 1995. **157**(1–4): p. 386-391.
50. Kolodzey, J., et al., *Growth of germanium-carbon alloys on silicon substrates by molecular beam epitaxy.* Applied Physics Letters, 1995. **67**(13): p. 1865-1867.
51. Krishnamurthy, M., J.S. Drucker, and A. Challa, *Epitaxial growth and characterization of Ge1−xCx alloys on Si(100).* Journal of Applied Physics, 1995. **78**(12): p. 7070-7073.
52. Vilcarromero, J. and F.C. Marques, *XPS study of the chemical bonding in hydrogenated amorphous germanium–carbon alloys.* Applied Physics A, 2000. **70**(5): p. 581-585.
53. Li, Y.-P., et al., *Optical and structural properties of co-sputtered Ge1-xCx thin films as a function of the substrate temperature.* Thin Solid Films, 2014. **551**(0): p. 74-78.
54. Jiang, C., et al., *The surface topography, structural and mechanical properties of Ge1−xCx films prepared by magnetron co-sputtering.* Journal of Non-Crystalline Solids, 2014. **383**(0): p. 126-130.
55. Hu, C.Q., et al., *Effects of radio frequency power on the chemical bonding, optical and mechanical properties for radio frequency reactive sputtered germanium carbide films.* Journal of Physics D: Applied Physics, 2006. **39**(23): p. 5074.
56. H.Z. Shafi, A.M., Z. Ali, M. Mehmood, *Optical and Structural Analysis of GeC Thin Films Deposited by Reactive Pulsed Laser Ablation Technique* Key Engineering Materials, 2010: p. 178-186.
57. Kumar, S., S.C. Kashyap, and K.L. Chopra, *Structure and transport properties of amorphous Ge1−xCx:H thin films obtained by activated reactive evaporation.* Journal of Non-Crystalline Solids, 1988. **101**(2–3): p. 287-290.
58. Conibeer, G., et al. *Hot Carrier solar cell absorbers: Superstructures, materials and mechanisms for slowed carrier cooling*. in *Photovoltaic Specialists Conference (PVSC), 2012 38th IEEE*. 2012.
59. Shrestha, S., et al. *Growth and characterization of germanium carbide films for hot carrier solar cell absorber*. in *Photovoltaic Specialists Conference (PVSC), 2012 38th IEEE*. 2012.
60. Todd, M., J. Kouvetakis, and D.J. Smith, *Synthesis and characterization of heteroepitaxial diamond-structured Ge1−xCx (x=1.5–5.0%) alloys using chemical vapor deposition.* Applied Physics Letters, 1996. **68**(17): p. 2407-2409.
61. Paolo, G., et al., *QUANTUM ESPRESSO: a modular and open-source software project for quantum simulations of materials.* Journal of Physics: Condensed Matter, 2009. **21**(39): p. 395502.
62. Hernández, M.P., et al., *Growth and characterization of polycrystalline Ge1−xCx by reactive pulsed laser deposition.* Applied Surface Science, 2011. **257**(11): p. 5007-5011.

63. Prabhakaran, K. and T. Ogino, *Oxidation of Ge(100) and Ge(111) surfaces: an UPS and XPS study.* Surface Science, 1995. **325**(3): p. 263-271.
64. W.S. J.F. Moulder, P.S., K. Bomben, *Handbook of X-ray Photoelectron Spectroscopy*. 1992, Perkin Elmer Corporation
65. Christensen, A.N., Dietrich, O. W.,Kress, W.,Teuchert, W. D., *Phonon anomalies in transition-metal nitrides: ZrN.* Physical Review B, 1979. **19**(11): p. 5699-5703.
66. Allred, A.L., *Electronegativity values from thermochemical data.* Journal of Inorganic and Nuclear Chemistry, 1961. **17**(3–4): p. 215-221.
67. Sasaki, Y. and C. Horie, *Second-order Raman scattering of small Ge particles in resonance with the E1 and E1+Delta1 edges.* Physical Review B, 1993. **48**(3): p. 2009-2011.
68. Weinstein, B.A. and M. Cardona, *Second-Order Raman Spectrum of Germanium.* Physical Review B, 1973. **7**(6): p. 2545-2551.
69. Pei, L.Z., et al., *Low temperature growth of single crystalline germanium nanowires.* Materials Research Bulletin, 2010. **45**(2): p. 153-158.
70. Jalilian, R., et al., *Phonon confinement and laser heating effects in Germanium nanowires.* Physical Review B, 2006. **74**(15): p. 155421.
71. Okinaka, M., et al., *Effect of lower growth temperature on C incorporation in GeC epilayers on Si(001) grown by MBE.* Physica E: Low-dimensional Systems and Nanostructures, 2003. **16**(3–4): p. 473-475.
72. Weber, W.H., B.K. Yang, and M. Krishnamurthy, *The Ge-C local mode in epitaxial GeC and Ge-rich GeSiC alloys.* Applied Physics Letters, 1998. **73**(5): p. 626-628.
73. Kittel, C., *Introduction to solid state physics*. 6 ed. 1986, New York: John Wiley.
74. Mei, A.B., et al., *Physical properties of epitaxial ZrN/MgO(001) layers grown by reactive magnetron sputtering.* Journal of Vacuum Science & Technology A, 2013. **31**(6): p. -.
75. Smyth, T., et al. *Hot carrier solar cells from group III-V quantum well structures*. in *Photovoltaic Specialists Conference (PVSC), 2013 IEEE 39th*. 2013.
76. Saito, N., T. Yamaguchi, and I. Nakaaki, *Comparative study of properties between a-GeC:H and a-SiC:H films prepared by radio-frequency reactive sputtering in methane.* Journal of Applied Physics, 1995. **78**(6): p. 3949-3954.
77. Vilcarromero, J., F.C. Marques, and J. Andreu, *Bonding properties of rf-co-sputtering amorphous Ge–C films studied by X-ray photoelectron and Raman spectroscopies.* Journal of Non-Crystalline Solids, 1998. **227–230, Part 1**(0): p. 427-431.
78. Vilcarromero, J., F.C. Marques, and F.L. Freire, *Optoelectronic and structural properties of a-Ge1−xCx:H prepared by rf reactive cosputtering.* Journal of Applied Physics, 1998. **84**(1): p. 174-180.
79. Saleh, R., L. Munisa, and W. Beyer, *Infrared absorption in a-SiC:H alloy prepared by d.c. sputtering.* Thin Solid Films, 2003. **426**(1–2): p. 117-123.
80. Saito, N., et al., *Amorphous and microcrystalline GeC:H films prepared by magnetron sputtering.* physica status solidi (a), 2009. **206**(2): p. 238-242.
81. Tuinstra, F. and J.L. Koenig, *Raman Spectrum of Graphite.* The Journal of Chemical Physics, 1970. **53**(3): p. 1126-1130.
82. Losurdo, M., et al., *Structural and optical investigation of plasma deposited silicon carbon alloys: Insights on Si-C bond configuration using spectroscopic ellipsometry.* Journal of Applied Physics, 2005. **97**(10): p. 103504.
83. Hong, J., A. Goullet, and G. Turban, *Ellipsometry and Raman study on hydrogenated amorphous carbon (a-C:H) films deposited in a dual ECR-r.f. plasma.* Thin Solid Films, 1999. **352**(1–2): p. 41-48.
84. Long, N.J. and H.J. Trodahl, *Structure of amorphous carbon in amorphous C/Ge multilayers.* Journal of Applied Physics, 1990. **67**(4): p. 1753-1756.

85. Minoru Kumeda, Akio Masuda, and Tatsuo Shimizu, *Structural Studies on Hydrogenated Amorphous Germanium-Carbon Films Prepared by RF Sputtering.* Japanese Journal of Applied Physics, 1998. **37**(4R): p. 1754.
86. Mariotto, G., et al., *Raman spectroscopy and scanning electron microscopy investigation of annealed amorphous carbon–germanium films deposited by d.c. magnetron sputtering.* Diamond and Related Materials, 1999. **8**(2–5): p. 668-672.
87. Tauc, J., *Optical properties and electronic structure of amorphous Ge and Si.* Materials Research Bulletin, 1968. **3**(1): p. 37-46.
88. Audoit, G., et al., *Size dependent thermal properties of embedded crystalline germanium nanowires.* Journal of Materials Chemistry, 2007. **17**(16): p. 1608-1613.
89. Jiang, C.Z., et al., *Chemical bonding and optical properties of germanium–carbon alloy films prepared by magnetron co-sputtering as a function of substrate temperature.* Journal of Non-Crystalline Solids, 2011. **357**(24): p. 3952-3956.
90. Ferrari, A.C. and J. Robertson, *Interpretation of Raman spectra of disordered and amorphous carbon.* Physical Review B, 2000. **61**(20): p. 14095-14107.

Chapter 4

Synthesis and characterization of deposited zirconium nitride

This chapter provides an overview of the experimental work performed on zirconium nitride (ZrN) film deposited using radio frequency and direct current sputtering. The structural, compositional and optical properties of as-deposited and annealed films are explored. XRD, XPS, AFM, HR-TEM, Raman and UV-Vis spectra were used to the study the above-mentioned properties. The growth of polycrystalline ZrN_x using RF reactive sputtering and single crystalline cubic ZrN using DC sputtering is reported.

Introduction

Zirconium nitride (ZrN) is a transition metal nitride known for its high hardness, thermal conductivity, high melting point and mechanical strength. There is a large mass difference between the constituent atoms which are arranged in a simple cubic rock salt structure and is expected to have a wide phonon gap. Calculated phonon bands of ZrN show a wide phonon gap [1] as shown in Figure 4.1 (a). Theoretical phonon bands have been supported experimentally by neutron scattering of ZrN powdered samples [2]. Therefore, it has a potential to exhibit slow carrier cooling due to its phononic properties. Electronic properties of ZrN indicate their metallic nature as shown by theoretical investigations and in Figure 4.1 (b) from Saha et al. [1]. Energy selective contacts (ESC) in hot carrier solar cells (HC-SCs) collect carriers at a higher energy level above the electronic bandgap, therefore, it may be possible to design a HC-SC using an absorber with no electronic band gap if the ESCs are able to extract carriers at

elevated energies and the hot carriers are maintained at high temperature in the absorber for a long time to be extracted. Materials having long hot carrier lifetime could also be used in technologies such as thermoelectric, plasmonic and thermionic emission waves [3, 4].

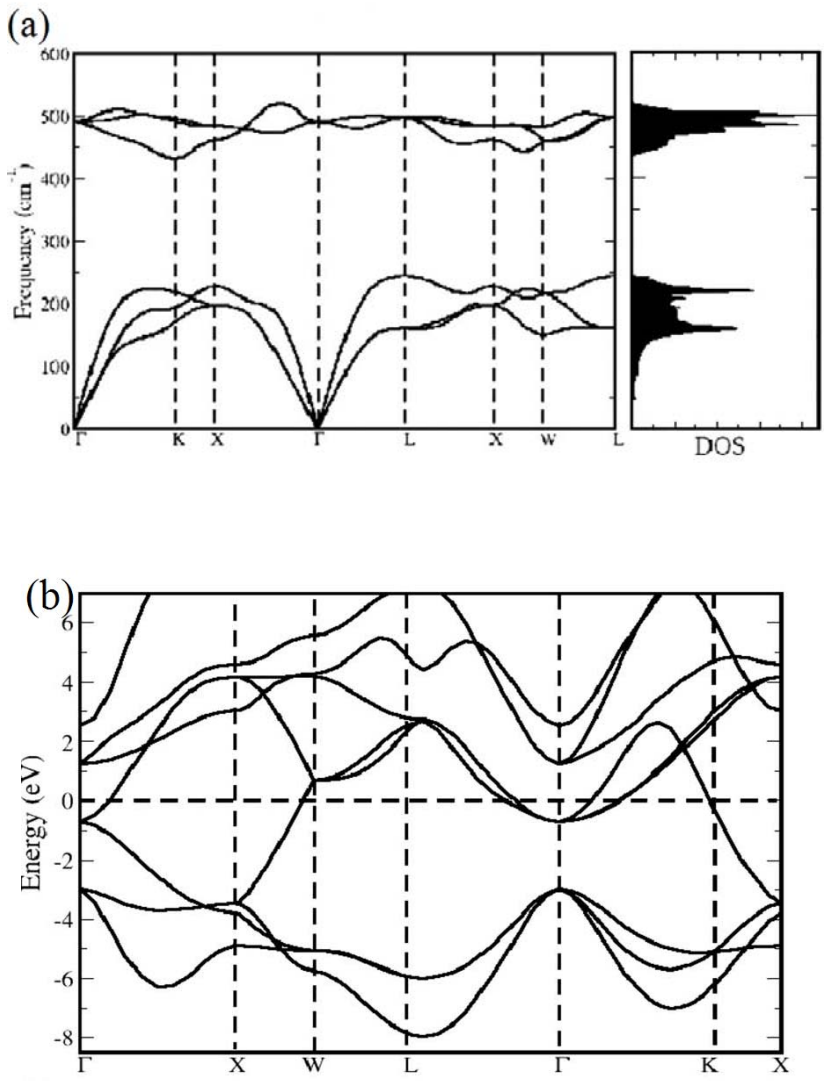

Figure 4.1: First-principles calculations of (a) phonon dispersion of zirconium nitride and (b) electronic structure. The large gap between the acoustic and optical phonon dispersion curves is evident. Reproduced from Saha et al. [1].

As discussed in Chapter 1, ZrN would require a carrier thermalisation time of the order of 1 ns or few 100 ps to be suitable as a HC-SC absorber[5, 6]. Moreover, cubic ZrN does not have an electronic bandgap, thus it would require to be operated under highly concentrated irradiation for its efficiency to be comparable with existing multi-junction cells [6-8] .While ZrN is metallic, higher nitrides of ZrN have been shown to be semiconducting or insulating. The electronic band gap of the cubic phase Zr_3N_4 is predicted to be between 0.82 and 1.1eV [9, 10]. Among transition metal nitride, zirconium nitride (ZrN) films are the most attractive candidate for various applications because they have the highest heat of formation and the lowest resistivity 13.6 μΩ cm [11-15]. It has been generally believed that to obtain epitaxial ZrN films on Si substrate, a relatively high substrate temperature of approximately 600 - 900 ºC is required [16, 17], which is too high for practical use in the microelectronics or semiconductor industry. In addition, cracks were observed in ZrN films prepared at high substrate temperature because the lattice mismatch between ZrN and Si is 16% and the thermal expansion coefficient ($7.24\times10^{-6}/°C$) of ZrN is much higher than that of Si($2.33\times10^{-6}/°C$). Previous study of ZrN [18] revealed that the primary factor prevailing the formation process of stoichiometric ZrN films was the selection of an optimum N_2 gas flow ratio. It was also found that the film resistivities were strongly dependent on the N_2 gas flow ratio and the film crystallinities were dependent on DC power and T_s. The optimum sputtering conditions obtained were as follows: N_2 gas flow ratio of 3% and a DC power of 15 W. Furthermore, it was found that epitaxial growth of high-quality stoichiometric (001) ZrN films with a resistivity of 17 μΩ cm comparable to that of bulk ZrN with a resistivity of 13.6 μΩ cm was achieved on (001) Si at T_s = 500 ºC, under the sputtering conditions described in paper [19]. ZrN film is

also epitaxially grown on MgO substrate as discussed by A.B Mei et. al [20]. MgO and ZrN are better lattice mismatch with 8% compared to 16 % with Si substrate. Single-crystal ZrN films, 830 nm thick, grew on MgO(001) at 450 °C by magnetically unbalanced reactive magnetron sputtering with a cube-on-cube orientational relationship, $(001)_{ZrN}\|(001)_{MgO}$ and $[100]_{ZrN}\|[100]_{MgO}$.

In this chapter ZrN films deposited using RF and DC reactive sputtering on various substrates (Si, quartz and MgO) are presented. Effects of process parameters on the film quality, determined from various characterization techniques, have been investigated. Epitaxial growth of ZrN using DC sputtering for the first time has been demonstrated.

Materials and methods

Thin films of ZrN_x have been grown on Si (100) and quartz substrates using radio frequency magnetron reactive sputtering using a 4 inch Zr target of 99.9 % purity in a mixed nitrogen and argon gases atmosphere. Before the deposition, the chamber was pumped down to a base pressure of lower than 5 x 10^{-4} Pa. The samples were deposited with a constant RF power of 100 W and a total pressure of 0.1 Pa. The films were deposited at different substrate temperatures from 100 ºC to 600 ºC for an hour with different nitrogen partial pressure ($N_2/(N_2+Ar)$) varies from 5% to 100%. The substrates were chemically cleaned using piranha solution and silicon substrates were dipped into HF solution to remove oxide from its surface prior to loading into the chamber. The sputter target was pre-sputtered for at least 10 minutes using argon gas before deposition to remove surface oxides and other impurities. Properties of RF sputtered ZrN films have been discussed in Section 4.1.

Thin films of ZrN have also been grown on MgO single sided polished (SSP) and double sided polished (DSP) substrates using an AJA sputter (same Zr target used as in RF sputtering). Before deposition, the chamber was pumped down to a base pressure lower than 10^{-6} Pa. The MgO substrates were chemically cleaned using ultrasonic bath (acetone + IPA) solution. The sputter target was sputter-cleaned using argon and nitrogen gas before deposition for, at least, 15 minutes to remove surface oxides and other impurities. The samples were deposited with constant DC power of 100 W and a total gas pressure of 0.1 Pa. The films were deposited at substrate temperature of 500 ºC for different duration from 5 minutes to 60 minutes with 3% and 5% of nitrogen gas flow. The films were subsequently annealed at 530 ºC in Ar^+ only atmosphere (~0.1 Pa) for 60 minutes in load lock chamber and then at 730 ºC in N_2 only atmosphere in MTI furnace. The sputtering gas flow was kept constant at 8 sccm. MgO substrates were degassed by heating for an hour at 500 ºC in pure argon gas atmosphere with a total gas pressure of 0.1 Pa. Resistivity of the deposited ZrN films on MgO was found to be ~ 14.9 μΩ cm using four point probe method. Properties of DC sputtered ZrN films have been discussed in Section 4.2

4.1. Study of ZrN_x films sputtered using RF reactive sputtering

ZrN_x films deposited using various T_s from RT to 600 ºC with 100 W RF power for 60 minutes. All the samples were deposited with 25% N_2 gas flow. GA-XRD of the samples deposited at various temperature are shown in Figure 4.1.1 (a). Films deposited at RT, 60 ºC and 100 ºC show one peak at ~ 55º and another peak at 33º. These peaks are attributed to Zr (220) and ZrN (111), respectively [18, 21]. When the growth temperature T_s is increased from RT to 100 ºC, Zr (220) signal diminishes

while ZrN (111) signal slightly increases which suggest formation of ZrN is enhanced at higher temperature. It is consistent with work done by H. Jiménez et.al [21]. The spectrum for the sample deposited at 200 ºC, shows dominant diffraction peak at ~30º which is attributed to ZrO_2 (111) along with small broad peaks around 52 ºand 63 º could be attributed to the ZrO_xN_y. This could be due to the oxidation of Zr metal or the strong affinity of Zr metal towards oxygen.

Figure 4.1.1 (b) shows GA-XRD measurements of ZrN_x films deposited at T_s >350 ºC Samples deposited with a T_s of 350 ºC exhibits a golden yellowish colour characteristic of stoichiometric zirconium nitride, while films deposited at higher substrate temperature have a darker blue shade which is a characteristics of ZrO_xN_y [22]. Thickness of the sample deposited at a substrate temperature 350 ºC is ~ 450 nm (measured using Dektak profilometer) whereas the films deposited at higher substrate temperature are correspondingly thinner which may be attributed to a lower sputter yield at high substrate temperature in the deposition chamber [23, 24]. Several ZrN_x peaks can be observed signifying the samples are poly-crystalline. Epitaxial growth of ZrN on Si is not predicted due to the large lattice mismatch (~16 %) between silicon and ZrN. The sample deposited at 350 ºC shows four distinct ZrN peaks, (100) at 32.1°, (101) at 36.6°, (102) at 47.9°, (103) at 63.4° and a small broad peaks at 68.5°, 69.7º, 77.7º and 82.0º representing the ZrN (200), ZrN (112), ZrN (202) and ZrN (104) peaks . A broad peak at around 54º is observed which indicates the ZrO_xN_y (600). Samples deposited at higher substrate temperature show only two main broad peaks around 30° and 54º representing ZrO_xN_y (222) and ZrO_xN_y (600), respectively, indicating oxidation of the films deposited above 500 º C. The observed Bragg peaks for the samples deposited with substrate temperature >350 ºC exhibit the cubic phase of ZrON.

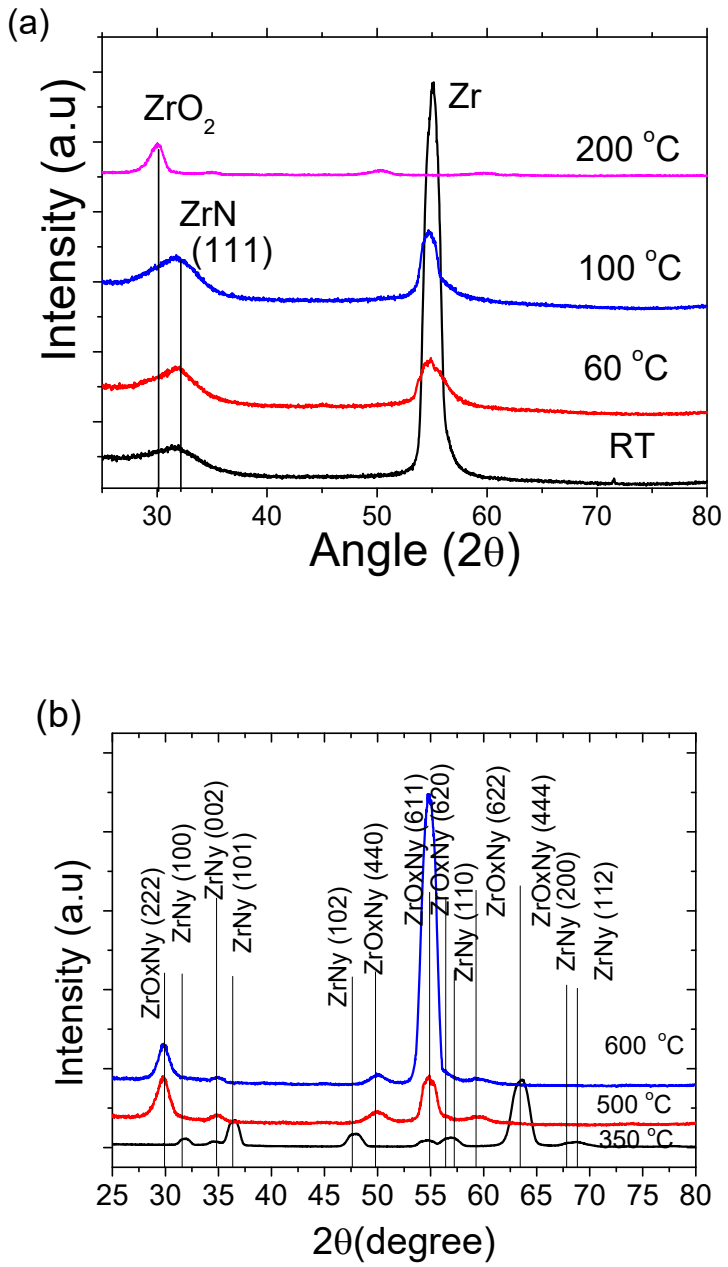

Figure 4.1.1: Results of GAXRD on the ZrN_x samples deposited at different substrate temperatures: (a) RT to 200 °C, and (b) 350 °C to 600 °C.

The chemical composition of the films was determined with XPS measurement. The composition was estimated by calculating the area under the respective peaks and then normalising with a scaling factor. XPS spectra of a representative sample deposited at 350 ºC are shown in Figure 4.1.2. Measurements were taken on the surface, and after etching the film for 240 seconds and 480 seconds minutes. Generally, the associations between N (1s) peaks positions and compounds are the following: 395.8 eV to ZrN_2 [25], 396.4 eV to Zr_3N_4 [25], 397.2 eV to ZrN [26],398.7–399.8 eV to ZrN_x with x<1 . However, in this case, N (1s) XPS spectra show only one broad peak centred around 397.2 eV which is attributed to the ZrN stoichiometry. The Zr (3d) peak around 180.5-181.2 eV is attributed to the ZrN species and that at 182.5 eV and 185.1 eV [25] are associated with ZrO_xN_y. These results are consistent with the XRD results. A Zr 3d peak shift slightly to higher BE whereas N 1s peak shifts slightly to lower BE with depth which is due to the transfer of charge between Zr and N. This could be due to electronegativity difference between Zr and N (pauling electronegativities: ~1.33 for Zr and ~3.04 for Nitrogen) [27]. Inset in Figure 4.1.2 shows the atomic composition of Zr (3d), N (1s) and O (1s) with film thickness. The composition of the film is essentially same in the bulk of the film. The peak around 55 eV for 350 ºC in XRD pattern in Figure 4.1.1 (b) evidenced the presence of oxygen in the film. The films are Zr-rich, with average N/Zr=0.58. The film contains about 20% oxygen which can be explained by the extremely high reactivity of zirconium transition metal with oxygen. Oxygen in the bulk of the film may be due to residual oxygen or moisture presence in the sputtering chamber (Chamber was not load lock) or oxidation of the sputtering target.

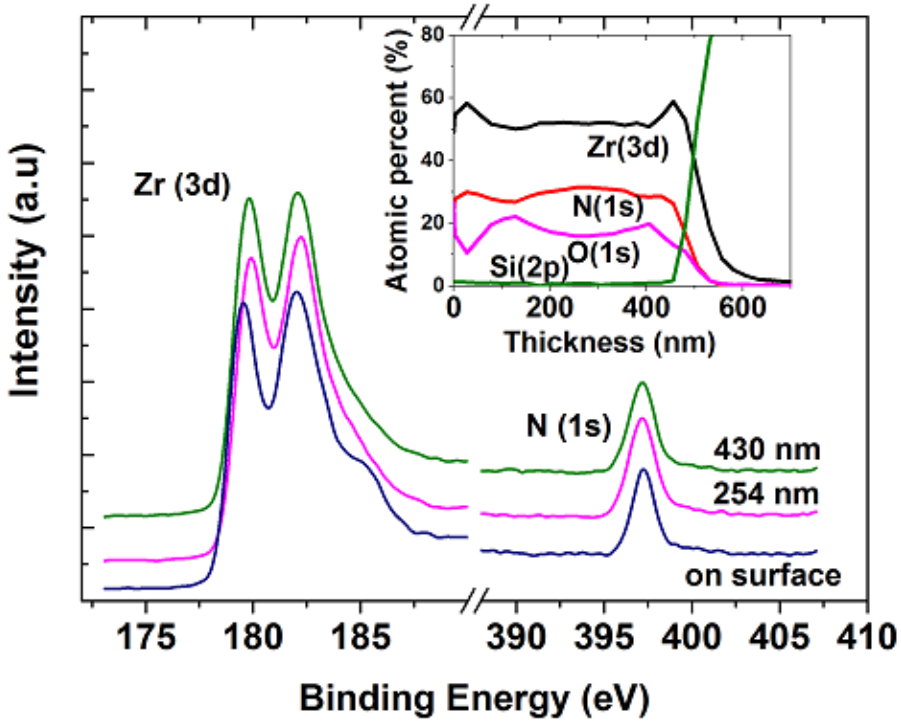

Figure 4.1.2: XPS spectra of a ZrN film deposited at 350 ºC with 25% nitrogen partial pressure. The inset shows the Zr (3d), N (1s), O (1s) and Si (2p) atomic percent of the film with thickness.

Figure 4.1.3 shows the XPS spectra of the ZrN_x sample grown at 600 ºC before and after Ar+ etching. Only Zr 3d, N 1s, and O 1s XPS spectra are shown. It shows the major peak shift of N1s (from 395.2 eV to 397.2 eV) towards higher binding energy and O 1s peak (from 531 eV to 530 eV) towards lower binding energy. However, there is only a slight shift in Zr 3d peak observed from 181.2 eV to 181.4 eV after Ar+ etching for the ZrNx sample deposited at 600 ºC.

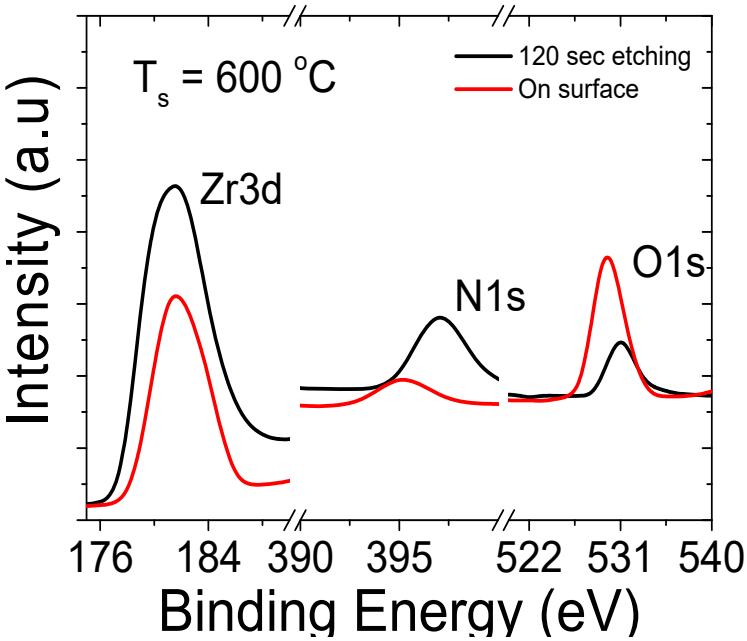

Figure 4.1.3: XPS spectra of the ZrN_x film deposited at 600 °C before (red) and after 120 sec (black) etching.

XPS peak fitting analysis of Zr 3d, N 1s and O 1s peaks at different temperatures was conducted to characterize the composition and chemical bonding state in the films. The Zr 3d, N 1s and O 1s spectra in Figure 4.1.4 of ZrN films were fitted by using two Gaussian components using a Levenberg-Marquardt (L-M) peak analyser algorithm keeping peak centre and FWHM as free parameters. It is evident that the quality of the fit is very good with r-square (coefficient of determination) value close to 0.9. In Figure 4.1.4 (b) and (d), Zr 3d spectrum of ZrN_x film deposited at 500 °C and 600 °C respectively has been shown after in situ cleaning of the sample by sputtering. The peak around 180 eV attributed to Zr 3d has been fitted with two peaks. The Zr 3d 5/2 component of film deposited at 500 °C at 180.2 eV corresponds to ZrN, the Zr 3d 5/2 component at 182.2 eV is attributed to the oxynitride (ZrON) compound while the component at 184.5 eV is associated to the oxide compound (ZrO_2) in agreement with work published by Wiame et al.[28]. The relative percentages of these components are

12%, 31% and 47%, respectively. In the correspondent N 1s spectrum (Figure 4.1.4 (a) and (c)) there are three components: 396.3 eV, 397.2 eV, and 398.1 eV as ZrN_2, ZrN and ZrON, with a quantitative contribution of 21%, 49% and 30% of the total nitrogen signal, respectively. The Binding energy of ZrN_2, ZrN and ZrON are closely matched with the references [25, 29, 30]. Taking into account the crystal structure of zirconium oxynitride suggested in paper [31-33], it is possible to make the following assignments. In this structure one nitrogen atom is four-coordinated, one is six-coordinated and the remaining two nitrogen atoms are five-coordinated. In the first case, this four-coordinated nitrogen atom can give an XPS peak at a binding energy (BE) position attributed to ZrN_2 material [31]. It represents the contribution labelled as 396.3 eV in the N 1s de-convoluted signal. The six-coordinated nitrogen atom belongs to a configuration typical of free-defects ZrN and its contribution has been labelled as 397.2 eV [25]. Moreover, here there is the 398.1 eV components, representing the oxynitride contribution [29]. This component can be evidenced on the O 1s fitted spectrum from the high binding energy side labelled as ZrON in Figure 4.1.4 (e). The ratio Zr:N:O is equal to 30%:50%:30%, which means it has an oxynitride compound with O/Zr = 1.0 and of N/Zr = 1.7 linked as a ternary compound. The (N + O)/Zr ratio of nearly 2 lets us to suppose an oxynitride ternary compound where the nitrogen replaces the oxygen in a ZrO_2 structure. The same analyses have been performed for sample deposited at 600 ºC and the compounds relative percentage is reported in Table 4.1. For ZrON films there is a competition between nitride and oxynitride components: the oxynitride compound is favourable at higher substrate temperature due to the affinity of Zr transition metal towards oxygen. It is presumed the nitrogen content of the film is underestimated due to the preferential sputtering of nitrogen over zirconium atomic species

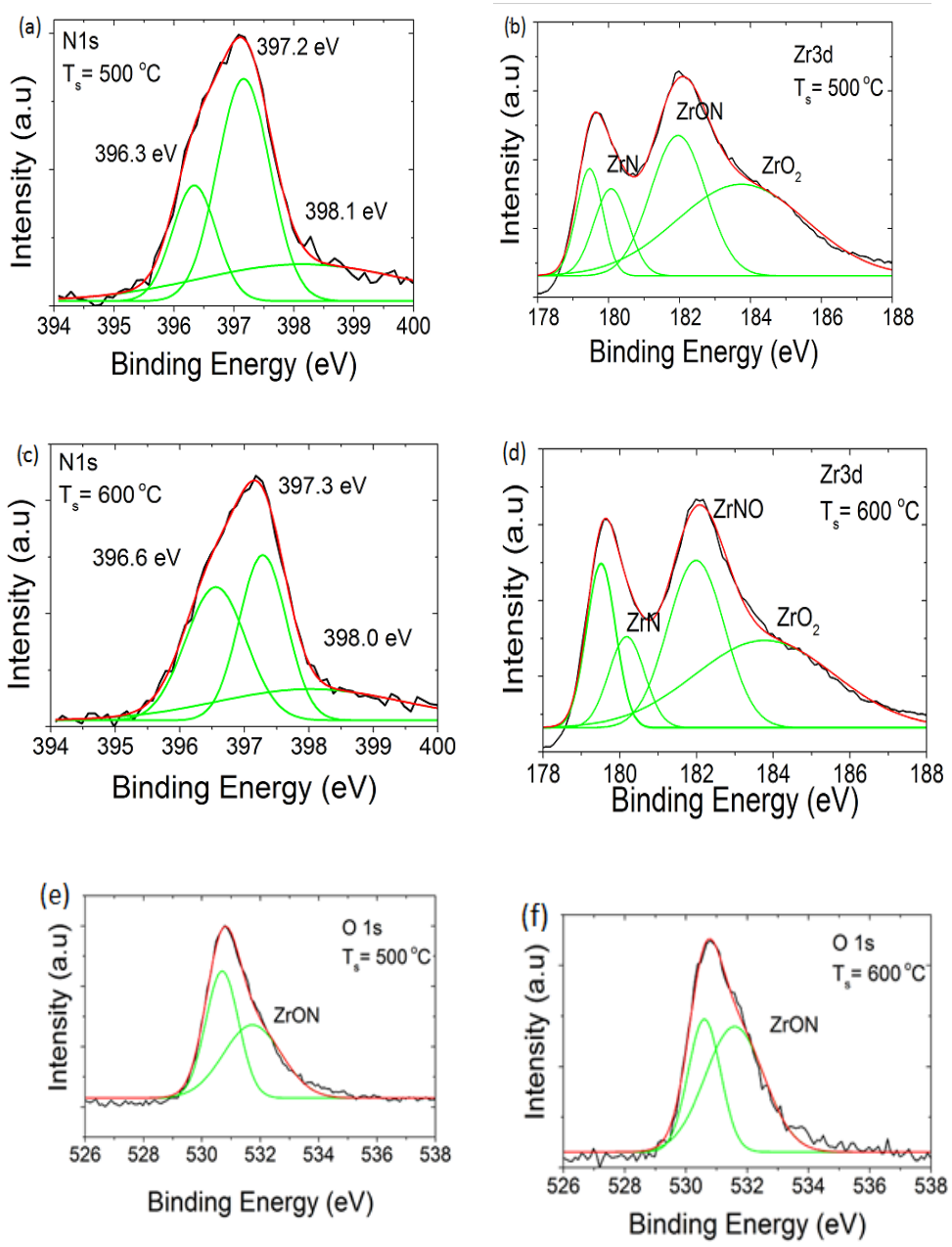

Figure 4.1.4: XPS core energy spectra Zr 3d, N 1s and O 1s for a- ZrN_x films after Ar+ bombardment at different T_s with 100 W RF. The black line is the experimental plot, red line is the fitted spectrum, and all green spectras are de-convoluted peaks assigned as indicated. The estimated error in the fitted peaks is less than 5% (a) N 1s 500 °C ,(b) Zr 3d 500 °C (c), N1s 600 °C (d), Zr 3d 600 °C (e), O 1s 500 °C and (f) O 1s 600 °C of ZrN_x film deposited

Table 4.1: Composition of films deposited with different substrate temperature. Film composition has been estimated by fitting Zr 3d XPS spectra.

Substrate Temperature (°C)	% Zr	% N	% O	% ZrN	% ZrNO	% ZrO_2
60	90.3	1.8	7.5	-	-	-
100	53.4	35.8	10.4	-	-	-
200	72.3	4.4	23.2	-	-	-
500	47.3	24.4	28.8	12	30	47
600	48.5	27.5	23.9	11	32	41

Figure 4.1.5 shows the Raman spectra of the ZrN_x samples deposited using different substrate temperature. The Raman spectra of the samples deposited at 350 °C shows two distinct peaks of the first order acoustic modes (150 -200 cm^{-1}) and first order optical modes (430 -530 cm^{-1}). Due to a large mass difference between nitrogen and transition metal Zr atoms; there are large gaps between the acoustic and optical modes. Three other modes are likely to be second order acoustic modes (300 - 350 cm^{-1}), optical – acoustic modes (~379 cm^{-1}) and optical + acoustic modes (~624 $cm^{-}1$) [14]. However, these modes are absent in the films deposited at higher substrate temperature could be due to the presence of oxygen in films grown at higher T_s. In stoichiometric ZrN which are rock salt structured, first order Raman peaks are forbidden by symmetry. The first order peaks observed can be attributed to point defects of the polycrystalline ZrN_x film[2]. These results agree with ZrN's phonon density of states calculated (as shown in Figure 4.1.1). This is favourable as we aim to exploit the large gap in the phonon DOS to slow down carrier cooling. As shown in Figure 4.1.5, the broad Raman peak at 480 cm^{-1} is associated with zone centred optical mode and small Raman peak at 140 cm^{-1} is associated with the acoustic peak [33-35]. The peaks in the Raman spectrum of ZrN deposited on quartz is relatively broad, whereas the Raman spectra of samples deposited on silicon substrates

displayed sharper and more defined peaks. This is an indication of the quality of the sample deposited on silicon substrates.

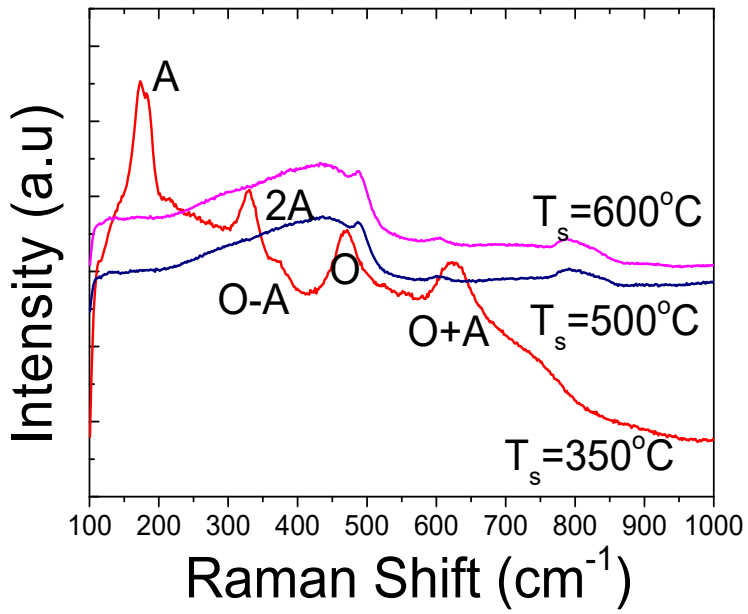

Figure 4.1.5: Raman Spectra of deposited ZrN_x films with 25% Nitrogen at different substrate temperatures.

The surface roughness of the deposited film was determined by AFM. Surface roughness is important characteristics since it can influence the electronic transport. Mean and RMS roughness are the most useful measurement to estimate the surface roughness. The RMS roughness is usually preferred over the mean roughness as it involves the sum of the squares of the deviation from the fitted plane surface, which is always a positive quantity. AFM images of the ZrN_x film deposited at substrate temperatures 500 ºC and 600 ºC are shown in Figure 4.1.6. (a) and (b) in 3D (left) and 2D (right). The film grown at T_s =500 ºC has an RMS roughness of 1.71 nm, whereas the film at T_s =600 ºC has an RMS value of 1.87 nm. As can be seen from Figure 4.1.6 (a) and (b), the grain sizes in the deposited films are very uniform, and the surface are

very dense and smooth. Roughness value is more for the film deposited at higher substrate temperature which is consistent with previously published results [25, 36]

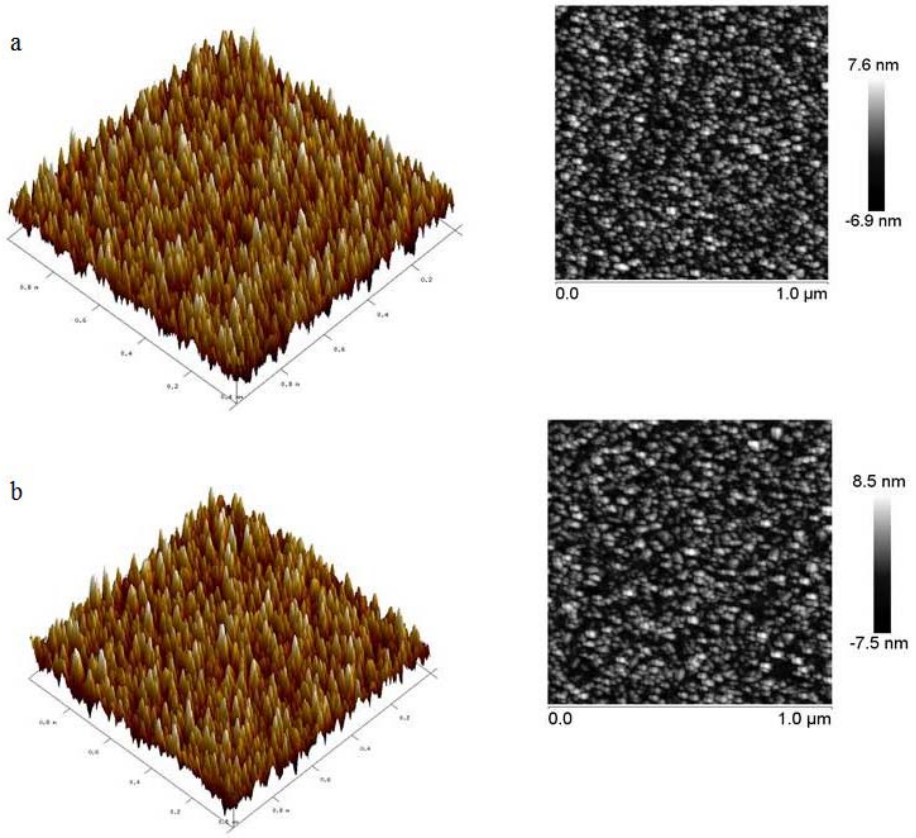

Figure 4.1.6: AFM image of the ZrN_x film deposited at (b) 500 °C (3D left and 2D right) and (c) 600 °C (3D left and 2D right) shows the RMS roughness value of 1.71 nm and 1.87 nm respectively for 1 μm^2 area.

Absorption coefficient was calculated using the following approximation

$$\alpha \approx -\frac{1}{d}\ln\left(\frac{T}{(1-R)^2}\right) \quad [\mathrm{cm}^{-1}]$$

Where d is the film thickness, T is the transmittance and R is the reflection of the thin film as measured by a spectrometer. The Figure 4.1.7 main shows that the absorption coefficient is not constant but still depends strongly on wavelength. The minima of the absorption coefficient around 530 nm for the sample deposited at 500 ºC and 600 ºC represent the transition point from free electron absorption and reflection to interband transition for shorter wavelength. Figure 4.1.7 inset shows the absorption coefficient of sample deposited at 350 ºC. The transition point for this sample is at 580 nm.

Thickness of the films deposited at 500 ºC and 600 ºC was approximately 100 nm. Figure 4.1.8 shows the reflection and transmission spectra of the ZrN_x film deposited at 500 ºC used to determine the absorption coefficient. The reflection spectrum shows a minimum at 430 nm while the transmittance has a maximum at 450 nm. The transmittance does not reduce to zero evidently at long wavelengths showing the metallic nature of the material with free carrier absorption of low energy photons. Strong absorption is evident at low wavelengths from inter-band transitions and at long wavelengths free carrier absorption. In the region at longer wavelengths than the absorption minimum is characteristic of free electron absorption from the Zr d-states through intraband transitions [27]. The optical properties of the ZrN_x shows there is strong free carrier absorption from ~500 nm onwards. In conjunction with the high absorption at low energy levels the reflectivity is also low in this region. The absorption and reflection by free electrons in the material is indicative of the metallic nature of ZrN_x. The steady state optical spectroscopy measurements agree with the optical properties and the density of states of ZrN calculated from first principles and other experimental studies[37, 38]. ZrN is able to absorb light within the solar spectral range,

with strong absorption at low wavelengths, particularly at long wavelengths beyond 1100 nm which not utilised in silicon based photovoltaic devices. To optimally use ZrN as an absorber optical light trapping such as using antireflection coatings and nanostructures would be required to minimise the reflection and enhance the optical light path to promote absorption.

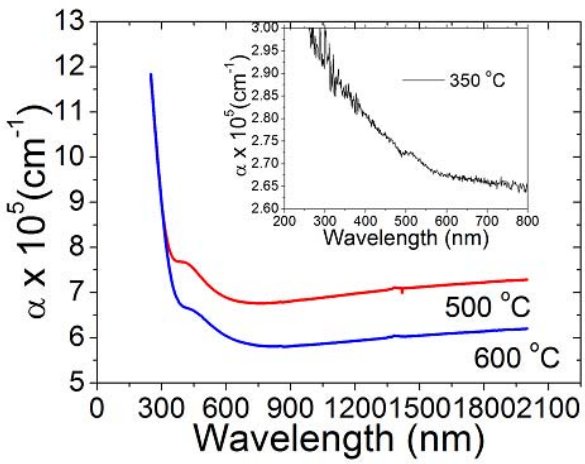

Figure 4.1.7: Absorption coefficient vs wavelength plot for the films deposited at 500 °C (red) and 600 °C (blue). Inset shows results for the film deposited at 350 °C.

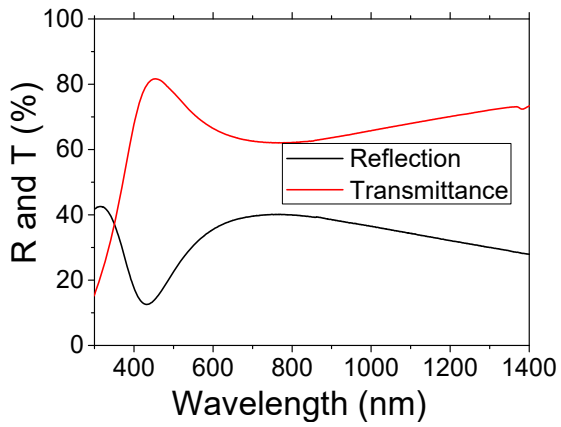

Figure 4.1.8: Transmission and reflection measurement for ZrN_x sample deposited at 500 °C

.

Summary

The growth of ZrO_xN_y thin films has been demonstrated using cost-effective RF magnetron sputtering. ZrN_x thin films deposited on Si (100) and quartz substrates are polycrystalline. XRD results indicate that the film is more metallic when deposited at low temperature < 200 ºC with higher percentage (90.3 %) of Zr whereas higher substrate temperature > 500 ºC favours the formation of ZrO_xN_y. XPS measurement supports the XRD results and shows the formation of nitrogen-poor ZrN_x at T_s < 200 ºC. Raman spectroscopy measurements demonstrate for the sample deposited > 500 ºC that there is an agreement between the Raman spectra and theoretical zone centred phonon modes. Phononic and carrier cooling properties of the films deposited at T_s > 500 ºC, investigated using ultrafast transient absorption spectroscopy,are presented in Chapter 5.

4.2. Epitaxial growth of ZrN (100)/ MgO (100) using DC sputtering

Epitaxial deposition of ZrN has been investigated by DC sputtering on MgO substrate. MgO and ZrN are better lattice mismatch with 8% compared to 16 % with Si substrate. Therefore, it is possible to grow epitaxial ZrN on MgO. Films have been deposited using Zr sputtering target in Ar and nitrogen gas atmosphere. The samples were deposited with constant DC power of 100 W and a total gas pressure of 0.1 Pa. The films were deposited at substrate temperature of 500 ^{o}C for different duration from 5 minutes to 60 minutes with 5% of nitrogen gas flow.

The as-sputtered ZrN films show mirror-like surface from appearance. The epitaxial nature of the deposited ZrN films was characterized by XRD, X-ray pole figure analyses with Cu Kα radiation, and also by cross-sectional TEM.

XRD ω-2θ scans, over the 2θ range from 20°–110° diffraction angles, of a film deposited at 500 ^{o} C are shown in Figure 4.2.1. ZrN films were deposited on SSP MgO (100) substrate for 5 minutes, 20 minutes and 60 minutes at 100 W RF power. The film deposited for 5 mins doesn't show any ZrN peak except substrate peaks of MgO (200) and MgO (400). This indicates that the deposited film is amorphous in nature after 5 mins of deposition. But, after 20 minutes of deposition, five peaks are identified. Out of them, two peaks belong to ZrN peaks in (111) and (222) directions at 2θ = 34.3 ^{o} and 72.3 ^{o}, respectively and other three peaks attributed to MgO (100), MgO (200) and MgO (400) reflections at 2θ = 22 ^{o}, 42.9 ^{o} and 94.1 $^{o.}$ Similarly, the film deposited for 60 minutes reveals only five peaks, out of them two peaks corresponding to (200) and (400) ZrN planes and others related to substrate reflections, indicating (100) preferred orientation. ZrN (200) and (400) reflections at 39.15 ^{o} and 84.31 ^{o} are symmetric with FWHM intensities of 1.09 and 2.73, respectively. It is also observed from Figure 4.2.1

that ZrN deposited in {111} direction when sputtered for 20 minutes and in {100} direction when sputtered for 60 minutes. This observation needs further investigation to understand why the preferred orientation change with deposition time.

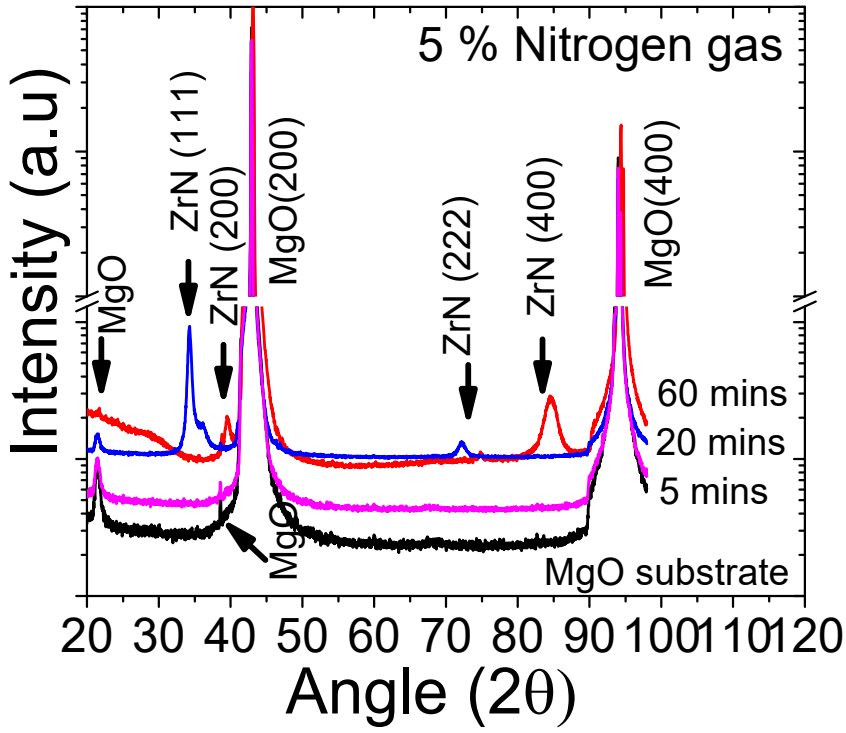

Figure 4.2.1: XRD ω-2θ scans from a ZrN layer grown on MgO (100) by DC reactive sputtering at T_s = 500 °C for 5 mins (pink), 20 mins (blue) and 60 mins (red).

The ZrN film deposited for 60 minutes is annealed for an hour at 530 °C in a load lock chamber in Ar only atmosphere shows enhancement of ZrN (200) peak but a detraction of ZrN (400) as shown in Figure 4.2.2 (a). This film is further annealed at higher T_s = 730 °C in MTI furnace (Maximum temperature allowed in load lock chamber is 600 °C) in N_2 only atmosphere. The film then shows peaks corresponding to ZrN (111), ZrN (222) and ZrO_2 (200) and ZrO_2 (400). XRD spectrum after annealing at 730 °C is

redrawn as an inset in Figure 4.2.2 (a) for a clear view. The change of ZrN orientation from (200) to (111) in the film after annealing could be due to formation of ZrN as a result of annealing at higher substrate temperature of 730 ºC in N_2 only atmosphere [39]. The formation of ZrO_2 phase could be due to the introduction of oxygen during annealing [39] (MTI furnace is not load lock chamber) and Zr has strong affinity towards oxygen. Moreover, the bond strength of Zr-O is stronger than that of Zr-N (BE of Zr-O is 182 Kcal/mol whereas Zr-N is 135 kcal/mol) [37]

A narrow region of a ω-2θ scan for the film annealed at 530 ºC is presented in Figure 4.2.2 (b). The peaks centred at 38.8° and 42.9º are indexed as (200) ZrN and (200) MgO, respectively [11, 19, 20]. From the known lattice constant of MgO, $a_s = 0.421$ nm [20, 40] and the measured angular separation between the two peaks, $\Delta 2\theta = 4.1°$, the ZrN lattice parameter $a_\perp$ along the film growth direction can be calculated to be 0.467 nm. The lattice constant and gain size, calculated from XRD, for the three ZrN samples are tabulated in Table 4.2.1. The lattice constant of as-deposited films of the cubic ZrN are calculated from the equation: $a = \lambda*((h^2 + k^2 + l^2)^{1/2})/ (2*\sin(\theta))$, where h, k and l are Miller indices and a is the standard lattice parameter of ZrN bulk specimen, whereas grain size are calculated using known Scherrer equation [41]. The lattice constant value for the ZrN film deposited for 60 minutes is in a good agreement with the value expected for stoichiometric ZrN of 0.4577 by H. Yanagisawa et.al [11, 17].

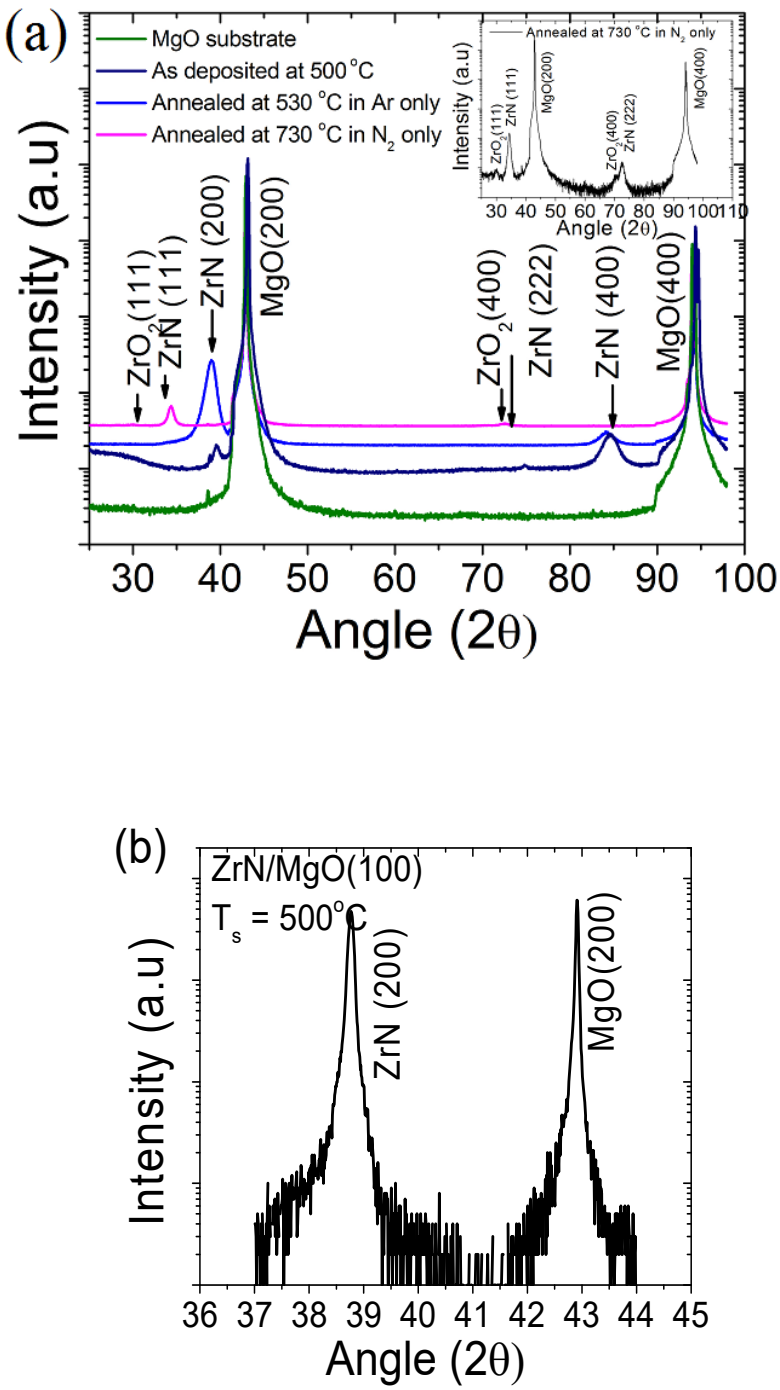

Figure 4.2.2: (a) XRD spectra of MgO (100) substrate (black) and ZrN films grown at 500 °C (dark blue), after annealing at 530 °C in Ar only atmosphere (sky blue) and further annealing at 730 °C (pink) in N_2 gas only atmosphere (b) A section of ω-2θ scan for the film annealed at 530 °C highlighting ZrN(200) and MgO(200) peaks.

Table 4.2.1: Calculated lattice constant and gain size of ZrN films deposited for different durations. Results of other theoretical calculations and experimental data are listed separately after the table.

N_2 gas flow	Time (mins)	ZrN orientation present in the films deposited		Lattice constant of the film (nm)	Grain Size Å
5 %	60	ZrN (200)	ZrN (400)	0.457	12.30
	20	ZrN (111)	ZrN (222)	0.454	12.92
	5	-	-	-	

Lattice constant of ZrN film from other calculations and value of experimental data are follows 0.4578 nm (bulk), 0.457 nm [42], 0.4583 nm [35], 0.4537 nm [43], and 0.459 nm [1].

Pole figure analysis is done to further confirm the presence of epitaxial ZrN film. A pole figure (in the context of texture) is a map of a selected set of crystal plane normals plotted with respect to the sample or reference frame. It is used to determine the distribution of crystallographic orientation. To obtain pole figure, HR-XRD scans from ZrN and MgO, obtained in the parallel-beam mode with ω and 2 θ angles set to detect the (220) peaks at a tilt angle of 45° with respect to the surface normal, are plotted in Figure 4.3.2(a). The results show four 90° rotated (220) peaks at the same φ angles for both ZrN and MgO. The combination of the XRD ω-2 θ and φ scans demonstrate that ZrN (100) layers grow epitaxially with a cube-on-cube relationship to the substrate: (100) ZrN ∥ (100) MgO.

The annealed film is confirmed to be epitaxial by the four-fold symmetry of the (100) reflection in pole figure studies in Figure 4.2.3(b) and indicated that the film has an epitaxial relationship with the single crystal MgO substrate.

From XPS measurement, it was found that ZrN sample contains ~41 % N_2, 53 % Zr and 6 % oxygen after 120 seconds Ar+ etching. The ZrN film is Zr rich with N/Zr ratio as 0.77. Oxygen amount is considerable reduced from 20 % for the sample deposited at 500 ºC, 25 % N_2 using RF sputtering in modified sputter system discussed in Section 4.1. This indicate the introduction of oxygen in the sample can be controlled by using high vacuum and load lock chamber of AJA sputter chamber compared to single target sputter machine.

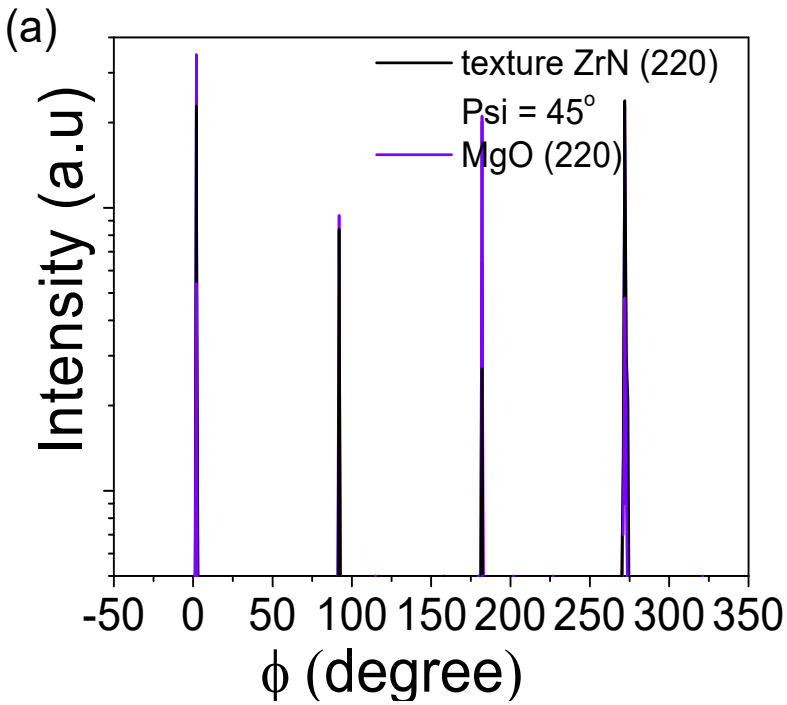

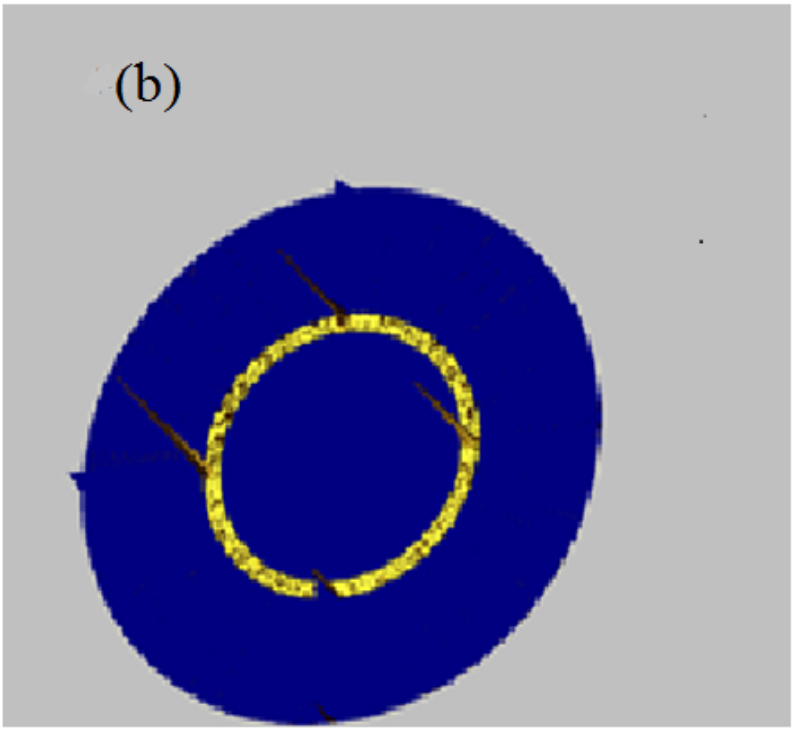

Figure 4.2.3 (a) ZrN (black) and MgO (purple) XRD (220) scans from the annealed ZrN sample at 530°C). They are overlayed. (b) Pole Figures measurement done at 2θ = 56.8 °, showing the reflections of ZrN film.

Figure 4.2.4 shows Raman spectra of the as-deposited and annealed ZrN films. All the peaks near 178 cm^{-1} and 240 cm^{-1} attributed to TA and LA phononic modes in acoustic region respectively due to the vibration of heavy Zr ion [44] and in the optic region at 505 cm^{-1} due to the vibration of lighter N ions. There is no sign of secondary phases within the detection limit [33, 44, 45]. This is a good agreement with reported Raman studies by J.Y.Li [45] and C. Moura [33]. Whereas, after annealing at 730 °C, peak related with ZrN TA, LA and optic modes are lost. It could be due to the formation of ZrO_2 (111) phase.

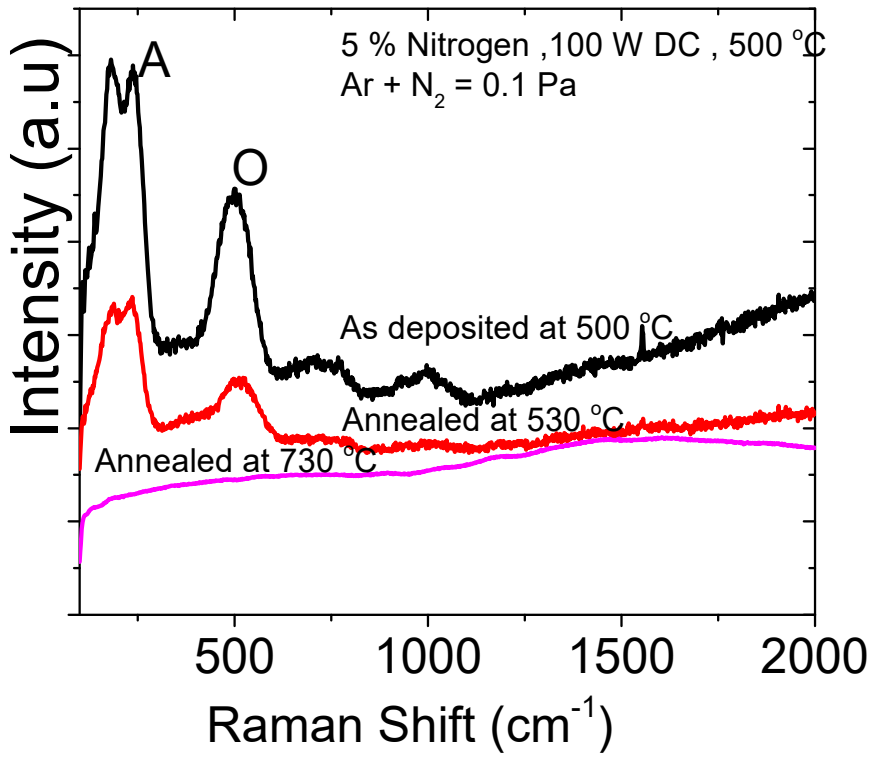

Figure 4.2.4: Raman spectra of the ZrN films as deposited (black) at 500 °C, annealed (red) at 530 °C and further annealed at 730 °C (pink).

A HRTEM cross-sectional image of the ZrN-MgO (100) interface region shown in Figure 4.2.5. A Phillips CM200 operated at 200 kV was used for TEM analysis. The ZrN layer is well aligned with the substrate, illustrating the successful heteroepitaxial growth of ZrN on MgO. From the TEM image, d-spacing has been calculated which gives lattice constant around 4.53 ± 0.5 Å Calculated lattice contact of deposited ZrN film from TEM image is closely matched with the value (0.457 nm) from XRD peaks.

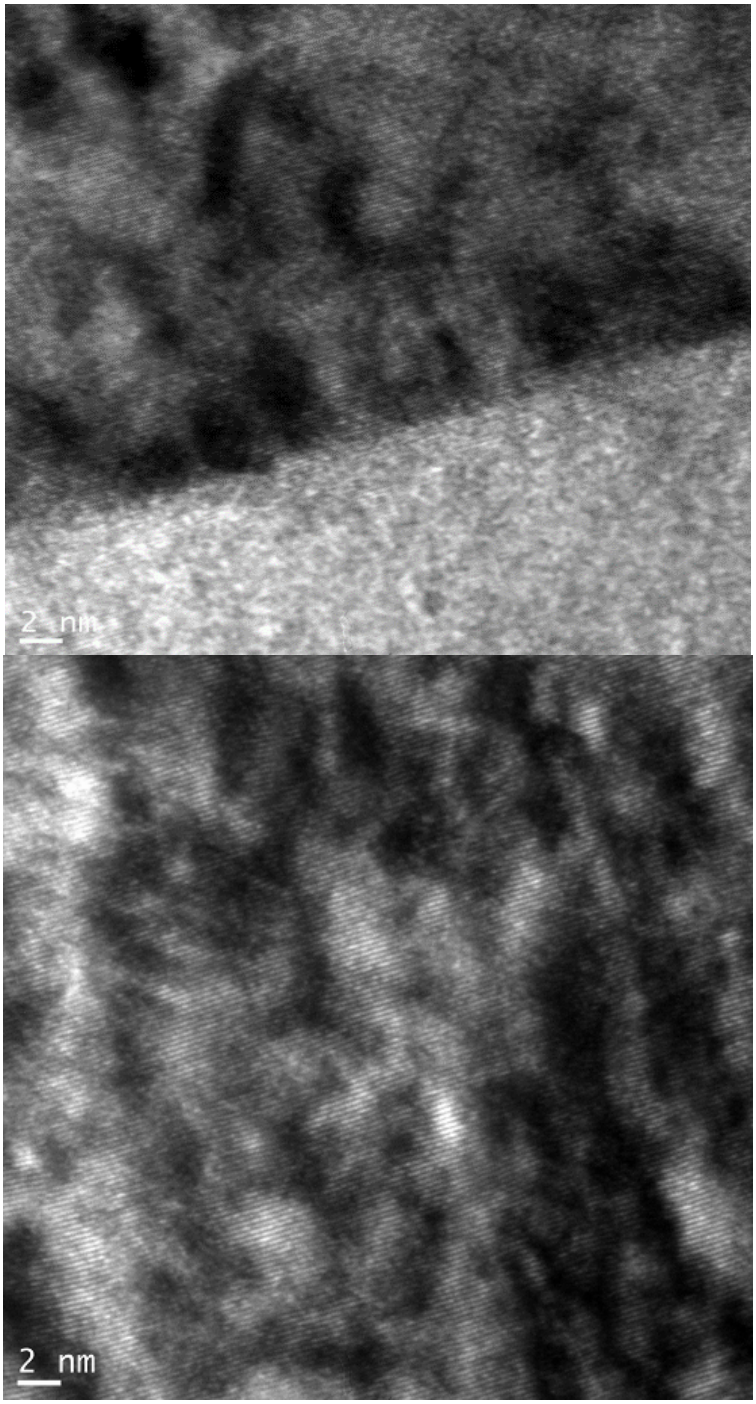

Figure 4.2.5: Cross-sectional TEM image obtained from ZrN on MgO (100) substrate.

Summary

Epitaxial ZrN thin films were successfully grown on MgO (100) substrates by DC reactive sputtering from a single Zr target after annealing at 530 ºC. The epitaxial growth of ZrN was confirmed by XRD and X-ray pole diagram using Phi scan. XRD result confirmed the growth of ZrN in {100} on MgO (100) with cube on cube orientation with 5% of nitrogen gas flow. It was further confirmed by means of HRTEM that ZrN film is grown epitaxially with lattice constant of 0.457 nm. Structural properties of the as-deposited ZrN film on MgO (100) by DC sputtering technique were further investigated and compared with the post-annealed film at 730 ºC under N_2 ambient in MTI furnace (not load locked). It was revealed after XRD measurement that the ZrN {100} phase was lost with the growth of ZrO_2 (100) phase after annealing at 730 ºC in MTI furnace.

4.3. Bibliography

1. Saha, B., Acharya, Jagaran,Sands, Timothy D.,Waghmare, Umesh V., *Electronic structure, phonons, and thermal properties of ScN, ZrN, and HfN: A first-principles study.* Journal of Applied Physics, 2010. **107**(3).
2. Christensen, A.N., Dietrich, O. W.,Kress, W.,Teuchert, W. D., *Phonon anomalies in transition-metal nitrides: ZrN.* Physical Review B, 1979. **19**(11): p. 5699-5703.
3. Schroeder, J.L., et al., *Bulk-Like Laminated Nitride Metal/Semiconductor Superlattices for Thermoelectric Devices.* Microelectromechanical Systems, Journal of, 2014. **23**(3): p. 672-680.
4. Naik, G.V., V.M. Shalaev, and A. Boltasseva, *Alternative Plasmonic Materials: Alternative Plasmonic Materials: Beyond Gold and Silver (Adv. Mater. 24/2013).* Advanced Materials, 2013. **25**(24): p. 3258-3258.
5. Conibeer, G., et al. *Hot carrier solar cell absorbers: materials, mechanisms and nanostructures*. 2014.
6. Chung, S., et al., *Hafnium nitride for hot carrier solar cells.* Solar Energy Materials and Solar Cells, 2014(0).
7. Shrestha, S., et al. *Evaluation of hafnium nitride and zirconium nitride as Hot Carrier absorber*. in *Photovoltaic Specialist Conference (PVSC), 2014 IEEE 40th*. 2014.
8. Yao, Y. and D. König, *Comparison of bulk material candidates for hot carrier absorber.* Solar Energy Materials and Solar Cells, 2015. **140**: p. 422-427.
9. Meng, Q.N., et al., *Preferred orientation, phase transition and hardness for sputtered zirconium nitride films grown at different substrate biases.* Surface and Coatings Technology, 2011. **205**(8–9): p. 2865-2870.
10. Johansson, B.O., et al., *Higher nitrides of hafnium, zirconium, and titanium synthesized by dual ion beam deposition.* Journal of Materials Research, 1986. **1**(03): p. 442-451.
11. Yanagisawa, H., et al., *Epitaxial growth of (111) ZrN thin films on (111) Si substrate by reactive sputtering and their surface morphologies.* Journal of Crystal Growth, 2006. **297**(1): p. 80-86.
12. Liu, C.-P. and H.-G. Yang, *Systematic study of the evolution of texture and electrical properties of ZrNx thin films by reactive DC magnetron sputtering.* Thin Solid Films, 2003. **444**(1–2): p. 111-119.
13. Chen, C.S., et al., *Influence of the preferred orientation and thickness of zirconium nitride films on the diffusion property in copper.* Journal of Vacuum Science and Technology B: Microelectronics and Nanometer Structures, 2004. **22**(3): p. 1075-1083.
14. Pilloud, D., et al., *Effect of germanium addition on the properties of reactively sputtered ZrN films.* Thin Solid Films, 2005. **492**(1–2): p. 180-186.
15. Ramos, H.J. and N.B. Valmoria, *Thin-film deposition of ZrN using a plasma sputter-type negative ion source.* Vacuum, 2004. **73**(3-4): p. 549-554.
16. Horita, S., T. Toda, and H. Kasagawa, *Epitaxial growth of a (101) Pb(ZrxTi1-x)O3 film on an epitaxial (110) Ir/(100) ZrN/(100) Si substrate structure.* Japanese Journal of Applied Physics, Part 1: Regular Papers and Short Notes and Review Papers, 2002. **41**(11 B): p. 6653-6657.
17. Barnett, S.A., et al., *Epitaxial growth of ZrN on Si(100).* Applied Physics Letters, 1988. **53**(5): p. 400-402.
18. Yanagisawa, H., et al., *Study on preparation conditions of high-quality ZrN thin films using a low-temperature process.* Japanese Journal of Applied Physics, Part 1: Regular Papers and Short Notes and Review Papers, 1998. **37**(10): p. 5714-5718.
19. Yanagisawa, H., et al., *Epitaxial growth of (001)ZrN thin films on (001)Si by low temperature process.* Japanese Journal of Applied Physics, Part 1: Regular Papers and Short Notes and Review Papers, 2005. **44**(1 A): p. 343-349.

20. Mei, A.B., et al., *Physical properties of epitaxial ZrN/MgO(001) layers grown by reactive magnetron sputtering.* Journal of Vacuum Science & Technology A, 2013. **31**(6): p. -.
21. Jiménez, H., E. Restrepo, and A. Devia, *Effect of the substrate temperature in ZrN coatings grown by the pulsed arc technique studied by XRD.* Surface and Coatings Technology, 2006. **201**(3–4): p. 1594-1601.
22. Klumdoung, P., et al., *Variation of color in Zirconium nitride thin films prepared at high Ar flow rates with reactive dc magnetron sputtering.* Procedia Engineering, 2012. **32**(0): p. 916-921.
23. Rizzo, A., et al., *Influence of growth rate on the structural and morphological properties of TiN, ZrN and TiN/ZrN multilayers.* Thin Solid Films, 2007. **515**(17): p. 6665-6671.
24. Liu, C.-P. and H.-G. Yang, *Deposition temperature and thickness effects on the characteristics of dc-sputtered ZrNx films.* Materials Chemistry and Physics, 2004. **86**(2–3): p. 370-374.
25. Del Re, M., et al., *Study of ZrN layers deposited by reactive magnetron sputtering.* Surface and Coatings Technology, 2003. **174–175**(0): p. 240-245.
26. Bertoti, I., et al., *Surface chemical changes in PVD TiN layers induced by ion bombardment.* Surface and Interface Analysis, 1994. **21**(6-7): p. 467-473.
27. Allred, A.L., *Electronegativity values from thermochemical data.* Journal of Inorganic and Nuclear Chemistry, 1961. **17**(3–4): p. 215-221.
28. Wiame, H., et al., *Thermal oxidation under oxygen of zirconium nitride studied by XPS, DRIFTS, TG-MS.* Journal of the European Ceramic Society, 1998. **18**(9): p. 1293-1299.
29. Mohamed, S.H., A.M.A. El-Rahman, and R.A. Mahrous, *Investigation of zirconium oxynitride thin films deposited by reactive pulsed magnetron sputtering.* Journal of Physics D: Applied Physics, 2007. **40**(22): p. 7057.
30. Signore, M.A., et al., *Investigation of the physical properties of ion assisted ZrN thin films deposited by RF magnetron sputtering.* Journal of Physics D: Applied Physics, 2010. **43**(22): p. 225401.
31. Rizzo, A., et al., *Physical properties evolution of sputtered zirconium oxynitride films: effects of the growth temperature.* Journal of Physics D: Applied Physics, 2009. **42**(23): p. 235401.
32. Cunha, L., et al., *Structural evolution in ZrNxOy thin films as a function of temperature.* Surface and Coatings Technology, 2006. **200**(9): p. 2917-2922.
33. Moura, C., et al., *Raman spectra and structural analysis in ZrOxNy thin films.* Thin Solid Films, 2006. **515**(3): p. 1132-1137.
34. Spengler, W. and R. Kaiser, *First and second order Raman scattering in transition metal compounds.* Solid State Communications, 1976. **18**(7): p. 881-884.
35. Isaev, E.I., et al., *Phonon related properties of transition metals, their carbides, and nitrides: A first-principles study.* Journal of Applied Physics, 2007. **101**(12): p. 123519.
36. Zhou, M., et al., *Influence of sputtering conditions on microstructure and mechanical properties of ZrN films prepared by radio-frequency-reactive sputtering.* Journal of Vacuum Science & Technology A: Vacuum, Surfaces, and Films, 2003. **21**(5): p. 1791-1795.
37. Lamni, R., et al., *Optical and electronic properties of magnetron sputtered ZrNx thin films.* Thin Solid Films, 2004. **447–448**(0): p. 316-321.
38. Benia, H.M., et al., *Optical properties of non-stoichiometric sputtered zirconium nitride films.* Applied Surface Science, 2003. **211**(1–4): p. 146-155.
39. Larijani, M.M., et al., *Effects of post annealing on micro and nanostructural properties of ZrN films prepared by ion beam sputtering technique on SS304.* Surface and Coatings Technology, 2009. **203**(17–18): p. 2486-2489.
40. Smith, D.K. and H.R. Leider, *Low-temperature thermal expansion of LiH, MgO and CaO.* Journal of Applied Crystallography, 1968. **1**(4): p. 246-249.

41. Zhong, Y., et al., *Determination of grain size by XRD profile analysis and TEM counting in nano-structured Cu.* Journal of Alloys and Compounds, 2009. **476**(1–2): p. 113-117.
42. Stampfl, C., et al., *Electronic structure and physical properties of early transition metal mononitrides: Density-functional theory LDA, GGA, and screened-exchange LDA FLAPW calculations.* Physical Review B, 2001. **63**(15): p. 155106.
43. Wyckoff, R.W.G., *Crystal Structure,*, ed. 2nd. Vol. 1. 1963, New York: Wiley.
44. Constable, C.P., J. Yarwood, and W.D. Münz, *Raman microscopic studies of PVD hard coatings.* Surface and Coatings Technology, 1999. **116–119**: p. 155-159.
45. Li, J.Y., et al., *Zirconium nitride (ZrN) fibers prepared by carbothermal reduction and nitridation of electrospun PVP/zirconium oxychloride composite fibers.* Chemical Engineering Journal, 2008. **144**(1): p. 149-152.
46. Harley, R.T., J.B. Page Jr, and C.T. Walker, *Experimental and theoretical study of raman scattering in Tl+ -doped alkali halides.* Physical Review B, 1971. **3**(4): p. 1365-1381.
47. Montgomery Jr, G.P., et al., *Raman scattering and far-infrared absorption induced by silver ions in sodium chloride.* Physical Review B, 1972. **6**(10): p. 4047-4060.
48. J.M., et al., *X-Ray diffraction investigations of magnetron sputtered TiCN coatings.* Surface and Coatings Technology, 1995. **74-75**(PART 1): p. 312-319.

Chapter 5

Hot carrier cooling in ZrN film

Slow cooling is an essential prerequisite for successful hot carrier solar cells (HC-SC). Although extensive theoretical and simulation work has been undertaken, experimental study of hot carrier cooling is rarely reported. In this chapter, the carrier thermalization in ZrN_x using ultrafast transient absorption (TA) spectroscopy is explored for the first time. Carrier lifetime of the order of hundreds of picosecond is evidenced from TA measurements. The findings reported in this chapter may be useful for the implementation of advance photovoltaic concept such as HC-SC.

Introduction

As discussed in Chapter 4, ZrN has the potential to be used as a HCSC absorber [1-17]. As stated before, ZrN has large phonon band gap due to the large mass difference between its constituent atoms. A wide phonon band gap in ZrN is expected to prevent the Klemens' decay and reduce Ridley decay pathways. A material such as ZrN with a wide phononic gap can increase the optical phonon lifetime and thus enable the electron population to be re-energized and maintained at a higher energy. This occurs due to the large difference between the mass of the Zr and N atoms in the material. The phenomena of a wide phonon gap leading to decreased carrier cooling rates has been demonstrated in an experiment on GaAS and InP using time-resolved photoluminescence comparing similar materials in which one has a phononic band gap while the other does not [18].

The absorber is required to maintain a hot carrier population for a long enough time for the hot carriers to be extracted. Exploiting or engineering the phononic properties of

materials can lead to a long carrier lifetime. In this Chapter, the carrier cooling properties using ultrafast relaxation of carriers in bulk ZrN_x thin films by means of femtosecond (fs) pump-probe transient absorption spectroscopy is reported. However, until now significantly slowed cooling of hot carriers is rarely observed experimentally, both for bulk and quantum dots. In this investigation, ZrN_x films fabricated using RF magnetron reactive sputtering show as long as hundreds of picoseconds slow cooling time. Structural, compositional, optical and phononic properties of deposited films have been discussed in Chapter 4.

Materials and method

Samples investigated in this work are given in Table 5.1. Zirconium nitride (ZrN_x) thin films have been deposited by RF sputtering. Characterization and deposition methods of ZrN have already been discussed in Chapter 4's introduction [4-17]. The structural, compositional, phononic and optical properties of deposited ZrN films using RF sputtering have been discussed in Chapter 4, Section 4.1.

The composition of the films was estimated from XPS. The sample was etched for 60 seconds using a 1 keV Argon ion beam to study the bulk composition. Composition (N, Zr and O content) of the films are shown in Table 5.1. The composition of the films have been estimated by fitting XPS spectra, as described in Chapter 4, Section 4.1.

Table 5.1: Key properties of ZrN samples investigated by transient absorption.

Sample ID	Growth method	Growth Temperature (ºC)	Thickness (nm)	Composition (%)			Crystal size (nm)
				Zr	N	O	
A	RF sputter	500 ºC	~ 92	~48	~28	~24	~10.5
B	RF sputter	600 ºC	~ 100	~50	~29	~21	~11.0

5.1 Ultrafast transient absorption measurement

Ultrafast pump-probe transient absorption (TA) measurements are commonly used to study charge dynamics in materials [19-21]. In this method, the sample is exposed to an ultra-short laser pulse. Immediately after the ultra-short laser irradiation, electrons are excited to high excited states which causes variations in the optical properties from the steady state conditions due to the change in occupied electron states as they relax down to lower energy states. This process is repeated at different time delays. Transmission spectra before and after the pump pulse gives the information on change in absorption characteristics with and without pump excitation of electronic states. Femtosecond pump-probe experiments were performed with a transient absorption spectrometer (FemtoFrame II, IB Photonics). The experiment used both an excitation source of 400 nm and 360 nm pulse with a fluence of 36 μJ/cm^2 from an OPA laser (TOPAS, Spectra Physics) with 100 fs duration and 1 kHz repetition rate. The probe beam of white light

continuum was generated by focusing the 1 kHz Ti:sapphire amplified laser (Spitfire, Spectra Physics) into a BBO crystal, and detected by a polychromator-CCD.

Transient absorption spectroscopy has been used to investigate the carrier dynamics in ZrN_x films.

Figure 5.1.1 (a), (b) are the transient absorption spectra of ZrN_x deposited at 500 ºC and 600 ºC at various time delays, showing the change in optical density, ΔOD, as a function of the probe wavelength in the visible range. For a pump-probe measurement, a positive signal represents excited state absorption while a negative ΔOD originates from bleaching of the ground state or stimulated emission in some cases. In ZrN_x samples we could not observe bleaching peaks in the detection range of 900 nm - 1500 nm.

In Figure 5.1.1 (a), t = -1 ps signifies the steady state when there is no laser excitation hence no change in optical density. At t = 0.06 ps positive peaks around 500 nm and 730 nm. Immediately after the pump pulse, the electron density is high. There could be higher probability of excitation from higher energy state than from ground state. It is interesting to note several peaks around 50 fs (limited by the time resolution of the system), probably represent the density of the states in ZrN_x. Similar to the metal and other π-electron system, the initial effective electron-electron scattering occurs in very short time scale [22, 23]. As the time progresses the TA spectra show positive peaks around 480 nm and 730 nm. By about t = 1.0 ps a stable distribution is formed which decays back to steady state at longer ps scale, as shown in Figure 5.1.1 and Figure 5.1.2. The excited state absorption peaks appear around 500 nm and 730 nm and peaks on these time scales suggests the ZrN_x samples deposited at these substrate temperatures contain many free electrons for absorption and thus there is effective electron-electron

scattering between these electrons. This observation suggests there is high density of free electrons in ZrN, similar to the metal. Also a stable carrier distribution can be established by an efficiently e-e scattering within a couple of hundred of fs.

In general, two important interaction mechanisms dominate the photo-excited carrier decay in an ultrafast measurement, i.e. electron–electron scattering and electron–phonon scattering [24-27]. The former e-e scattering is usually very fast within tens of femtoseconds, the carrier distribution is generally a non-equilibrium distribution, not a Fermi–Dirac distribution. The first e-e scattering usually result in the carrier distribution according to the electron density of states (DOS) of the material. Therefore, in such extremely short time within disappear of the pump pulse (<100 fs), the initial carrier distribution is a representative of the material DOS. TA spectra for ZrN exhibited two positive peaks located at 500 and 736 nm. No bleaching peaks were observed on this wavelength range.

Moreover, a decay time of the order of hundreds of picoseconds was found for the peaks. Two decay processes were observed in this sample. This suggested that at the first stage, carriers may be captured in a side valley where thermalisation is slow, while at longer times the carriers are returned from the side valley and decay at zone centre to the Fermi level.

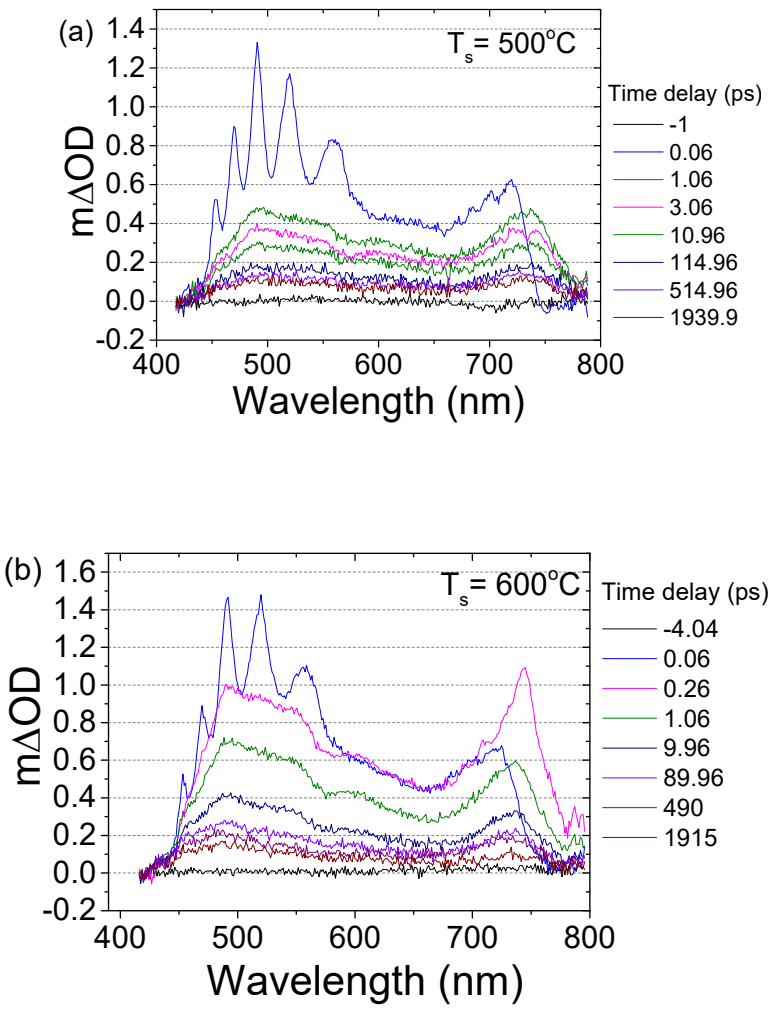

Figure 5.1.1 Transient absorption spectra of ZrN_x samples deposited at (a) 500 °C and (b) 600 °C on quartz substrate in visible range. The pump wavelength is 400 nm and I_{ex} = 600 μJ/cm^2

Figure 5.1.2 shows the time evolution of the ESA peaks at 730 nm after excitation for the ZrN_x samples deposited at 500 °C and 600 °C. Exponential fitting of the ΔOD for the ESA peaks indicates a decay constant of around 470 ± 84 ps and 605 ± 118 ps for the sample deposited at 500 °C and 600 °C respectively. In the excited states immediately after the pump laser, an ultrafast spike is observed as shown in the insets of Figure 5.1.2 (a) and (b), which is likely to correspond to the e-e scattering, limited by

the time resolution of the system, 250 fs. This process has a lifetime of the order of 100 fs [28]. The lifetime of this dynamic process observed in our experiments is around 400 fs. This ultrafast process represents e-e scattering occurring in the population in the excited states bringing the carrier population to thermal equilibrium as described by the Fermi-Dirac distribution at an elevated temperature. Ultrafast e-e scattering has usually been observed in metals, metal clusters as well as carbon based materials [29-31] where the free electrons or free π-electrons are present. This observation suggests there is high density of free electrons in ZrN_x, similar to metallic-like materials, consistent to the calculation and other measurements. Also a slowly changing carrier distribution can be established by such efficient e-e scattering within a couple of hundreds of fs. Using a single exponential function we can extract the decay time of the slow process. Table 5.1.1 tabulated the decay time at different wavelengths in visible and infrared regions for samples deposited at 500 ºC and 600 ºC.

The decay of the TA signal shows two distinct stages. One stage is shown in Figure 5.1.2, (a) electron-electron scattering occurs in one hundred fs and other stage is shown in Figure 5.1.2 (b) subsequently nanoseconds long decay is observed. The ultrafast decay is limited by the time resolution of the system of 150 fs. At times faster than 150 fs the ΔOD signal electron-electron scattering occurs. The similar process also occurs with a lifetime of tens to one hundreds of fs in semiconductors [8], metals [43,44] and metal clusters as well as carbon based materials [45,46] where free electrons or π-electrons contribute to the electron-electron scattering. A carrier distribution at an elevated temperature is established by such an efficient e-e scattering. The nanosecond long decay time can be attributed to thermalisation of excited states with the lattice via electron-phonon interactions. It is suggested the long decay time is a consequence of

restricted thermalisation pathways leading to carriers remaining in the valleys of high energy Zr 3d states. Figure 5.1.2 (a) shows the time evolution of the ESA peaks at 730 nm after excitation for the ZrN_x samples deposited at 500 ºC and 600 ºC in logarithmic scale to see better exponential fittings.

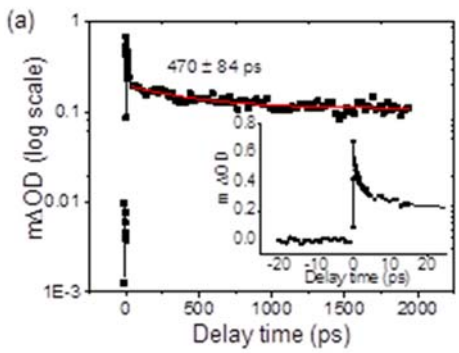

Figure 5.1.2 (a): Change in OD as a function of delay time measured at the 730 nm for samples deposited at a) 500 ºC, b) 600 ºC in logarithmic scale. Red curves are Exponential fits. Insets shows data in short time scale to highlight decay in this range.

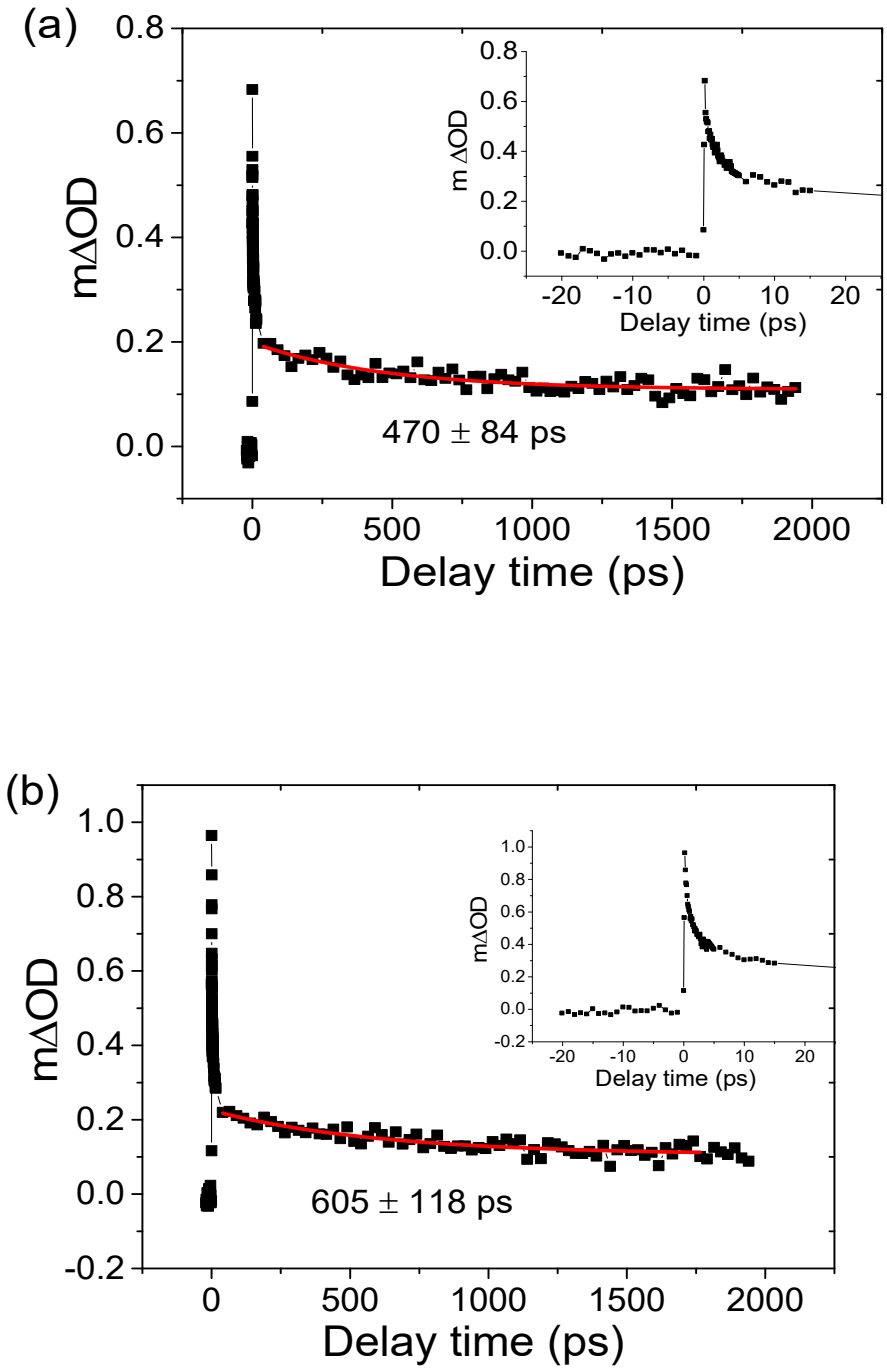

Figure 5.1.2: Change in OD as a function of delay time measured at the 730 nm for samples deposited at a) 500 ºC, b) 600 ºC. Red curves are Exponential fits. Insets shows data in short time scale to highlight decay in this range.

Figure 5.1.3 (a) and (b) show the transient absorption spectra in 900-1300 nm at various delay times. In this range, a positive band was observed for both samples. The near infrared signal from 900-1300 nm was studied to explore carrier dynamics of low energy excited states. It must be noted the near-infrared region measurements were pumped with a higher fluence than the measurements made in the visible region due to the higher noise levels. At an ultrafast pump-probe measurement, a high density of pump excites electron into the high energy level. Then the excited electrons can experience an effective e-e scattering if enough free electrons are available. The observed small peak with width of 200 fs suggests there are sufficient free electrons available in ZrN_x, implying ZrN_x metallic-like property, consistent to the observation in the visible region. After the short time of scattering, a stable carrier distribution, Fermi-Dirac distribution, forms relative to the density of states. They are positive and are independent of the probe wavelength within the measured wavelength range of 900 – 1200 nm. Spectrally the transient absorption signal remained positive. The wavelength independence of the carrier distribution in this region may be due to transitions between a very broad distributions of low excitation states thus a flat ΔOD response. This response is most likely from the free electron distribution near the Fermi surface of the material, as shown in steady state absorption. The signals after 0.2 ps were fitted to an exponential decay resulting in a decay time constant between 400 – 600 ps for probe wavelengths in the infrared region, tabulated in Table 5.1.1

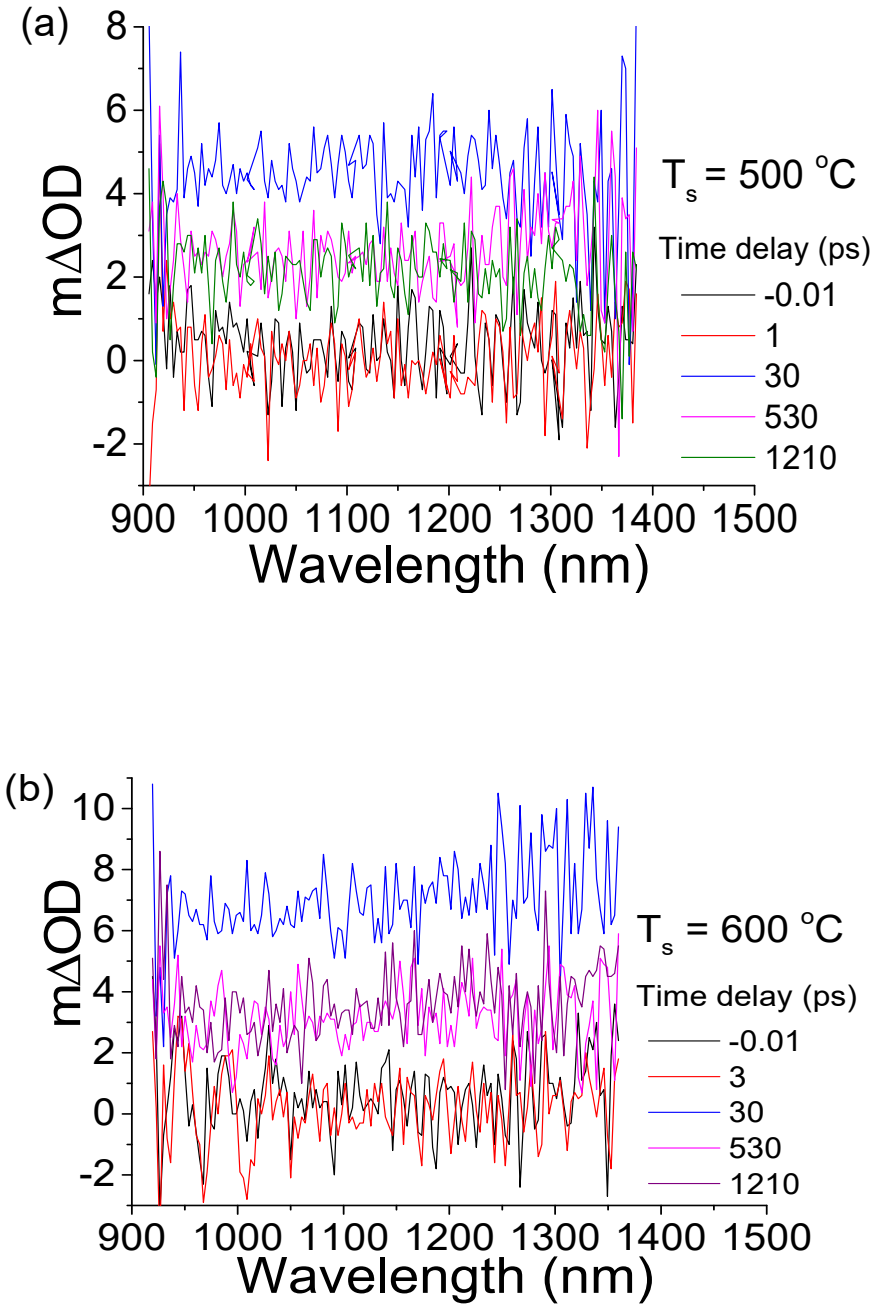

Figure 5.1.3 Ultrafast transient absorption spectrum in the near infrared regions showing positive delta OD after the pump of ZrN_x deposited at (a) 500 °C, and (b) 600 °C. TA spectrum is essentially flat in the 900-1350 nm range.

The observed decay times can potentially be ascribed to the electron cooling down to the lower states. In the general definition of hot carrier electron in semiconductors, the cooling time is attributed to the thermalization down to the edge of the conduction band. Here we do not have evidence about the band gap of ZrN_x and do not observed any negative TA band, which could be due to band edge bleaching. Hot carriers refers to carriers in the higher excited states, other than the conduction band edge or lowest excited state. The positive band in principle is ascribed to excited state absorption, and should be associated with excited states. For a positive TA signal, the decay time is dominated by the population of the lower state, and so essentially represents the decay time of the lower state. So, here we speculated if two or three observed positive bands originate from the same excited lower states, they in principle have a similar decay time (whilst of course, considering the errors). Otherwise, they should originate from at least one or more different excited states associated with the higher excited state, therefore, they could be considered to be hot carriers.

In the probe region, near infrared and visible, three positive bands were confirmed. To date, very little knowledge about the band structure is known in ZrN, it is difficult to assign specific transitions to the observed band. At longer time scales from several fs up to hundreds of picoseconds a stable linear-like distribution forms in the TA spectrum, from 450 - 750 nm. This oscillatory distribution takes 100s of ps to relax back to the steady state absorption levels. This kind of distribution of the TA spectrum may possibly be representative of the tail end of the Fermi-Dirac distribution of electrons described by an elevated temperature. Table 5.1.1 presents the time evolution of the change in optical density at 480 nm with exponential fitting obtaining a decay time constant of 412 ps at 500 ^{o}C and 512 ps at 600 ^{o}C. This decay time constant is

speculated to be representative of electron transitions at 480 nm. Upon excitation with the pump beam, optically allowed transitions from the excited (populated) states to higher excited states may exist in certain wavelength regions, and absorption of the probe pulse at these wavelengths will occur. Interestingly, a positive signal in the TA spectrum is observed in the wavelength region of excited-state absorption (Figure 5.1.1). Again, the intensity of the probe pulse is so weak that the excited-state population is not decreased appreciably by the excited-state absorption process.

TA measurements have shown features with long relaxation times of the ΔOD in the range of hundreds of picoseconds in the visible region and in the infrared region. The TA measurement shows that electrons with higher energy can be populated for a long time, which suggests it is possible to extract such higher temperature (dynamic energy) electrons with energy selective contacts and ZrN_x can be used toward the HC-SCs. Such long relaxation times on the order of hundreds of ps have not previously been observed in a bulk material using the TA technique.

Table 5.1.1: Decay time constant extracted by fitting exponential decay function using Lavenberg algorithm in TA spectrum.

Wavelength (nm)	**Decay time constant at T_s =500 °C**	**Decay time constant at T_s =600 °C**
480	412 ± 38 ps	512 ± 44 ps
570	366 ± 38 ps	402 ± 36 ps
730	470 ± 64 ps	605 ± 118 ps
Infrared wavelength		
950 nm	489 ± 218 ps	426 ± 152 ps
1050 nm	479 ± 123 ps	442 ± 119 ps
1250 nm	560 ± 218 ps	533 ± 198 ps

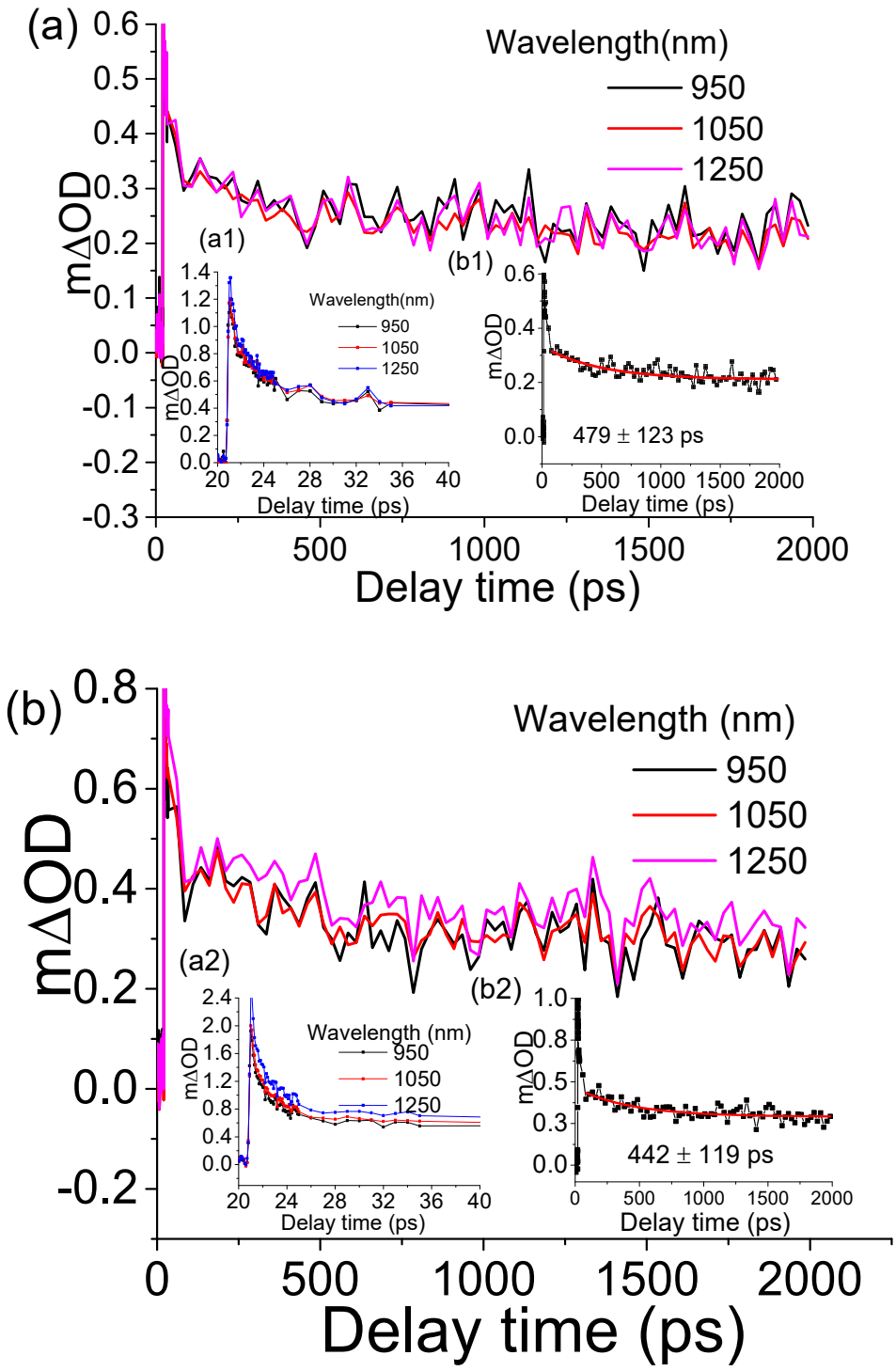

Figure 5.1.4: Time traces of transient absorption signals at several IR wavelengths for the films deposited at 500 °C and 600 °C. Inset (a1) and (a2) shows the transient on a shorter time scale. Insets (b1) and (b2) show the exponential fitting at 1050 nm for the film deposited at 500 °C and 600 °C respectively.

5.1.1. Theoretical investigation on carrier cooling time

Experimental results are further analysed theoretically by Hongze Xia using Density functional theory (DFT) in UNSW [1]. It has been assumed that the two important interaction mechanisms dominate the photoexcited carrier decay in an ultrafast measurement, i.e. electron–electron scattering and electron–phonon scattering [24]. The first one is usually very fast within tens of fs while the latter is a lot longer acting on picosecond to nanosecond timescales [32]. The theory finds the instantaneous carrier distribution at any moment after pumping using the measured data from the ultrafast TA spectra. It should be noted that the carrier distribution is generally a non-equilibrium distribution, not a Fermi–Dirac distribution. The carrier temperature of the non-equilibrium distribution is defined as in terms of the average carrier energy. This implies that the carrier temperature defined here is calculated by equating the total energy and particle number of a non-equilibrium carrier distribution to those of a Fermi–Dirac distribution at that temperature. This carrier temperature is an indicator of the average carrier energy, and qualitatively demonstrates how far the carrier population is excited away from the equilibrium distribution at room temperature. In metallic systems where electron density is high and carrier scattering is strong [33-36], the theory is simplified to only consider the electron density of states (DOS) of the material, and neglects the momentum information as it has been assumed that a phonon state is always available to assist with a specific transition. Under low injection, the carrier distribution is not changed much and the change is only relatively significant in the vicinity of the Fermi level where the slope of the Fermi distribution function is steep. At energy levels well below (or above) the Fermi level, the occupation is close to one (or

zero) and does not vary with the electron energy. So the change in those areas is minimal. The probe is a low intensity broad spectrum. So it is in the low injection condition. The total energy per unit cell is denoted as E_{tot} which reads

$E_{tot} = E_{in} + E_{off}$ E_{in} represents the input energy from the pump while E_{off} is the total energy per unit cell without excitation and can be expressed as:

$$E_{off} = \int_{-\infty}^{\infty} \xi . n_{off}(\xi) d\xi = \int_{-\infty}^{\infty} \xi .\ g(\xi).\ f_0(\xi, E_f^0, T_0) d\xi \quad \ldots\ldots(1)$$

Where $n_{off}\, d(\xi)$ is the carrier distribution in the dark expressed as $n_{off}(x) = n_o(x)\,(e^{qv/kt} - 1)$ while $gd(\xi)$ and $f_0(\xi)$ are the electron density of states (DOS) and the Fermi–Dirac distribution. E_f^0 and T_0 in function $f_0(\xi, E_f^0, T_0)$ indicate the initial Fermi level and carrier temperature ($T_0 = 300$ K) respectively.

An instantaneous carrier distribution exists at each moment after pumping and here we denote this quantity as $f_{on}(\xi)$. At any time, the number of electrons is conserved and reads:

$$N_{tot} = \int_{-\infty}^{\infty} g(\xi).\ f_{on}(\xi.t) d\xi \quad \ldots\ldots(2)$$

The total energy of the system at a given time can also be expressed as:

$$E_{tot}(t) = \int_{-\infty}^{\infty} g(\xi).\ f_{on}(\xi.t) d\xi \geq E_{off} \ldots\ldots(3)$$

Before estimating $f_{on}(\xi,t)$, the photon absorption in a material needs to be analysed. The absorption probability from state $\psi(\xi)$ to $\psi(\xi')$ excited by a photon $\hbar\omega$ can be estimated via Fermi's golden rule for a perturbing Hamiltonian H' :

$$W_{\xi-\xi'} = \frac{2\pi}{\hbar} <\psi(\xi)\, H'\psi(\xi)> 2\delta(\xi'-\xi-\hbar\omega)[(f(\xi;t)-f(\xi',t))] \ldots\ldots(4)$$

F(ξ,t) is either the instantaneous carrier distribution or the Fermi– Dirac distribution at equilibrium. The two f(ξ',t) in the last term of (4) denote the occupation probabilities at the initial and final energy levels, corresponding to the forward and reverse process of the transition. The absorption coefficient of a photon $\hbar\omega$ is proportional to the integral of W over the energy space and inversely proportional to the photon frequency [37]. In the calculation, It has been assumed that the matrix element <ψ(ξ)H'ψ(ξ)> in (4) is insensitive to the variation of ξ and also neglects the associated spontaneous emission. This is because for non-emissive materials, spontaneous emission is negligible. By merging all constants into one prefactor C, the absorption coefficient reads:

$$\alpha(\omega) = \frac{C}{\omega}\int_{-\infty}^{\infty}[f(\xi,t)-f(\xi+\hbar\omega),t)].J(\xi,\omega)d\omega$$

$$= \frac{C}{\omega}\int_{-\infty}^{\infty} f(\xi,t)\, J(\xi,\omega)d\xi - \frac{C}{\omega}\int_{-\infty}^{\infty} f(\xi,t)J(\xi-\hbar\omega,\omega)d\xi$$

$$= \frac{C}{\omega}\int_{-\infty}^{\infty} f(\xi,t)\,[J(\xi,\omega)- J(\xi-\hbar\omega,\omega)]d\xi \quad \ldots\ldots(6)$$

With

$$J(\xi,\omega) = [g(\xi)-.g(\xi+\hbar\omega)]^{1/2}$$

J(ξ,ω) is the approximate joint DOS at ξ while C contains information about the averaged matrix element for all possible transitions. Assuming the reflection of the sample is not affected by the pump, the transmission profile reads T(ω) = exp[(-α(ω)d][1-R(ω)] where d is the sample thickness and R is the reflection. This assumption is valid as the transient reflection measurements showed that the change of reflection is of the order 103 [36]. By comparing the transmission before and after pumping, the transient absorption spectrum is derived:

$$\frac{\Delta T}{T}(\omega) = \frac{e^{-\alpha d} - e^{-\alpha 0 d}}{e^{-\alpha 0 d}} \sim (\alpha_0 - \alpha)d \quad \ldots\ldots\ldots\ldots\ldots\ldots\ldots\ldots 7a$$

$$\Delta OD(\omega) = \log\left(\frac{T_o}{T}\right) = \log\left(\frac{e^{-\alpha 0 d}}{e^{-\alpha d}}\right) = -(\alpha_0 - \alpha)d \quad \ldots\ldots\ldots\ldots\ldots\ldots\ldots\ldots 7b$$

Now we have connected our theory with a TA experiment and by discretising (5) and (7), a set of linear equations can be constructed. We discretise the electron energy into N+1 levels with a constant energy step $\Delta\xi$ and the photon spectrum into N frequencies with the same level separation. The upper part of Eq. (8) results from the substitution of (5) into (7b) while the bottom part is the particle conservation constraint. By solving the (N+1) (Nx1) linear equations, the instantaneous carrier distribution f_{on} is obtained. We can define $f_{on} = f_{quasi} \times \Delta f$ where f_{quasi} is a Quasi Fermi–Dirac distribution at elevated temperature that reproduces the total energy and conserves the particle number (see Eq. (8)). The temperature that results from this Fermi–Dirac distribution can be regarded as the carrier temperature of f_{on}. Δf is simply the occupation fluctuation of f_{quasi}:

$$\int_{-\infty}^{\infty} \xi\, g(\xi).\, f_{on}(\xi, t)\, d\xi = \int_{-\infty}^{\infty} \xi.\, g(\xi).\, f_{quasi}(\xi, t)\, d\xi \quad \ldots\ldots\ldots\ldots\ldots\ldots\ldots\ldots (8a)$$

$$\int_{-\infty}^{\infty} g(\xi).\, f_{on}(\xi, t)\, d\xi = \int_{-\infty}^{\infty} g(\xi).\, f_{quasi}(\xi, t)\, d\xi \quad \ldots\ldots\ldots\ldots\ldots\ldots\ldots\ldots\ldots\ldots (8b)$$

Density functional theory (DFT) calculation was performed to obtain the DOS of rock salt ZrN. This simulation was done using 55 Hartree as the plane wave energy cutoff and a 12 x 12 x 12 k-grid for the self-consistent-field calculation. The Perdew–Burke-Ernzerhof exchange-correlation functional was adopted and a larger k-grid with a size of 20 x 20 x 20 was chosen for the DOS calculation. In order to obtain a highly accurate DOS, a tetrahedral method over a direct sum with Gaussian smearing was favoured. The calculation was performed by ABINIT using Fritz-Haber-Institute pseudo-potentials.

The band structures and the DOS of the two materials can be found in Chapter 4, Figure 4.1. The TA spectra of ZrN were analysed using the DOS obtained from DFT calculations [1]. Figure 5.1.5 shows that the measured TA spectra for ZrN_x deposited at 500 ^{o}C were reproduced by the dynamic theory. Using the proposed model, some new insights into the instantaneous carrier distribution as well as the quasi-Fermi Dirac distributions at elevated temperatures can be obtained. Plots (a) and (b) of Figure 5.1.5 show that the carrier distribution and the corresponding carrier occupation were altered slightly after the excitation. Most of the fluctuations were within 0.2 eV of the Fermi level and are responsible for the variation of optical density.

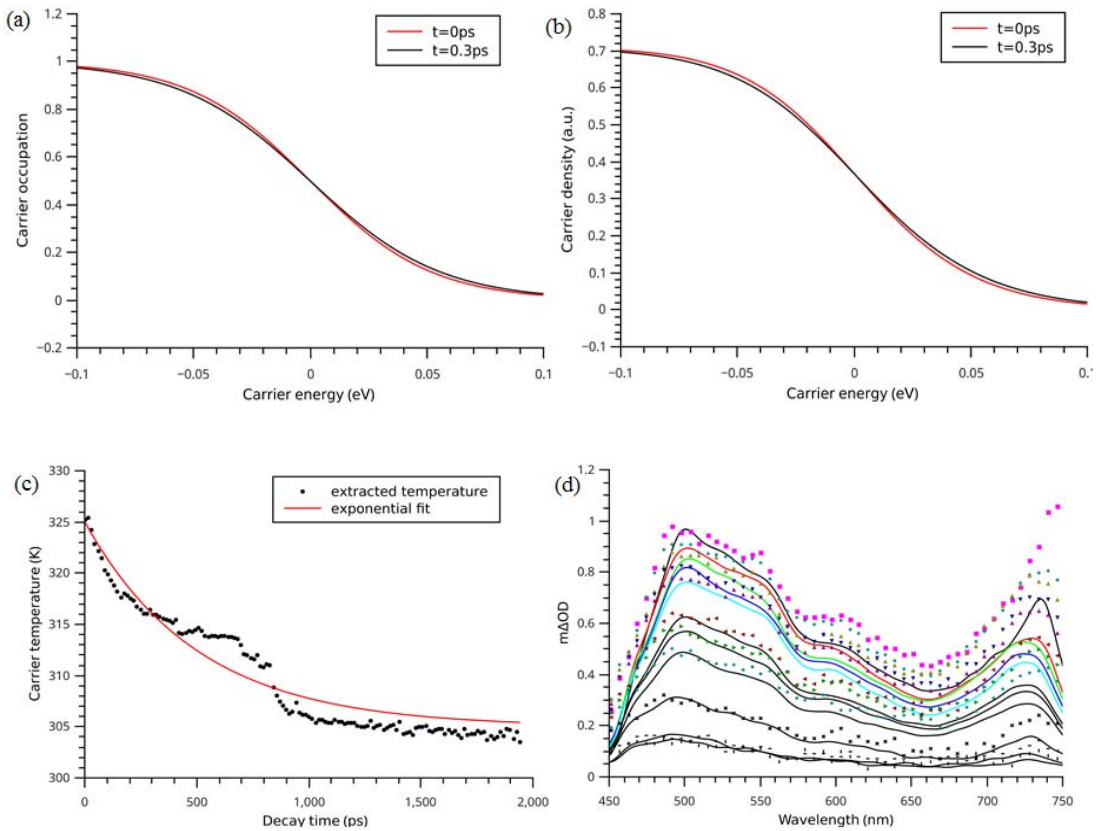

Figure 5.1.5: Simulation results for ZrN. (a) Quasi-Fermi Dirac distribution at t = 0.3 ps after excitation (T=323 K) and the equilibrium carrier distribution at 300 K. (b) The corresponding carrier density distribution. (c) The extracted carrier temperature from the quasi-Fermi Dirac distribution and the exponential fitting with a time constant of 0.50 ns. (d) The reproduced transition absorption spectra using the instantaneous distribution function f_{on}. In (d), the points are from the experiment, while the smooth curves are from the simulation [1].

TA spectra for ZrN exhibited two positive peaks located at 500 and 736 nm (see Figure 5.1.1). No bleaching peaks were observed on this wavelength range. Moreover, a decay time of the order of hundreds of picoseconds was found for the peaks. Hence, a lower carrier temperature was extracted and confirmed by the following analysis, as shown in Figure 5.1.5 (d). Two decay processes were observed in this sample. Initially, the carrier temperature increased to 325 K and then dropped to 315 K after a few hundred picoseconds. At about 750 ps, the carrier temperature entered a second decay and

quickly decreased to 305 K. This suggested that at the first stage, carriers may be captured in a side valley where thermalisation is slow, while at longer times the carriers are returned from the side valley and decay at zone centre to the Fermi level. The exponential decay is also shown in Figure 5.1.5(d) for a comparison against the standard theory, where the relaxation rate is generally characterised by a single time constant. However, this single exponential fit is phenomenological and given the complexities of electronic band structures, this simple exponential decay could not be expected to always represent the temperature of a hot carrier as it relaxes at ultra-fast timescales. Nonetheless it does represent carriers at elevated energies for relatively long periods.

5.1.2. Summary

ZrN_x films have been deposited on quartz and silicon substrates by sputtering of a Zr target in a mixed argon and nitrogen atmosphere. Chemical composition of the film from XPS study yields a (N+O)/Zr ratio of 1.7. The steady state optical study shows strong metal like absorption at high energies where transitions occur at wavelengths below 450 nm. Strong free carrier absorption is observed at wavelengths greater than 450 nm indicative of the metallic nature of the ZrN film at long wavelengths. In this chapter, the ultrafast relaxation of carriers in bulk ZrN thin films has been demonstrated by means of femtosecond pump-probe TA spectroscopy. TA results show excited state absorption peaks in visible region. In the near-infrared TA spectra, a positive band is observed. TA measurements have shown features with a long relaxation time of the ΔOD in the hundreds of picoseconds in the visible region and near-infrared region for both sample deposited at 500 ºC and 600 ºC. On the ultrafast time scale elastic electron-electron scattering occurs within several hundred fs then a transient carrier distribution is formed with decay times in the order of hundreds of picoseconds. The detected

lifetimes in the visible region are longer than in the near-infrared region. The electrons are populated for longer at these higher energy states than in lower excited states. The TA measurements are evidence for electrons at higher electronic states that can be colonized for a long time, which suggests the possibility to extract these electrons with high dynamic energy with the use of energy selective contacts in a hot carrier photovoltaic device. The long carrier lifetime and the metallic nature allowing absorption of a wide spectrum of light in ZrN and indicates it would be a promising material for use as an absorber for HCSCs.

Bibliography

1. Xia, H., et al., *Hot carrier dynamics in HfN and ZrN measured by transient absorption spectroscopy.* Solar Energy Materials and Solar Cells, 2016. **150**: p. 51-56.
2. Xiaoming, W., et al. *Ultrafast transient absorption study of hot carrier dynamics in hafnium nitride and zirconium nitride*. in *Photovoltaic Specialist Conference (PVSC), 2015 IEEE 42nd*. 2015.
3. Conibeer, G., et al., *Hot carrier solar cell absorber prerequisites and candidate material systems.* Solar Energy Materials and Solar Cells, 2015. **135**(0): p. 124-129.
4. Johansson, B.O., et al., *Higher nitrides of hafnium, zirconium, and titanium synthesized by dual ion beam deposition.* Journal of Materials Research, 1986. **1**(03): p. 442-451.
5. Keiichi, T., et al., *Properties of Superconducting ZrN Thin Films Deposited by dc Reactive Magnetron Sputtering.* Japanese Journal of Applied Physics, 1987. **26**(5A): p. L570.
6. Tung, H.-M., et al., *Hardness and residual stress in nanocrystalline ZrN films: Effect of bias voltage and heat treatment.* Materials Science and Engineering: A, 2009. **500**(1–2): p. 104-108.
7. Leu, L.C., et al., *Comparative study of ZrN and Zr–Ge–N thin films as diffusion barriers for Cu metallization on Si.* Journal of Vacuum Science & Technology B, 2008. **26**(5): p. 1723-1727.
8. Mei, A.B., et al., *Physical properties of epitaxial ZrN/MgO(001) layers grown by reactive magnetron sputtering.* Journal of Vacuum Science & Technology A, 2013. **31**(6): p. -.
9. Yanagisawa, H., et al., *Epitaxial growth of (111) ZrN thin films on (111) Si substrate by reactive sputtering and their surface morphologies.* Journal of Crystal Growth, 2006. **297**(1): p. 80-86.
10. Yanagisawa, H., et al., *Epitaxial growth of (001)ZrN thin films on (001)Si by low temperature process.* Japanese Journal of Applied Physics, Part 1: Regular Papers and Short Notes and Review Papers, 2005. **44**(1 A): p. 343-349.
11. Barnett, S.A., et al., *Epitaxial growth of ZrN on Si(100).* Applied Physics Letters, 1988. **53**(5): p. 400-402.
12. Saha, B., Acharya, Jagaran,Sands, Timothy D.,Waghmare, Umesh V., *Electronic structure, phonons, and thermal properties of ScN, ZrN, and HfN: A first-principles study.* Journal of Applied Physics, 2010. **107**(3).
13. Christensen, A.N., Dietrich, O. W.,Kress, W.,Teuchert, W. D., *Phonon anomalies in transition-metal nitrides: ZrN.* Physical Review B, 1979. **19**(11): p. 5699-5703.
14. Heid, R., et al., *Ab initio lattice dynamics and electron-phonon coupling in the refractory compounds ZrN and HfN.* Physical Review B, 2005. **71**(9): p. 092302.
15. Benia, H.M., et al., *Optical properties of non-stoichiometric sputtered zirconium nitride films.* Applied Surface Science, 2003. **211**(1–4): p. 146-155.
16. Signore, M.A., et al., *Zirconium nitride films deposited in sputtering atmosphere: Optical, structural, and electrical properties.* Journal of Vacuum Science & Technology A: Vacuum, Surfaces, and Films, 2011. **29**(6): p. 061507-061507-9.
17. Lamni, R., et al., *Optical and electronic properties of magnetron sputtered ZrNx thin films.* Thin Solid Films, 2004. **447–448**(0): p. 316-321.
18. Clady, R., et al., *Interplay between the hot phonon effect and intervalley scattering on the cooling rate of hot carriers in GaAs and InP.* Progress in Photovoltaics: Research and Applications, 2012. **20**(1): p. 82-92.

19. Wen, X., et al., *Ultrafast electron transfer in the nanocomposite of the graphene oxide-Au nanocluster with graphene oxide as a donor.* Journal of Materials Chemistry C, 2014. **2**(19): p. 3826-3834.
20. Pandey, A. and P. Guyot-Sionnest, *Slow Electron Cooling in Colloidal Quantum Dots.* Science, 2008. **322**(5903): p. 929-932.
21. Maity, P., T. Debnath, and H.N. Ghosh, *Slow Electron Cooling Dynamics Mediated by Electron–Hole Decoupling in Highly Luminescent CdSxSe1–x Alloy Quantum Dots.* The Journal of Physical Chemistry C, 2015. **119**(19): p. 10785-10792.
22. Hartland, G.V., *Ultrafast studies of single semiconductor and metal nanostructures through transient absorption microscopy.* Chemical Science, 2010. **1**(3): p. 303-309.
23. Sui, L., et al., *Ultrafast carrier dynamics of carbon nanodots in different pH environments.* Physical Chemistry Chemical Physics, 2016. **18**(5): p. 3838-3845.
24. Hartland, G.V., *Optical Studies of Dynamics in Noble Metal Nanostructures.* Chemical Reviews, 2011. **111**(6): p. 3858-3887.
25. Shah, J., *Ultrafast spectroscopy of semiconductors and semiconductor nanostructures*. Vol. 115. 2013: Springer Science & Business Media.
26. Alfano, R.R., *Semiconductors Probed by Ultrafast Laser Spectroscopy*. Vol. 2. 2012, New York: Elsevier.
27. Wen, X., *Ultrafast Spectroscopy: Principle and Applications in Semiconductor Nanostructures; VDM Publishing, 2007.* 2007: VDM publishing.
28. Nozik, A.J., et al., *Dependence of hot carrier luminescence on barrier thickness in GaAs/AlGaAs superlattices and multiple quantum wells.* Solid State Communications, 1990. **75**(4): p. 297-301.
29. Voisin, C., et al., *Ultrafast Electron Dynamics and Optical Nonlinearities in Metal Nanoparticles.* The Journal of Physical Chemistry B, 2001. **105**(12): p. 2264-2280.
30. Brida, D., et al., *Ultrafast collinear scattering and carrier multiplication in graphene.* Nat Commun, 2013. **4**.
31. Gierz, I., et al., *Snapshots of non-equilibrium Dirac carrier distributions in graphene.* Nat Mater, 2013. **12**(12): p. 1119-1124.
32. Bonn, M., et al., *Ultrafast electron dynamics at metal surfaces: Competition between electron-phonon coupling and hot-electron transport.* Physical Review B, 2000. **61**(2): p. 1101-1105.
33. Allen, P.B., *Theory of thermal relaxation of electrons in metals.* Physical Review Letters, 1987. **59**(13): p. 1460-1463.
34. Bejan, D. and G. Rąseev, *Nonequilibrium electron distribution in metals.* Physical Review B, 1997. **55**(7): p. 4250-4256.
35. Rethfeld, B., et al., *Ultrafast dynamics of nonequilibrium electrons in metals under femtosecond laser irradiation.* Physical Review B, 2002. **65**(21): p. 214303.
36. Sun, C.K., et al., *Femtosecond investigation of electron thermalization in gold.* Physical Review B, 1993. **48**(16): p. 12365-12368.
37. Feng, Y., et al., *Can Tauc plot extrapolation be used for direct-band-gap semiconductor nanocrystals?* Journal of Applied Physics, 2015. **117**(12): p. 125701.

Chapter 6

Discussion, Conclusion and Future Work

The purpose of this thesis was to synthesise and characterise the suitable absorber material for third generation photovoltaic- hot carrier solar cells. In pursuit of this aim, an in-depth study of the various group IV alloys and refractory metal nitrides has been carried out. Group IV alloy -Germanium carbide and refractory metal nitride – Zirconium nitride were fabricated using sputtering. The structural, compositional, optical, and phononic properties of the resulting Ge_xC_{1-x} *and* ZrN_x *films were examined and critically analysed with regards to the achievement of the above-mentioned aim. This chapter extracts the important principles that can be gleaned from the experimental work and details the novel contributions of this thesis, leading to recommendations for future research.*

Introduction

This chapter has the aim of bringing the contents studied in the thesis into a single broad picture, finding an absorber material to implement real HC-SC. In particular the first part of the chapter is devoted to the summarising all the important results related with fabrication and characterization of GeC and ZrN as a hot carrier absorber material. The second part of the chapter is dedicated to the discussion related with the suitability of GeC and ZrN as an absorber for HC-SC. Subsequently, result of the ZrN films (deposited using RF sputtering) from the ultrafast transient absorption measurement has been discussed to investigate the carrier cooling properties of ZrN. In the last part of the chapter, all the original contribution of this thesis has been listed along with some recommendation for future research related with the implementation of HC-SC.

6.1 Summary

6.1.1. Study of GeC as an absorber for a HC-SC

Germanium carbide- group IV alloy is quite attractive as a hot carrier absorber material because of the calculated wide phononic band gap. The large mass difference between its constituent elements makes it suitable for suppressing carrier cooling which is one of the pre-requisites for a hot carrier absorber material. Furthermore, the elements of GeC alloy are reasonably abundant to implement low cost solar cells. However, due to the low solubility, it is quite challenging to fabricate stoichiometric and stable GeC film. Nevertheless, the widely used RF sputtering method was employed to fabricate Ge_xC_{1-x} films in Chapter 3. The challenging growth of nano-crystalline GeC using an industry-friendly process called sputtering has been demonstrated for the first time in UNSW SPREE laboratory. Nano-crystalline Ge_xC_{1-x} is a potential third generation solar cell absorber material due to its favourable optoelectronic properties and relatively high abundance of elements. The ability to grow nano-crystalline Ge_xC_{1-x} in large areas by an industry-friendly process can enhance its scope as a photovoltaic absorber. In Section 3.1 of Chapter 3, Ge_xC_{1-x} nano-crystalline films were grown on Si (100) substrates by RF magnetron co-sputtering using graphite target with Ge strips on it. The coverage area of Ge strips were 40 %. The sputtered Ge_xC_{1-x} film has a smooth surface with a root mean square roughness of about 4 nm. XPS results indicated the carbide formation and the presence of Ge-C bonding for the samples grown at 350 ^{o}C, 50 W with 0.9 eV bandgap estimated using the Tauc equation. TEM imaging shows the formation of nanocrystals with lattice spacing of 5.53 Å which is consistent with the GeC lattice constant published elsewhere. The lattice constant value was also determined using a numerical model. With the help of Quantum Espresso, Self-consistent-field (SCF)

calculations were performed on the postulated system within the framework of Density Functional Theorem (DFT). The lattice constant estimated using numerical model was 5.34 +/- 0.5 Å which matched well with our TEM measurement. The Raman signature of the local Ge–C mode is identified near 530 cm^{-1} in Ge_xC_{1-x} film grown at 350 ºC. At this growth condition, a maximum value for x = 15.5 % is found for Ge_xC_{1-x} by fitting XPS spectra.

In Section 3.2, all Ge_xC_{1-x} films were deposited with Ge target and methane gas using reactive sputtering to observe the effect of RF powers and the T_s on deposited films. All the films deposited with reactive sputtering were found amorphous in nature with a lot of hydrocarbon on the surface. It could be due to the carbon poisoning of the Ge target. Less than 1 % oxygen was found in all the Ge_xC_{1-x} samples after 60 seconds Ar+ etching. The effects of the T_s on the yield of GeC for the samples deposited at different temperatures were analysed in detail in Section 3.2.1 of Chapter 3. The a-Ge_xC_{1-x} with GeC content up to 21 % has been fabricated with 50 W RF power at 250 ºC by reactive sputtering methods. This is the maximum percentage of Ge-C bond has been introduced in the film so far in spite of having low solubility between the elements. The GeC percentage by volume was found to first increases and then decreases with increasing T_s. The introduction of C into the Ge matrix seems to tune the optical bandgap over a wide range from 2.7 eV to 1.0 eV with decreasing carbon concentration in the films. Section 3.2.2 of Chapter 3 discussed the effect of different RF power (40 W to 80 W) on the deposited Ge_xC_{1-x} film keeping the T_s at 250 ºC. Study suggested that the low RF power around 50 W is favourable to fabricate Ge-C bond. It has been observed from XPS result that the high RF power above 50 W decreases the Ge-C content in the film drastically due to the increase in the total germanium content in the film.

6.1.2. Study of Zirconium Nitride as an absorber material

Recently refractory metal nitride such as ZrN have gained attention as a hot carrier absorber material for HC-SC due to a large mass difference between the constituent elements. It has the potential to slow down the carrier thermalization due to its interesting phononic properties which make it a promising candidate for HC-SC. A thin film of ZrN has been grown using two types of sputter system. One is single target sputter machine and another one is an AJA tool. One of the advantages of the AJA over the home built system is that it has a load lock and ultra-high vacuum system. Films deposited using RF reactive sputtering in the single target system were found to be polycrystalline at a T_s of 350 ºC, 100 W. Zr-rich ZrN_x films were deposited with considerable amount of oxygen around 20 % using XPS measurement, whereas, at T_s > 500 ºC, ZrO_xN_y was more favoured. It could be due to the stronger affinity of Zr towards oxygen. ZrN_x film was smooth and dense at T_s of 500 ºC and 600 ºC as confirmed by AFM with RMS roughness of 1.71 nm and 1.87 nm for the films grown at 500 ºC and 600 ºC respectively. Absorption calculation from UV-Vis spectrometer shows the transition point for the film deposited at 500 ºC and 600 ºC near to 530 nm.

Epitaxial growth of ZrN film has been carried out using DC reactive sputtering (AJA sputter) for the first time in UNSW. Single Zr target along with a mixture of Nitrogen and Argon gas have been used to synthesise ZrN. The epitaxial growth of ZrN with 5% of N_2 gas at 500 ºC has been confirmed by XRD and X-ray pole figure using Phi scan. TEM scan is also used to further substantiate the epitaxial growth of ZrN film. The calculated lattice constant of 0.457 nm of the deposited epitaxial ZrN film is in close agreement with bulk ZrN. An absence of second order phononic modes provide complementary evidence for the epitaxial growth. Unfortunately, ultrafast transient

absorption measurement has not been observed because of high reflectivity and low transmission, because of its metallic nature, but neither of which prevent its use as a hot carrier absorber. Properties of ZrN film have been further investigated after annealing at the high temperature of 730 ºC in N_2 only atmosphere using an MTI furnace. The film tends to lose ZrN phase in both XRD and Raman due to the introduction of ZrO_2 bond formation in all the annealed samples. It is because of the strong affinity of Zr metal towards oxygen.

6.1.3. Ultrafast Transient absorption measurement

ZrO_xN_y thin film deposited using RF sputtering method have been used to study the transient absorption measurement. ZrN_x sample deposited at T_s = 350 ºC did not show any TA signal. It could be due the low transmission due to the thick sample. The ultrafast relaxation of carriers in bulk thin films deposited at higher T_s > 500 ºC by means of femtosecond pump-probe transient absorption (TA) spectroscopy has been observed. TA spectra of deposited film show excited state absorption peaks at shorter wavelength of 480 nm and a longer wavelength of 730 nm, in the visible region. In the near-infrared TA spectra, a positive band of excited state absorption is observed. TA measurements have shown features with a long relaxation time of the ΔOD in the hundreds of picoseconds in the visible region and near-infrared region. On the ultrafast time scale elastic electron-electron scattering occurs within several hundred of femtoseconds then a transient carrier distribution is formed with decay times in the order of hundreds of picoseconds. The detected lifetimes in the visible region at wavelength 730 nm (605 ± 118ps) are longer than in the near-infrared region at 1050 nm (442 ± 119 ps) for the film deposited at 600 ºC. Indicating that the electron states are populated for longer at (730 nm) higher energy states than in (480 nm) lower excited

states. The TA measurements evidently show the electrons at higher electronic states can be colonized for a long time of the order of 605 ± 118 ps, which suggests the potential to extract these electrons with high dynamic energy with the use of energy selective contacts such as Al_2O_3/ Ge QW / Al_2O_3 in a hot carrier photovoltaic device. The long carrier lifetime and the metallic nature, allowing absorption of a wide spectrum of light in deposited film, indicates it to be a promising material for use as an absorber for HCSCs.

6.2 Discussion

In the first five chapters of this thesis, some of the main scientific and technological aspects related to the fabrication and characterization of a HCSC absorbers have been analysed. It is already been known that to implement HCSC, absorber and ESC are required. Moreover, absorber and ESCs are highly correlated in terms of physical and electrical properties. The characteristics of absorber material determine the requirement of ESCs structured and vice versa, thus the design of a HCSC has to be seen as a single task, where the properties and structures of the different components have to be engineered simultaneously.

Different group IV alloys (GeC, SnC etc), and transition metal nitrides (ZrN, HfN) are recently grabbing attention as a hot carrier absorber material. However, this thesis mainly focus on study of group IV alloy-GeC and transition metal nitride-ZrN as an absorber material for HC-SC. Both materials have a large phononic bandgap, proved theoretically and experimentally, which is one of the requisite for the absorber material is to prevents Klemens mechanism and hence slow down the carrier cooling, discussed in Chapter 2. To investigate the suitability of GeC as an absorber, firstly, germanium

carbide has been deposited using RF sputtering method with two techniques (Co-sputtering and RF sputtering) as discussed in Chapter 3. Although, we have fabricated nanocrystalline Ge_xC_{1-x} with 15.5 % of Ge-C bond using co-sputtering method, yet carrier cooling properties still unknown. Slow carrier cooling is one of the essential requirement of the absorber material in addition to large phononic band gap. In addition, deposition of stable GeC is very challenging due to the thermodynamic instability and low solubility of carbon in germanium. It is therefore too early to say GeC as a promising absorber for HC-SC before knowing carrier cooling properties. However, Ge_xC_{1-x} film deposited could be used in various photovoltaic application such as optoelectronics.

ZrN is a quite stable compound as compared to GeC and has large phononic bandgap. Therefore, ZrN films has been deposited to explore its suitability for HC-SC as an absorber. One of the main problem here is the affinity of Zr metal towards oxygen compared to nitrogen. All the films deposited $T_s > 500$ °C from a single target RF sputter seems to be suitable as an absorber for HC-SC. Apart from structural, compositional and optical measurement, they showed interesting transient absorption results. TA spectra of deposited film show two excited state absorption peaks at shorter wavelength of 480 nm and a longer wavelength of 730 nm, in the visible region (400 - 800 nm), and a positive band of excited state absorption in near Infrared region (900-1350 nm). Measurements have shown features with a long relaxation time of the ΔOD in the hundreds of picoseconds in the range of 400 - 600 ps in the visible and near-infrared region. The detected lifetimes in the visible region is comparably longer than in the near-infrared region. The electrons are populated for longer at these higher energy states than in lower excited states. These TA measurements evidently show the

electrons at higher electronic states can be populated for a long time, which suggests the possibility to extract these electrons with high dynamic energy with the use of energy selective contacts in a hot carrier photovoltaic device. The long carrier lifetime of the order of 600 ps is observed and the metallic nature allowing absorption of a large spectrum of light in ZrO_xN_y imparts it to be a promising material for use as an absorber for HCSCs. It also indicate that these lifetimes are significantly longer than those for materials without a large phonon gap such as gold and silver. For the first time we present evidence of such a long lifetimes of hot carriers observed in zirconium oxinitride. It is proposed that the long hot carrier lifetimes are due to restricted phonon decay pathways in zirconium oxinitride. It is envisaged that the long hot carrier lifetime in the bulk zirconium oxinitride film would provide a simpler route to devices designed to utilise hot carriers efficiently.

Epitaxial growth of ZrN at T_s = 500 ºC, detailed in Chapter 5 of the thesis, is one of the significant result has been demonstrated via DC sputtering using AJA load lock chamber. ZrN has been fabricated on MgO substrate. MgO and ZrN are better lattice mismatch with 8 % compared to 16 % with Si substrate. Therefore, it is possible to grow epitaxial ZrN on MgO. Epitaxial nature of the film was confirmed using HR-XRD, phi scan, pole figure analysis and TEM measurement. Even though we have achieved the epitaxial growth of ZrN, unfortunately, we could not get any signal from TA measurement. The fact that the film is too thick so it allows negligible transmission. But, absorbant for TA is not a problem with the material, just with the TA technique. It might actually be very useful indeed as a hot carrier absorber if there is some other method to measure carrier cooling property.

In addition, HC-SC could be implemented using epitaxial ZrN as an absorber with ESC structure i.e Al_2O_3 / Ge QW / Al_2O_3 or Al_2O_3 / Si QW / Al_2O_3 to realise a real solar cell.

In conclusion, this thesis investigated some of the basic aspects related to the fabrication and characterization of an absorber material for HC-SC. The aim of the work was to seek materials in order to achieve actual progress towards the fabrication of the device. Results have been obtained from the deposited GeC and ZrN films, in addition a potential absorber material for HC-SC has been presented. However, this thesis is still to be considered as a preliminary step towards the realization of a HC-SC, since this task still faces great scientific and technological challenges. Much room exists for further investigation of nanostructured or bulk material absorbers, both in Group IV alloys and transition metal nitrides, in order to obtain slower hot carrier cooling behaviours. Findings of this work have to be considered as a preliminary insight for the development of the HC-SC Further research is needed in order to accomplish the successful realization of an actual device.

What's the difference between the DC and RF magnetron sputtering in preparing the GeC and ZrN films? Why the different methods used to prepare the GeC and ZrN films?

Table 6.2.1: List of parameters and methods used in the fabrication of GeC and ZrN

Process parameters	**GeC**	**ZrN**	**ZrN**
Sputter method	RF	RF	DC (AJA sputter ultrahigh vacuum)
Substrate temperature	RT-600 ºC	RT – 600 ºC	
RF power	40-100 W	100 W	
DC power	-	-	50 W and 100 W

Table 6.2.1 list the parameters and methods used to fabricate the GeC and ZrN in the lab. The following point explains why different methods used to fabricate ZrN and GeC films.

- GeC has been deposited using RF sputtering method. After literature survey, co-sputtering and reactive sputtering seem to be suitable method to fabricate GeC.
- ZrN films have been deposited using RF sputtering method but there was considerable amount of oxygen found in the samples. It could be due to the tendency of ZrN to get oxidise easily as it exposes to atmosphere. Whereas, ZrN deposited using DC sputtering in AJA sputter machine reduce the amount of oxygen and favours epitaxial growth of ZrN.
- DC power (100 W and 50 W) were used to fabricate ZrN film while RF power was varied from 40 W to 100 W in case of GeC.
- Different sputter machines were used to deposit GeC and ZrN. ZrN deposited using DC sputtering with AJA sputter with load lock chamber while GeC deposited using RF sputtering in the home built sputter machine.

6.3 Novelty of the Thesis

This thesis contained a number of original contributions:

- Nano-crystalline germanium carbide has been fabricated using the industry-friendly process of sputtering for the first time for photovoltaic applications, with process details presented in this thesis, Chapter 3. Maximum 15.5% of Ge-C bond was found using XPS fitting method
- Fabrication and analysis of amorphous germanium carbide film to calculate the content of actual Ge-C bonds in the film. Maximum 21 % of Ge-C bond

is found in our samples deposited at 250 ºC, 50 W using RF reactive sputtering.

- Epitaxial Growth of ZrN using DC sputter at 500 ºC is one of the significant work and provides essential properties of cubic ZrN deposited on MgO substrate.
- Post annealing on DC sputtered ZrN film have been performed to investigate the effect on deposited film. ZrN phase lost when annealed at 730 ºC in N_2 gas ambient.
- Ultrafast carrier transient absorption measurement has been performed on RF sputtered ZrN_x films. Measurements have shown features with a long relaxation time of the change in optical density in the hundreds of picoseconds in the visible and near-infrared regions.

6.4 Recommendations for Future Research

- Single crystal Zirconium Nitride using DC sputtering needs further investigation to study carrier relaxation.
    - This can be achieved either by optimising ZrN film thickness.
    - And/or by developing another means of carrier cooling rate measurement – perhaps by construction of a full hot carrier cell.
- Atomic layer deposition method could be considered apart from sputtering to deposit ZrN film.
- Phononic properties of ZrON need investigation to understand carrier cooling property clearly.

Appendix A Typical Ge_xC_{1-x} samples processing parameters

A.1 Substrates cleaning procedure prior to deposition

Piranha Etch is used to remove most organic matter. It is highly exothermic and is a strong oxidizer thereby making the substrate surfaces highly hydrophilic. Appropriate personal protective equipment must be worn – including lab coats, safety goggles, gloves, and face mask. Piranhas etch gives off a gaseous by-product upon mixing therefore this reaction must take place in a fume cupboard. Glass – beakers and holders must be used during reaction. H_2O_2 is always ADDED TO H_2SO_4 .The Si and quartz substrates were cleaned using standard wet chemistry cleaning procedures, piranha (1:1= H_2SO_4:H_2O_2) and rinsed in deionised water before and after chemical cleaning. The native oxide of Si wafers was removed by diluted HF (10%) before wafers were immediately transferred into the chamber of the sputtering system.

A.2 Sputtering System

A home built RF magnetron sputtering system used in deposition of Ge_xC_{1-x}. In principle, sputtering is a PVD technique. The deposition process involves the creation of gas plasma that is usually an inert gas such as argon (Ar) by applying a voltage between a cathode and an anode. The produced argon ions (Ar+), which are accelerated toward the target, strike the target with such force that it ejects a very small part of the target material toward the substrate. As a result, a coating composed of atoms from the sputtered target will be gradually grown. The RF excitation mode is much more effective compared to the direct current (DC) mode, and is suitable for both conducting and insulating targets. The system used consists of a sputter chamber, a vacuum

pumping system and gas delivery system. In the sputter chamber, target of 100 mm diameter is installed on the water-cooled cathode, which houses permanent magnets for directing charged particles. The RF power is supplied by a RF generator operating at a frequency of 13.56 MHz, which is connected to the cathode through an impedance matching network with variable capacitors. The manual controls allow operators to tune capacitors to reduce the RF reverse power to about zero. 600 ºC and 100 W is the maximum possible substrate temperature and RF power, respectively for the home built system used.

A.3 Conditions of Ge_xC_{1-x} deposition

Ge_xC_{1-x} films have been deposited on Si (100) and Quartz substrates .The films were deposited using RF reactive sputtering with Ge target (99.9999% purity) and CH_4 gas and co-sputtering using graphite target and p-type germanium strips.

Process	**Parameters**	**Value**
Reactive Sputtering (Graphite target (99.999% pure) + CH_4 gas)	Substrate temperature T_s (ºC)	RT-600ºC
	RF power(W)	40-100 W
	CH_4 pressure (Pa)	0.01-0.08 Pa
	Total gas (Ar + CH_4) pressure (pa)	0.1
Co-sputtering (Graphite target (99.999% +germanium strips)	Substrate temperature T_{sub} (ºC)	300-550 ºC
	RF power(W)	100
	Total gas pressure (pa)	0.1
	Area covered by Ge strips (%)	20-40

Appendix B Typical ZrN_x samples processing parameters

B.1 Substrates cleaning procedure prior to deposition

Piranha process: It has been explained in appendix A.1.

RCA 1 and 2: RCA 1 and 2 has been used to clean substrates for ZrN_x film deposited using DC sputter. The Quartz and Si substrates were cleaned prior to each deposition using the RCA (Radio Corporation of America) sequence: wet cleaning procedure which is RCA1 (H_2O:NH_4OH:H_2O_2 = 5:1:1) at 75 °C to remove organic residues and RCA2 (H_2O: HCl: H_2O_2 = 5:1:1) at 75 °C to remove metals and reduce particulates.

MgO (SSP and DSP) substrates are cleaned and degreased by successive rinses in ultrasonic baths of trichloroethane, acetone, methanol, and deionized water, and then blown dry in dry N_2.

B.2 Sputtering System

Please refer section A.2 for sputter system explanation. Deposition of ZrN_x were carried out radio frequency (RF) magnetron (home built sputter) and DC sputtering (AJA International ATC-2200) on silicon, quartz and MgO substrates. The RF (13.56MHz) or DC suppliers were connected to Zr (4 in., 99.999%) targets. The base pressure was ~5.0 $\times 10^{-7}$ torr and the total gas pressure during film deposition was 0.1 Pa with argon (Ar + N_2), unless stated specifically. The Zr sputter rate was fixed by RF 100 W power.

B.3 Conditions of ZrN_x deposition

ZrN_x films have been deposited on Si (100) ,Quartz and MgO substrates .The films were deposited using RF reactive and DC sputtering with Zr target (99.9999% purity) and N_2 gas .

Process	Parameters	Value
RF Reactive Sputtering (Zirconium target (99.999% pure) + N2 gas)	Substrate temperature T_s (ºC)	RT-600ºC
	RF power (W)	100
	Ratio of nitrogen to argon	5-100
	Total gas pressure (pa)	0.1
DC Sputtering (AJA)	T_s	500 ºC
	DC power (W)	100
	Ar+ N_2 gas flow rate (sccm)	7 sccm
	Nitrogen	3-7%
	Total gas pressure (pa)	0.1

Appendix C Sample characterising techniques and operating conditions

C.1 Structural properties

C.1.1 Glancing incidence X-ray diffraction

Glancing incidence X-ray diffraction (GIXRD) (Philips X'Pert Pro) and using Emperyn with CuKα(λ=1.5406 Å) radiation was performed to study the phase and crystalline properties of the samples. GIXRD was operated at a voltage of 45 kV and a current of 40 mA and using a 1/8º divergent slit for all ZrN_x samples and 1/16 for all Ge_xC1-x films , a parallel plate collimator of 0.27º acceptance and a soller slit of 0.04 rad aperture. 2θ scan at glancing angle of ω= 2°was carried out for sample films on a wafer piece. Normal XRD was carried out for the ZrN samples deposited on MgO substrates.

C.1.2 Raman Spectroscopy

Raman spectroscopy was carried out using Reinshaw inVia Raman microscope of 514nm with argon ion laser power of 2.5 mW (1800l/mm grating) used with 10 times accumulation to reduce the laser power induced peak modification.

C.1.3 Transmission electron microscopy and specimen preparation

The structure of the NCs was observed by transmission electron microscope (TEM) (Philips CM200 and CM300). The TEM specimen was prepared by ion-beam milling and the small angle cleavage technique (SACT) for the cross-sectional and plan-view observations. The expected specimen thickness was less than 100 nm for the ion-beam milled and less than 50 nm for the SACT.

C.1.4 Atomic Force Microscopy

Atomic force microscopy (AFM) is a powerful tool which is widely used for studying the surface roughness of thin and thick films in coatings. The Bruker BioScope Catalyst™ Atomic Force Microscope (AFM) system used. The growth of films was found to accord with a three-dimensional island-like mechanism with low roughness (root-mean-square roughness <10 nm).

C.2 Compositional analysis

C.2.1 X-ray photoelectron spectroscopy

For the compositional analysis, X-ray photoelectron spectroscopy (XPS) (Fisons ESCALAB 220i-XL) with a monochromatic Al Kα (1486.5 eV) X-ray source and a hemispherical energy analyser detected the elements consisting of the film and

quantified their contents. The X-ray source power was 10 kV × 12 mA, with an analysed sample area of ~0.3 mm^2. With an etching rate of 0.2 nm/sec, approximately 10-15 nm of the top layer including the surface contaminants were removed prior to the measurement.

C.3 Optical properties

C.3.1 Spectrophotometer

A spectrophotometer (PerkinElmer) measured optical transmission and reflection values over the range UV-Vis-IR with the transmission reflectance accessory unless stated specifically.

C.3.2 Ultrafast transient absorption spectroscopy

Transient-absorption spectroscopy, also known as flash spectroscopy, is an extension of absorption spectroscopy. Here, the absorbance at a particular wavelength or range of wavelengths of a sample is measured as a function of time after excitation by a flash of light. In a typical experiment, both the light for excitation ('pump') and the light for measuring the absorbance ('probe') are generated by a pulsed laser. If the process under study is slow, then the time resolution can be obtained with a continuous (i.e., not pulsed) probe beam and repeated conventional spectrophotometric techniques.

A transient absorption experiment proceeds as follows: the time delay between excitation and probe beams is fixed. Before reaching the sample, the excitation beam (that delivers a pulse every 1 ms) passes through a mechanical chopper that is synchronized to the amplifier in such a way that every other excitation pulse is blocked. Thus, alternately the sample is being excited and not excited. Consequently, the white-light continuum that is incident on the detector diode array alternately corresponds to a

"pumped" and "unpumped" sample, and the detector alternately measures the intensity of the probe beam of a "pumped" and "unpumped" sample, $I(\lambda)_{pumped}$ and $I(\lambda)_{unpumped}$. $I(\lambda)_{pumped}$ and $I(\lambda)_{unpumped}$ are stored in separate buffers (while keeping the time delay between pump and probe fixed), and a number of shots that is sufficient for an acceptable signal-to-noise ratio is measured, usually 10^3–10^4. With the shot-to-shot detection capability of the multichannel detection system, particular spectra that deviate from the average ("outliers") can in real time be rejected during data collection, significantly improving signal-to-noise ratio. A second white-light beam (the reference beam) not overlapping with the pump pulse can also be used to further increase the signal-to-noise ratio. From the averaged values of $I(\lambda)_{pumped}$ and $I(\lambda)_{unpumped}$, an absorbance difference spectrum $\Delta A(\lambda)$ is constructed according to

$$\Delta A\,(\lambda) = -\log(I(\lambda)_{pumped}/I(\lambda)_{unpumped}$$

Then, the delay line is moved to another time delay between pump and probe, and the above procedure is repeated. In total, absorbance difference spectra at approximately 100–200 time points between 0 fs and ~5 ns are collected, along with absorbance difference spectra before time zero to determine the baseline. In addition, many spectra are collected around the time that pump and probe pulse overlap in time ("zero delay") to enable accurate recording of the instrument response function. This whole procedure is repeated several times to test reproducibility, sample stability, and long-term fluctuations of the laser system. In this way, an entire dataset $\Delta A(\lambda,t)$ is collected.

Table C1: Summary of growth and characterization techniques of thin-films used in this thesis

Properties	**Characterization technique**
Thickness	Dektak Profilometer ,X-Ray Reflectivity measurement
Resistivity	Four Point probe
Structural Properties	X-ray diffraction (XRD) spectroscopy
	Raman spectroscopy
	Transmission electron microscopy (TEM)
Optical properties	Spectrophotometry,
Topography	Atomic Force Microscopy (AFM)
Element identification and composition	X-ray photoelectron spectroscopy (XPS)
Phononic Properties	TRPL measurement, Ultrafast Transient absorption measurement (UTA)

Appendix-D List of publications

Patent:

Provisional: ZrN_x /HfN_x based solar cells

Journal papers

N. Gupta, B.P. Veettil, H. Xia, S.K. Karuturi, G. Conibeer, S. Shrestha, Synthesis of nano-crystalline germanium carbide using radio frequency magnetron sputtering, Thin Solid Films, 592, Part A (2015) 162-166.

N. Gupta, B.P. Veettil, G. Conibeer, S. Shrestha, "Effect of substrate temperature and radio frequency power on compositional, structural and optical properties of amorphous germanium carbide films deposited using sputtering". Journal of Non-crystalline Solids.

Neeti Gupta, Yu Wang, Yuanxun Liao, Simon Chung, Gavin Conibeer and Santosh Shrestha,'' Epitaxial Growth of ZrN (100) / MgO (100) using DC sputtering" submitted to Journal of Crystal growth. Under revision.

Simon Chung, Xiaoming Wen, Yu Feng, Shujuan Huang, **Neeti Gupta,** Gavin Conibeer, Santosh Shrestha, Takaaki Harada, Tak W. Kee, and Pyng Yu '' Nanosecond long hot carrier lifetimes observed in hafnium nitride'' submitted to Journal of Solar energy materials and Solar Cells

Santosh Shrestha, **Neeti Gupta**, Simon Chung, Hongze Xia, Gavin Conibeer "Hot Carrier solar cells: Toward the fabrication of practical absorbers", 7th ICMAT 2013, Suntec Singapore. International Journal of Nanotechnology.

Simon Chung, Xiaoming Wen, Yu Feng, Shujuan Huang, **Neeti Gupta,** Gavin Conibeer, Santosh Shrestha,''Nanosecond long hot carrier lifetimes observed in hafnium nitride'' submitted to Solar energy materials and Solar cells

Hongze Xia, Xiaoming, Wen, Yu Feng, Robert Patterson, Simon Chung, **Neeti Gupta ,** Santosh Shrestha, Gavin Conibeer, (2016),"Hot carrier dynamics in HfN and ZrN measured by transient absorption spectroscopy." Solar Energy Materials and Solar Cells **150**: 51-56.

G. Conibeer, S. Shrestha, S. Huang, R. Patterson, H. Xia, Y. Feng, P. Zhang, **N. Gupta**, M. Tayebjee, S. Smyth, Y. Liao, S. Lin, P. Wang, X. Dai, S. Chung, Hot carrier solar cell absorber prerequisites and candidate material systems, Solar Energy Materials and Solar Cells, 135 (2015) 124-129.

Gavin Conibeer, Santosh Shrestha, Shujuan Huang, Robert Patterson, Hongze Xia, Yu Feng, Pengfei Zhang, **Neeti Gupta**, Murad Tayebjee, Suntrana Smyth, Yuanxun Liao,

Shu Lin, Pei Wang, Xi Dai, Simon Chung" Hot Carrier solar cell absorbers: materials, mechanisms and nanostructures",

S. Chung, S. Shrestha, X. Wen, Y. Feng, **N. Gupta**, H. Xia, P. Yu, J. Tang, G. Conibeer, Hafnium nitride for hot carrier solar cells, Solar Energy Materials and Solar Cells,

Conference papers

Neeti Gupta, Santosh Shrestha; Hongze Xia, Simon Chung and Gavin Conibeer."Prospective of Zirconium Nitride as an absorber for the Hot Carrier Solar Cell", Proceedings of the 52nd Annual Conference, Australian Solar Energy Society (Australian Solar Council) Melbourne May 2014 ISBN: 948-0-646-92219-5

N. Gupta, S. Shrestha, G.J. Conibeer, H. Xia, B. Puthen-Veetil "Crystallographic analysis Of GexC1-x film deposited by RF magnetron sputtering for the hot carrier solar cells", Proceeding of the 28th Annual conference EUPVSEC 2013, Paris, France, 2013

Xiaoming, Wen, S. Chung, **N. Gupta**, Hongze, Xia, Y.Feng, S. Shrestha, Shujuan, Huang, T. W. Kee, T. Harad, G. Conibeer. Ultrafast transient absorption study of hot carrier dynamics in hafnium nitride and zirconium nitride. Photovoltaic Specialist Conference (PVSC), 2015 IEEE 42nd.

S. Shrestha, **N. Gupta**, P. Aliberti, G. Conibeer, Growth and characterization of germanium carbide films for hot carrier solar cell absorber, Photovoltaic Specialists Conference (PVSC), 2012 38th IEEE, 2012, pp. 002601-002604.

G. Conibeer, S. Shrestha, S. Huang, R. Patterson, H. Xia, Y. Feng, P. Zhang, **N. Gupta**, M. Tayebjee, S. Smyth, Y. Liao, Z. Zhang, S. Chung, S. Lin, P. Wang, X. Dai, Hot carrier solar cell absorbers: materials, mechanisms and nanostructures, 2014, pp. 917802-917802-917811.

S. Chung, X. Wen, Y. Feng, **N. Gupta**, H. Xia , S. Shrestha and G. Conibeer ," Hafnium Nitride for Hot Carrier Solar Cells" Photovolataic Technical Conference - Thin Film & Advanced Silicon Solutions 2014,

S. Shrestha, S. Chung, **N. Gupta**, F. Yu, W. Xiaoming, X. Hongze, G. Conibeer, Evaluation of hafnium nitride and zirconium nitride as Hot Carrier absorber, Photovoltaic Specialist Conference (PVSC), 2014 IEEE 40th, 2014, pp. 3428-3431.

S. Chung, S. Shrestha, X. Wen, Y. Feng, **N. Gupta**, H. Xia, P. Yu, J. Tang, G. Conibeer, Evidence for a large phononic band gap leading to slow hot carrier thermalisation, IOP Conference Series: Materials Science and Engineering, 68 (2014) 012002.

H. Xia, R. Patterson, Y. Feng, T. Smyth, Y. Liao, P. Zhang, X. Dai, **N. Gupta**, X. Wen, S. Chung, X. Jia, L. Wu, Z. Lin, B. Puthen-Veettil, S. Huang, S. Shrestha, G. Conibeer,

Numerical calculation of optical phonon decay rate in InN/GaN MQW, IOP Conference Series: Materials Science and Engineering, 68 (2014) 012009.

Simon Chung, Santosh Shrestha, Hongze Xia, **Neeti Gupta** and Gavin Conibeer."Potential of Hafnium Nitride for the Hot Carrier Solar Cell",SPIE 8923, Micro/Nano Materials, Devices, and Systems, 89232I (7 December 2013)

G.J.conibeer, S.Shrestha, S.Huang, R.Patterson, P.Aliberti, H.Xia, Y.Feng, P.Zhang ,**N.Gupta**, S.Smyth, Y. Liao, S. Lin, P. Wang, X. Dai, S. Chung, M.A. Green ," Hot carrier solar cells: Materials with modulated phonon energy for slowed carrier cooling", Proceeding of the 28th Annual conference EUPVSEC 2013, Paris, France, 2013

T. Smyth, H. Xia, Y. Feng, M.J.Y. Tayebjee, M. Dvorak, B. Puthen-Veetil, C. Johnson, R. Patterson, **N. Gupta**, Y. Liao, S. Shrestha, S. Huang, T.W. Schmidt, G.J. Conibeer," Group III-V Bulk and Quantum Well Hot Carrier Cell Absorbers", Proceeding of the 28th Annual conference EUPVSEC 2013, Paris, France, 2013

T. Smyth, P. Wadekar, C. Ching-Wen, T. Li Wei, F. Yu, X. Hongze, B. Puthen-Veetil, C. Johnson, S. Limpert, **N. Gupta**, L. Yuanxun, H. Shujuan, S. Shrestha, G. Conibeer, Hot carrier solar cells from group III-V quantum well structures, Photovoltaic Specialists Conference (PVSC), 2013 IEEE 39th, 2013, pp. 0840-0845.

G. Conibeer, S. Shrestha, H. Shujuan, R. Patterson, P. Aliberti, X. Hongze, F. Yu, **N. Gupta**, S. Smyth, L. Yuanxun, M.A. Green, Hot Carrier solar cell absorbers: Superstructures, materials and mechanisms for slowed carrier cooling, Photovoltaic Specialists Conference (PVSC), 2012 38th IEEE, 2012, pp. 000032-000035.

Yuanxun Liao, Santosh Shrestha, Shujuan Huang, Xi Dai, **Neeti Gupta**, Suntrana Smyth, and Gavin Conibeer, Fabrication of γ-Al_2O_3/Si/γ-Al_2O_3 quantum well structures for energy selective contact of hot carrier solar cell, Proceedings of the 50th Annual Conference, Australian Solar Energy Society (Australian Solar Council) Melbourne Dec 2012 ISBN: 978-0-646-90071-1

Appendix-E List of symbols and acronyms

FWHM	full width at half maximum
GIXRD	glancing incident x-ray diffraction
NC	nanocrystal
NIR	near-infrared
PV	photovoltaic
QD	quantum dot
QW	quantum well
SE	spectroscopic ellipsometry
SR	spectral response
TEM	transmission electron microscopy
UV	ultra-violet
XPS	X-ray photoelectron spectroscopy
PL	Photoluminescence
TRPL	Time resolved photoluminescence
UTA	Ultrafast transient absorption
T_s	Substrate temperature
RF	Radio frequency
DC	Direct current
t	Thickness
d_R	Deposition rate
α	Absorption coefficient of film as a function of wavelength
ρ	Resistivity
λ	Wavelength of light

μ	Mobility
θ	Angle
E_o	Energy of the localized states in the band gap